Order Number 8918595

On the dynamics of the Alaska coastal current

Luick, John Leonard, Ph.D.

University of Alaska Fairbanks, 1988

U·M·I

300 N. Zeeb Rd.
Ann Arbor, MI 48106

ON THE DYNAMICS OF THE ALASKA COASTAL CURRENT

A

THESIS

Presented to the Faculty of the University of Alaska

in Partial Fulfillment of the Requirements

for the Degree of

DOCTOR OF PHILOSOPHY

By

John Leonard Luick, B.S.

Fairbanks, Alaska

September, 1988

ON THE DYNAMICS OF THE ALASKA COASTAL CURRENT

by

John Leonard Luick

RECOMMENDED:

E. Kovalik

Walter R Johnson

Jean P. Gosink

George W Tripphut

Thomas C. Royer
Advisory Committee Chair

Henry Joseph Niebauer
Department Head

APPROVED:

Dean, School of Fisheries and Ocean Sciences

Dean of the Graduate School

7/19/88
Date

ABSTRACT

The Alaska Coastal Current (ACC) in the northern Gulf of Alaska is a wind- and buoyancy-driven near-surface jet primarily maintained by the horizontal salinity gradient due to fresh water entering at the coast. It serves as the major source of fresh water to the North Pacific Ocean.

The buoyancy driving force is the major focus of this investigation. The study area is situated just "downstream" of Prince William Sound (PWS), a large estuary whose surface outflow is seen to occupy a narrow inshore band after joining the ACC. The effect of this band appears to be the formation of an occasional double maximum in the ACC. The period focused on in this study was selected on the basis of weak windstress but large fresh water input in order to emphasize the buoyancy forcing.

The TS characteristics and a water mass tracing technique are used to separate the thermal and haline signals in the buoyancy forcing and to track the origin and fate of the source waters of the study area. The buoyancy driving force is shown to be primarily haline, with temperature playing a secondary, moderating role.

Because of the large topographic variablity and sloping density interfaces, and in order to exploit the available data, a diagnostic model retaining the baroclinicity and bottom topography terms was chosen to study the dynamics. Model premises are verified by results from hydrographic surveys, moored current meters, and a profiling current meter.

The model predicts a midshelf region of negligible sealevel gradient, with a nearshore (≈ 70 km wide) band over which the sealevel changes by about 25 cm. The sloping surface drives a strong (≈ 100 cm/s) surface flow, which decreases to zero and reverses below about 100 m

due to the opposing baroclinic pressure gradient. The flow splits around a shoal region. The onshore portion joins the outflow from PWS and accelerates downstream forming a double maximum. The offshore segment forms a large meander before rejoining the rest of the ACC, advecting midshelf water shoreward. The momentum balance is dominated by the JEBAT terms, which primarily determine the flow along and across contours of f/H.

TABLE OF CONTENTS

LIST OF FIGURES

LIST OF TABLES

ACKNOWLEDGEMENTS

It was my good fortune to find myself considering graduate study at the same time Tom Royer was looking for a graduate student to work on the COJET project. His continued support and reliable guidance are gratefully acknowledged. I especially appreciate the autonomy I was granted to pursue my own interests and the rare opportunities which are available to students at the Institute of Marine Science.

This thesis benefitted from the assistance of a number of individuals. In particular, Dave Nebert, whom I thank for data quality and assistance with personal computers; John Smithhisler, for help with the weather station and for his excellent coffee; Chirk Chu, for programming assistance; Gil Mimken, for perspective; Walter R. Johnson, for help with data analysis and interpretation; Zygmunt Kowalik, to whom I owe the success of the model; and Joan Gosink, for timely suggestions.

It is friends and family that make it all worthwhile. I would like to thank all my friends, the closest of whom is my wife, Eve.

I dedicate this thesis to my antecedents and descendants.

This work was supported by the National Science Foundation.

Chapter 1. INTRODUCTION

The Alaska Coastal Current is a near-surface alongshore jet found between three and twenty kilometers from shore, flowing westward along the northern Gulf of Alaska (Fig. 1.1). It forms part of a system of coastal currents extending from British Columbia counterclockwise around the gulf to the Aleutian Islands. The primary driving force and most distinguishing characteristic is the pressure gradient maintained by a large freshwater inflow at the coast (Schumacher and Reed, 1980, Royer, 1981). The intensity and structure are further modified by wind stress at the upper surface and by bottom frictional torques due to flow over variable shelf topography. The flow is further complicated by disturbances due to nonlocal sources such as tides.

Until the early 1970's, the inner shelf circulation, in general, was considered too chaotic or of too little significance to be the subject of extensive research, in comparison to larger scale motions. The growing awareness in the 1960's of the economic importance of the inner shelf, along with the development of improved instrumentation, resulted in a dramatic increase in the number of coastal studies. There has been a wide recognition of the inner shelf regime as a distinct zone possessing a set of unique characteristics which distinguish it from both the deep ocean and estuarine environments: the so-called "coastal boundary layer" (Csanady, 1977).

The study of coastal circulation has historically been associated with that of purely estuarine systems (Officer, 1976). In terms of cross isobath exchange, the inner shelf regime resembles an estuary with widely separated side walls (inner shelf being defined to include the region beyond the surf zone which is significantly affected by riverine input). The primary resemblance is in the classic salt-wedge pattern of underlying oceanic water, or conversely, the wedge-shaped layer of overlying fresh water resulting from riverine influx. Examples of this approach are Fischer (1980), who discusses horizontal mixing and dispersion along the east coast of the United States, and Atkinson *et al.* (1978), who compute shelf flushing rates in the

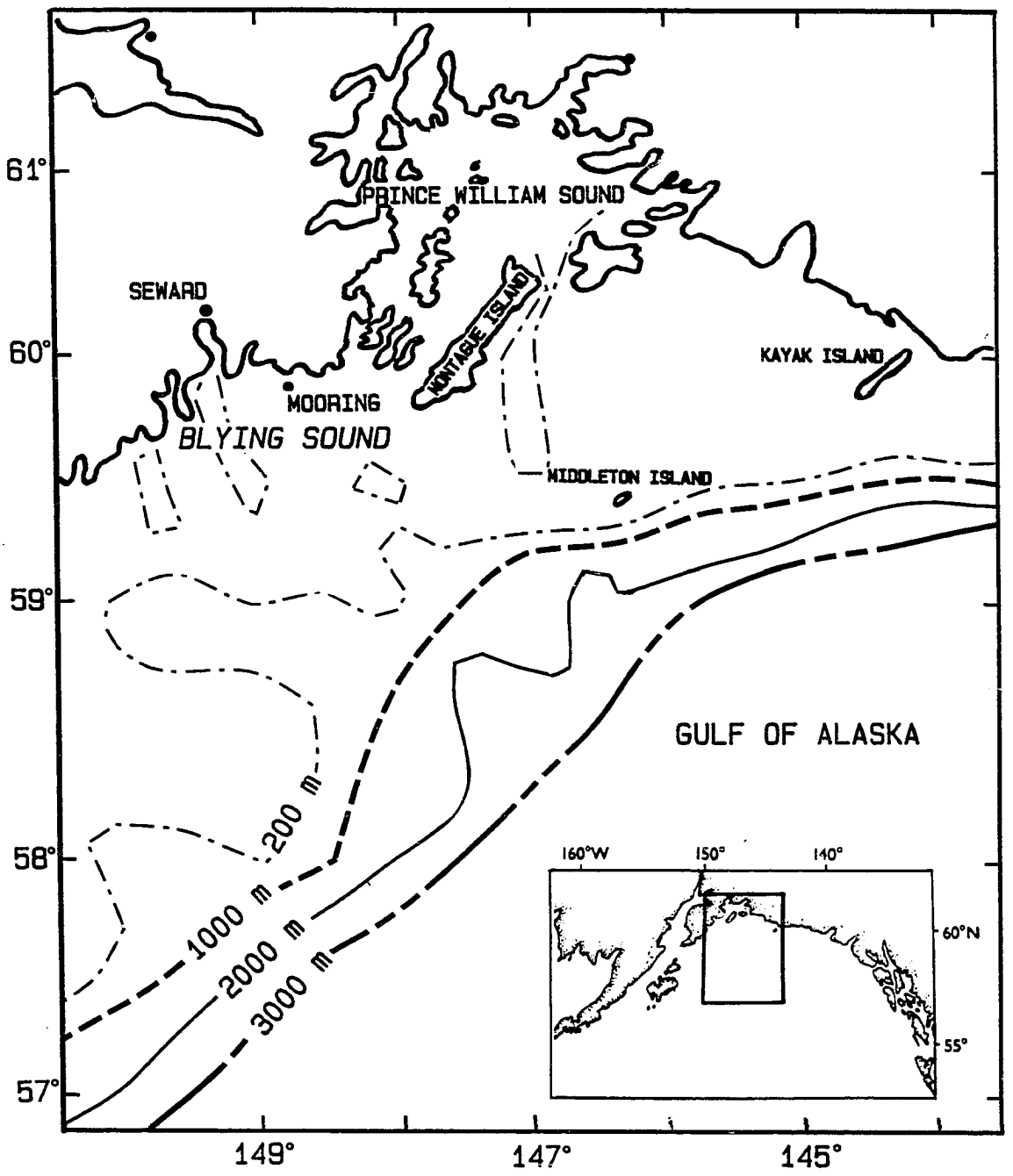

Fig. 1.1. Northwest Gulf of Alaska with mooring location. Inset map shows location of Fig. 1.1.

Georgia Bight and relate them to Gulf Stream meanders.

Stommel and Leetma (1972) presented an analytical model which applied to the winter circulation on a highly idealized version of the northeast coast of North America. Treating the entrance of freshwater at the coast as a line source, and assuming a steady wind stress and linearized equations of motion, while including the equation of advection for salt, they categorized the possible dynamic regimes based on Ekman number (a nondimensional ratio of internal frictional dissipation of momentum to the coriolis acceleration of the flow). Csanady (1976) discussed the shortcomings of this type of approach, in particular the assumption that the wind forcing, which is event-like, is constant in time. The influence of wind stress continues to be a problematical element in coastal models, partly due to questions such as how momentum is transferred across the air-sea interface, and partly due to the difficulty in achieving accurate wind measurements. An important result of Stommel and Leetma (1972), however, was the recognition of the importance of the fresh water driving mechanism.

The influence of a source of fresh water on coastal water properties and their density distributions has been observed in many parts of the world (Pettigrew and Murray, 1986). In some areas, such as those studied by Stommel and Leetma (1972), the water enters through a series of rivers distributed more or less regularly along the coast, and the driving force can be thought of as a line input. This is also the case along the east coast of Nicaragua (Murray *et al.* 1982), the coasts of Norway (Mork, 1980) and British Columbia (LeBlond *et al.*, 1986a), and along the northern Gulf of Alaska (Royer, 1981). A related circulation pattern occurs at the midwinter ice-edge front in the Bering Sea, where a baroclinic current flows along the ice edge as a result of density gradients maintained by sea ice melting at the edge (Muench and Schumacher, 1985). Csanady (1982) describes another line source of buoyancy which is observed over the shallow nearshore parts of the Great Lakes during the spring transition from winter mixed to summer stratified conditions. A baroclinic current develops parallel to the coast at the thermal front separating the warm inshore

water from the cold offshore water. In other areas, buoyancy is derived from a point source: a river such as the Amazon, Columbia, or Nile. A number of other larger scale currents are also properly categorized as buoyancy driven coastal currents, for example, the East Greenland current, which carries Arctic Ocean water southward along the east coast of Greenland (Griffiths and Linden, 1981).

Where certain simplifying assumptions can be made, successful analytic models incorporating wind and buoyancy forcing have been constructed. LeBlond *et al.* (1986b) were able to reproduce the seasonal behavior in a two layer model with entrainment, but wind and alongshore bathymetric changes were ignored. Murray and Young (1985) solved the momentum equations for a situation in which the isopycnal surfaces are evenly spaced vertically, the wind is steady, and the depths are not too great. (An underlying problem with this approach, also used by Heaps (1980), is that the solutions involve sums and differences of hyperbolic functions with depth in the argument. Even when a non-dimensionalized depth is used, these functions grow to very large values, and errors increase rapidly.) These models are successful in predicting certain aspects of the velocity distribution, in that the momentum balances are at least adequate. The primary driving force is the sloping density surfaces, and the steady state is maintained either by a loss of buoyancy at the interface (LeBlond *et al.* 1986b) or by friction (Murray and Young, 1985). A variety of three-dimensional coastal ocean models are described in Heaps (1987).

In the past decade, high latitude oceans have received increased attention as a result of both environmental considerations and the recognition of their scientific importance. A five year oceanographic study in the northern Gulf of Alaska was undertaken in 1974 as part of OCSEAP (Outer Continental Shelf Environmental Assessment Program). The sampling grid was chosen with shelf-width scale processes in mind. Station separations were 10 nautical miles. Despite the spacing width, an alongshore coastal current was suggested by the density profiles of the innermost stations. This current was shown to be statistically independent of the large scale (shelf break) sea level slope (Hayes

and Schumacher, 1976). Further details of the baroclinic structure were revealed by later hydrographic surveys in the Northwest Gulf of Alaska (Schumacher and Reed, 1980). The coastal fresh water input was correlated with alongshore transport by Royer (1981). However, these studies were limited by the lack of a comprehensive data set, so in 1983 the coastal jet (COJET) field study was initiated.

The emphasis of the COJET study was the response of the flow to variations in buoyancy forcing, particularly as compared to the wind stress. These act through fundamentally different mechanisms (body force versus surface stress), and their seasonal variations are out of phase. However, they are not unrelated. Wind stress acts both directly in driving surface motions, and indirectly through the redistribution of mass. For example, a conclusion of the COJET study (Johnson *et al.*, 1988), is that, at the monthly-averaged time scale, variations in transport are more closely correlated with variations in alongshore wind speed than freshwater discharge. Statistical results such as this, while valuable in identifying correlated processes, do not provide a satisfactory means for predicting details such as the offshore position of the supernatant jet. On the other hand the complexity of the interrelated driving and response mechanisms makes it impossible to fully parameterize the physical system, as one might use, for example, to predict the path of a comet. The approach taken here is to identify the important features, and to reproduce those features in a numerical model which will supply additional insight into the physical basis of the processes. The intent is to establish the essential dynamics of the steady-state buoyancy-driven mean flow. Steady-state is being defined here to mean those flow patterns and property distributions which are unchanged over the diurnal tidal cycle but which are allowed to vary over the course of months. This separation is artificial in the sense that the steady-state field is the net result of a series of shorter time scale events. Treating the mean field as a steady state contains an implicit assumption that the shorter time scale processes combine linearly; here, this assumption is justified by the good coherence downstream of the property

distributions and by the success of a linearized steady-state model in reproducing the circulation.

In Chapter 2, the field study is described. Also, the considerations used in choosing the sampling scheme are discussed.

In Chapter 3, the results of the hydrographic surveys are used to describe the seasonal evolution of water properties on the shelf. The buoyancy driving force is found to be controlled by the distribution of salinity, rather than temperature, at most depths, and over most of the year. The influence of the outflow from Prince William Sound onto the shelf is shown by T-S diagrams; the outflow is traced through the study area using cross-sections of a "density flux function". The outflow volume is used to test the hydrologic model of Royer (1981). Although the result is preliminary, it appears to confirm the hydrologic model.

In Chapter 4, the temporal variability of the ACC is analyzed using the current meter data. The underlying purpose is to define time and spatial scales over which the assumptions of the steady-state diagnostic model are valid. Thus, the subinertial mean flow and tidal oscillations are considered in terms of the rate of cross-shelf exchange. The profiling current meter data, which are used to initialize the model, are compared to the moored current meter data averaged over both 3 day and 29 day intervals. Attention is focused on a particular two week interval in early September, 1983, which is used in the model study of the dynamics.

In Chapter 5, a steady-state momentum balance is proposed and a diagnostic numerical model of the type pioneered by Sarkisyan (1977) is used to predict the mean circulation. The model output includes sealevel, depth-averaged velocity, and horizontal velocity as a function of depth. The model results and their implications to the shelf circulation in the northern Gulf of Alaska and elsewhere are summarized in Chapter 6.

Chapter 2. THE COJET FIELD STUDY

The 1983-1984 COJET field study included hydrographic (salinity and temperature versus depth) surveys, moored current meters, a moored weather buoy, a coastal weather station, and a profiling current current meter. Since March, 1986, an acoustic doppler current profiler has been used for direct measurement of velocity.

Royer (1981) found that the Rossby radius of deformation in the highly stratified nearshore region could be as small as 5 km. As a result, a station separation of 2 nautical miles (3.7 km) was chosen for COJET (Fig. 2.1). A pair of north-south sections (CF and CJ) separated by 5 n.m. were established to cross the central part of the area, from the coast out to nearly 60 km (Fig. 2.1). In order to provide a measure of longshore changes, and to discriminate water discharged from Prince William Sound from that originating on the outside of Montague Island, three more sections (ML, MI, and AC) were added upstream of the CF and CJ sections. The area coverage was completed by adding two more sections to the southwest (the SR section, and a second section which is to the west of the area shown in Fig. 2.1), which roughly connect the outer end of the CF line with the bending coastline, and by decreasing the station separation in the GAK line, which has been occupied at 10 n.m. intervals since 1970. With few exceptions, all of these stations were occupied on each of the eight COJET cruises, and many, particularly the CF line, were repeated more than once on most cruises. In all cases, a Neil Brown Mark IIIB CTD system was used to measure conductivity and temperature versus depth, and the Practical Salinity (S) was determined using the Unesco (1981) formulas. (As so defined, S has no units, but it is numerically equivalent to salinity in parts per thousand or grams per kilogram.) The CTD recorded approximately 16 samples per meter, which were averaged in one meter intervals. The CTD was calibrated annually at the Northwest Regional Calibration Center of NOAA in Seattle. Field calibrations were also done on each cruise. CTD data were processed by the Institute of Marine Science Data Management Group using standard

oceanographic techniques.

A current meter array was moored on the CF line 9 km from shore in 185 m. (Fig. 2.1). This mooring was designed to provide vertical resolution of the horizontal velocity, with Aanderaa RCM4 current meters at 50, 70, 110, and 175 m from surface (the deepest meter was 10 m above bottom). An Aanderaa tide gauge (TG3) was installed on the anchor. A second mooring was placed nearby, with an EG&G Vector Measuring Current Meter (VMCM) current meter at 2 m and an Aanderaa meter below it at 4 m. The location chosen has a relatively smooth bottom topography. The choice was also based on the apparent position of the current axis determined using the geostrophic method (Fomin, 1964) and using earlier data. The current meters were also needed to provide 1) a measure of temporal variability (power spectrum), 2) the amplitude and phase of variation in the annual cycles of temperature and salinity, and 3) an independent check on other velocity estimates. The data recovery for the five current meters and the tide gauge over the nineteen month study period is shown in Fig. 2.2. Details of these moorings and the data recovery can be found in Johnson and Royer (1986).

Meteorological data were obtained from three sources. A weather station (Luick *et al.*, 1987a) was installed atop a steep bluff at the inshore end of the CJ line to provide local measurements of wind, precipitation, barometric pressure, relative humidity, and temperature. This station operated from April 8, 1983 until October 30, 1984. A weather buoy operated for 11 days in the vicinity of the current meters to give more accurate conditions at the sea surface. Finally, the six-hourly surface winds were obtained from 3° Fleet Numerical Oceanography Center (FNOC) for 60° N, 149° W. A description of these data sets and their intercomparison can be found in Luick *et al.* (1987a).

A profiling current meter (PCM) was used to measure the velocity at the inner (nearshore) 13 stations on the CF line on each of the eight cruises in 1983 and 1984 (Johnson *et al.*, 1988). This instrument consists of an Aanderaa RCM4 current meter mounted on a PVC pipe

mounted horizontally, and is lowered slowly to the bottom. Here, the data set is used to form a set of boundary conditions for the model studies in Chapter 5.

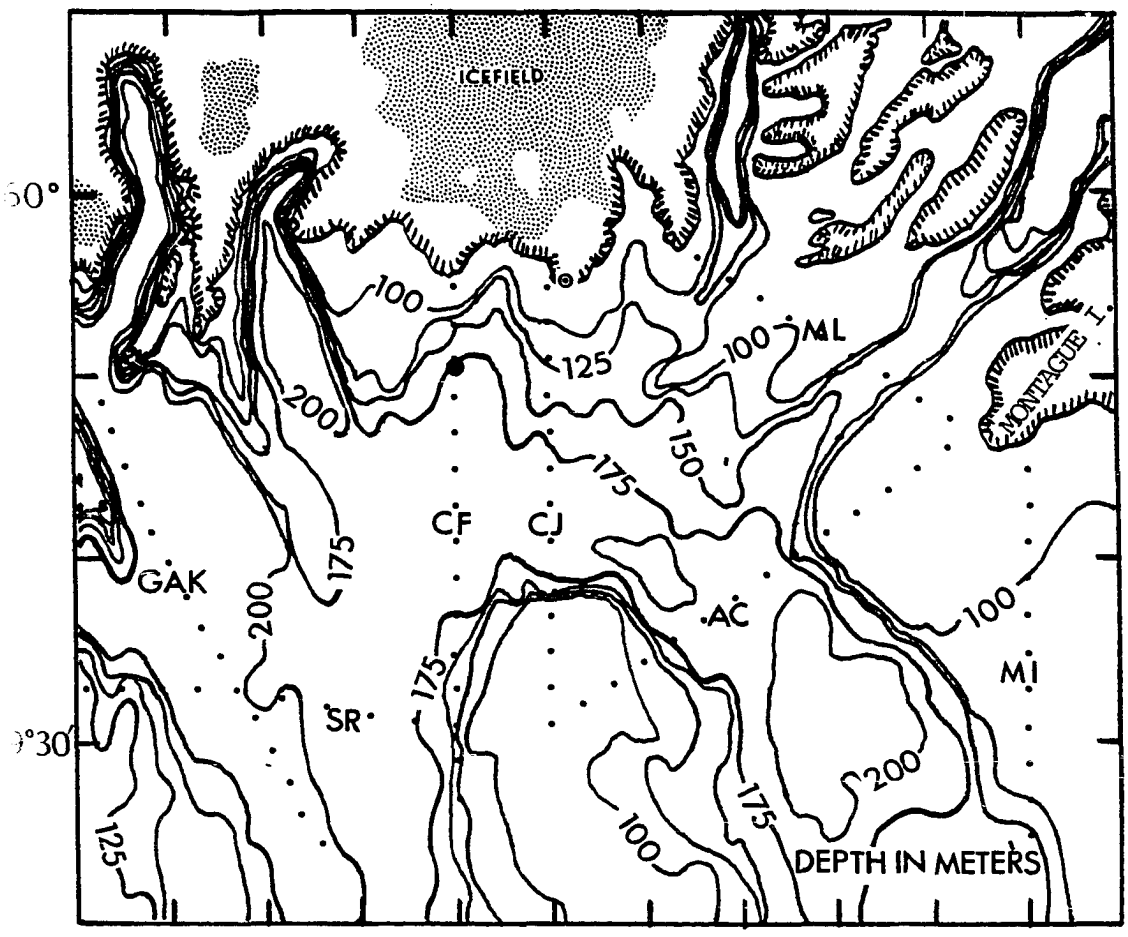

Fig. 2.1. Study region of COJET experiment. Hydrographic sections (CF, CJ, etc.) are marked by small dots; the mooring location is marked by the large dot on the CF line; the coastal weather station is marked by a bullseye. Stippled areas are icefields or glaciers. Scale 10 nautical miles per inch or 7.29 km per cm.

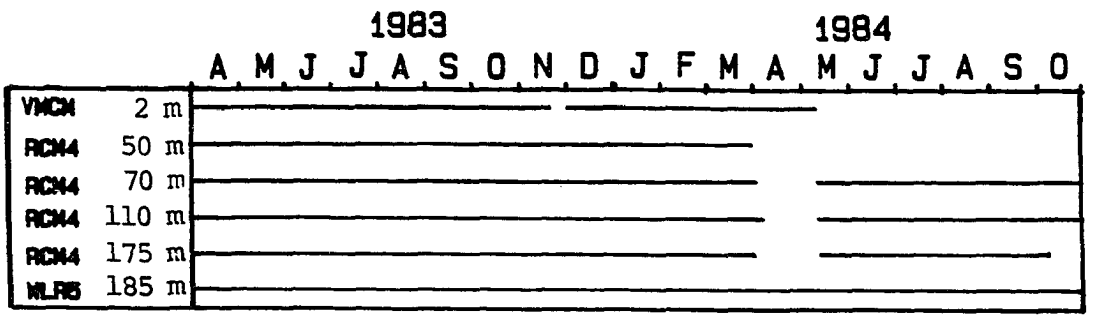

Fig. 2.2. Data recovery for the five current meters and the tide gauge over the nineteen month study period. Nominal depth of meters is in the second column.

Chapter 3. WATER PROPERTIES IN BLYING SOUND

3.1 Cross sectional distributions at Cape Fairfield

The seasonal evolution of the cross-shelf distribution of temperature, salinity, density is illustrated in Figs. 3.1, 3.2, and 3.3, respectively. The wedge shaped upper layer at the coast, typical of buoyancy driven coastal currents, is seen in all three. Otherwise, their radically altered character over the course of the year makes it impossible to speak of a typical structure without reference to season. The same can be said of the baroclinic, geostrophic velocities, which occur in response to the density gradients.

The most immediate feature observable in the temperature sections (Fig. 3.1) is the thermal stratification beginning in June and building through August of both years. This is due primarily to solar heating, which is fairly uniform over the shelf. The horizontal temperature gradients appear weak, indicative of their secondary role in the dynamics. However, the vertical gradient can become large. In September, 1983 (Fig. 3.1c), there was a 6°C range between surface and bottom, and in August 1984 (Fig. 3.1g), the range was more than 9°C. With convergences or divergences resulting from the Ekman transport associated with the winds, small vertical property gradients can become tilted to produce a horizontal property gradient. A possible example of this is the October section (Fig. 3.1h), which followed a period of vigorous winds (Luick *et al.*, 1987a).

Winter cooling in the upper layers can sometimes lead to a small increase in temperature with depth. This was observed in the first cruises of both years (Fig. 3.1a,e). This cooling is not sufficient to create vertical instability, since it is prevented by the increase in salinity with depth (Johnson *et al.*, 1988). Although the shelf is too deep to allow surface wind mixing to reach the bottom, winter cooling eradicates the temperature gradients. In the final cruise of 1983 (Fig. 3.1d) the temperature over most of the shelf was greater

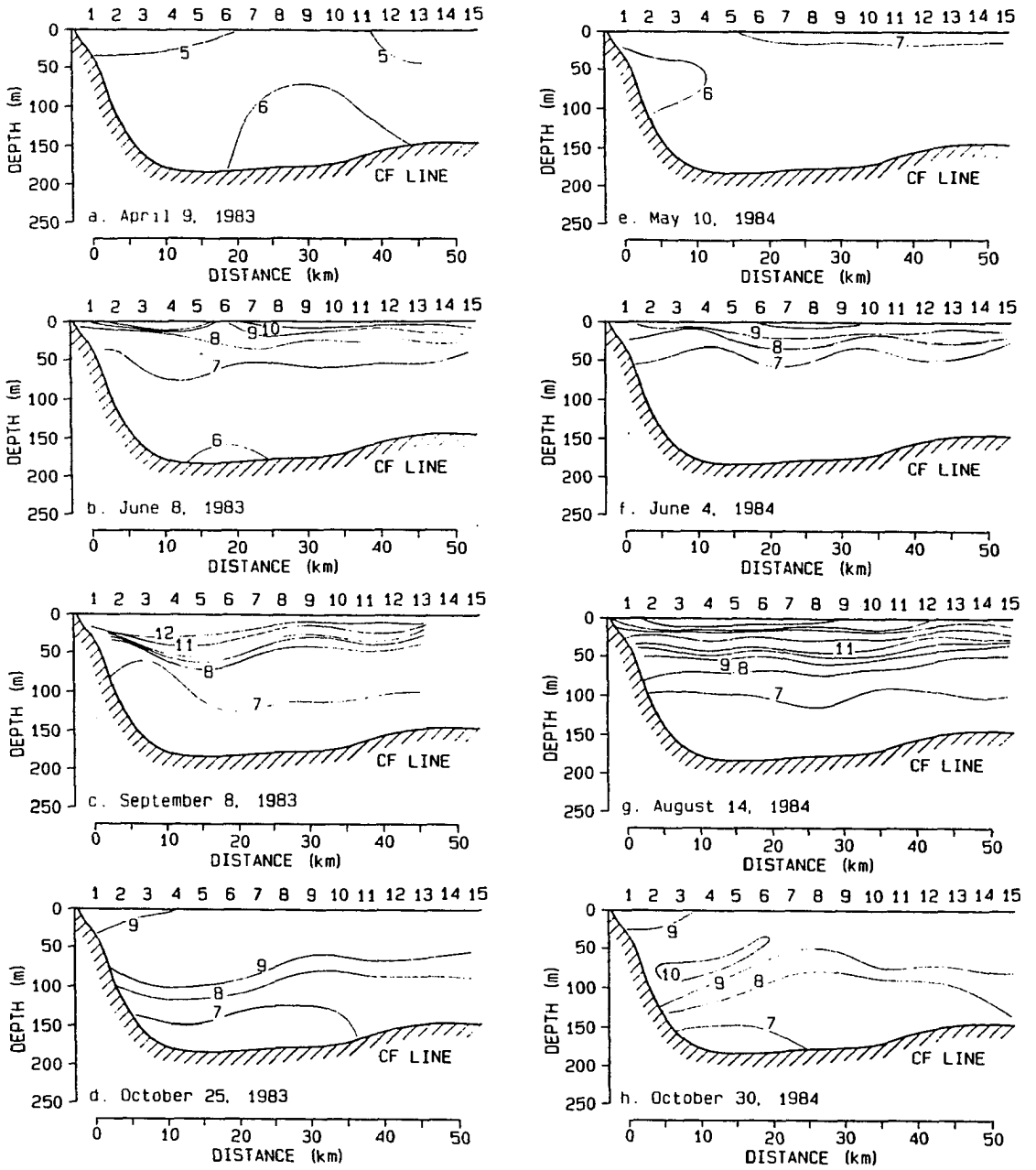

Fig. 3.1. Cross-section of temperature (°C) at the CF section.

than 7°C. By May, 1984 (Fig. 3.1e) no trace remained of the 7° water.

Compared to the thermal signal, the salinity changes are highly nonuniform across the shelf, reflecting the coastal origin of the salinity change (Royer, 1981). A wedge-shaped layer of low salinity water over the inner half of the CF section was observed on all eight cruises, but in August 1984 (Fig. 3.2g) the layer was nearly horizontal, with water of salinity less than 30 over more than half of the section, and the deepest isohalines (S>32) sloped upward toward shore. Two possible explanations for the August 1984 situation are a relaxation or reversal of the downwelling-favorable winds, and a reduction of freshwater input. For the entire eighteen month study period, the monthly mean wind computed from the FNOC pressures was at its minimum in July 1984 (Luick *et al.*, 1987a). On the other hand, using the hydrology model of Royer (1982), the freshwater discharge was anomalously low in Southeast Alaska in May and June 1984 (allowing 2-3 months for the signal to reach Blying Sound) and anomalously low along the south coast of Alaska (the Blying Sound region itself) in May through August 1984. These two factors, reduced wind and reduced discharge, probably combined to produce the August 1984 situation.

The first salinity cross-section is from April, 1983 (Fig. 3.2a), which can be taken to be typical of late winter conditions. Following April, the bottom salinities gradually increase (Fig. 3.2 b,c,d), due to the advection into the region from offshore of a deep saline layer. The shoreward motion has been hypothesized to be in response to summer relaxation of the downwelling-favorable winds of winter (Livingstone and Royer, 1980, and Luick *et al.*, 1987a).

Using only the cruise data, extremes in the salinity occurred in 1983. Salinity was lowest (S<27) in September 1983, at the surface and near shore (Fig. 3.2c). The highest salinity (S>33) occurred shortly thereafter, in October, at the bottom between 10 and 30 km offshore (Fig. 3.2d). At the same time the highest transport observed during study period was seen in October 1983 (to be discussed in Chapter 4). However, from the continuous time series of salinity data from the

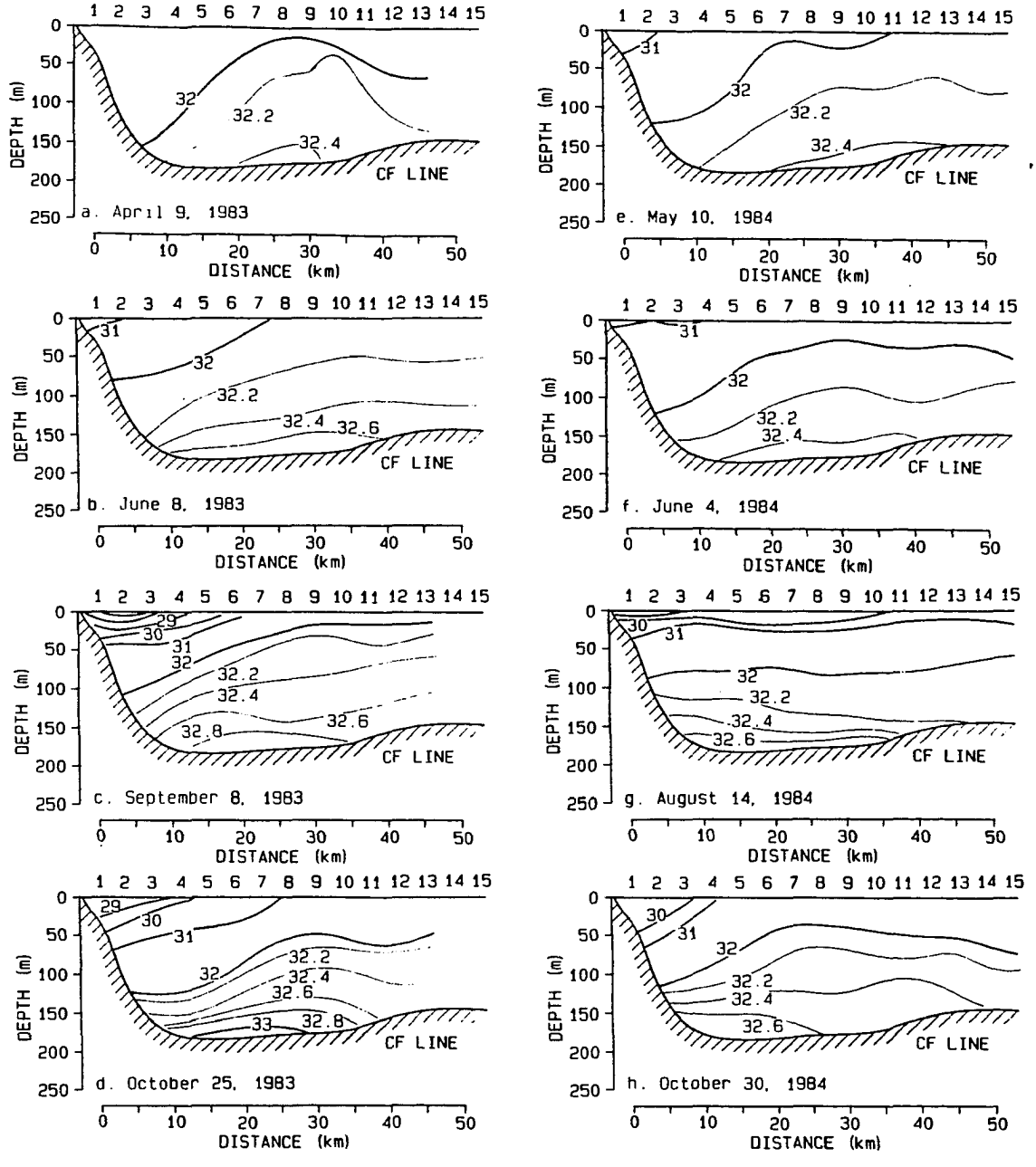

Fig. 3.2. Cross-section of salinity at the CF section.

deepest current meter near CF3, Johnson *et al.* (1988) found that the bottom salinity reached its minimum for the nineteen month study period in January, 1984. This minimum comes only two months after the maximum; it is a result of the coastal downwelling of fresh surface water rather than direct vertical mixing.

The seasonal cycle in density closely parallels that of salinity. Again, the density (σ_t) surfaces take on an opposite slope in the lower half of the water column in August 1984 (Fig. 3.3g). Also, the maximum and minimum densities occur simultaneously with their counterparts in salinity. In late winter (Fig. 3.3a), at the surface, σ_t changes by only a few tenths between shoreline and 50 km offshore. The vertical gradients are even smaller. By September 1984 (Fig. 3.3d) the horizontal gradient is 5 σ_t units and the vertical gradient has increased to 6 σ_t units. The April two-layer model internal Rossby radius of deformation ranges from 2 km within the first few kilometers of shore, to 5 km in the offshore portion (Johnson *et al.*, 1988). In September the increased density gradients result in Rossby radii of 15 km inshore and 30 km in the offshore portion. Strictly speaking, however, a two layer model does not fit the September data, because the vertical density gradient is too large in the upper layer.

The slopes of isopycnals in coastal regions are often nearly independent of depth within the upper and lower layers (Mork, 1980). This fact was exploited in the models of Heaps (1980) and Murray and Young (1985). This behavior is observed in the Blying Sound region (Fig. 3.3). Although the density gradients undergo large changes in amplitude, the slopes within the upper and lower layers remain fairly constant with depth.

3.2 Thermal *vs* haline effect on density: graphical approach

The equation of state of seawater (Unesco, 1981) defines density as a function of temperature, salinity, and pressure. For the pressure ranges involved in this study, the pressure effects on density can be ignored. On the whole, for the conditions present in Blying Sound,

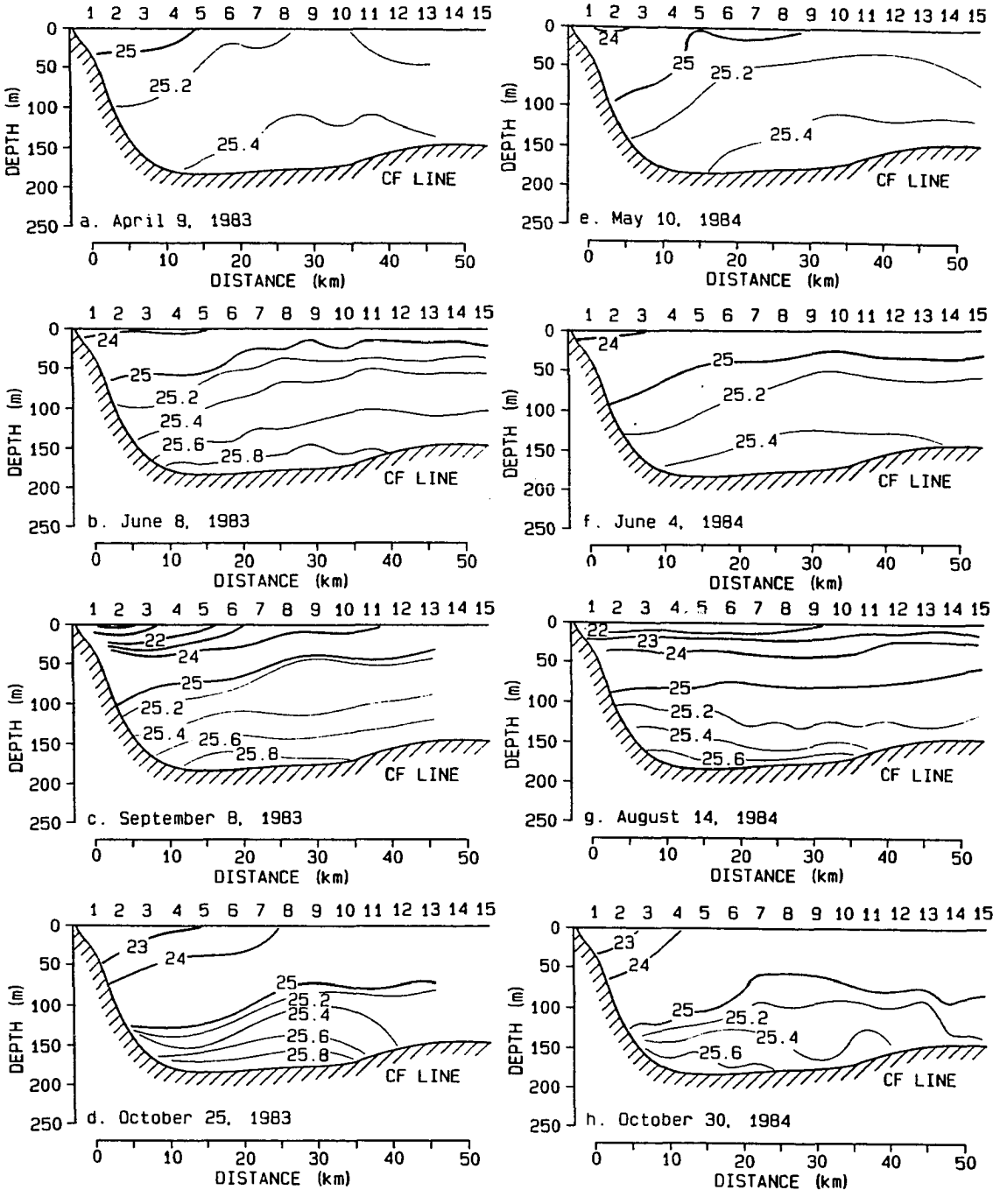

Fig. 3.3. Cross-section of σ_t at the CF section.

variations in salinity have been thought to dominate the perturbation mass (ρ') distribution which drives the ACC (Royer, 1979, 1981) and determines the vertical stability. (ρ' refers to an *in situ* density minus an areal average). This conclusion is supported using a simple graphical technique, although there are certain instances where the horizontal temperature structure does prevail.

The Cape Fairfield section is chosen to represent the entire Blying Sound and northern Gulf of Alaska. This choice includes both the outflow from Prince William Sound and the coastal water which enters from outside Montague Island. Representative TS plots from a point just offshore of the mooring are presented chronologically in Fig. 3.4. If the points on the TS curve lie on a straight line, the relative influences of temperature and salinity on density are approximately constant with depth. The TS curves reveal that for much of the year, the relative influences are a function of depth. For example, in Fig. 3.4e, the slope of the TS curve changes abruptly at several depths. In the upper 25 m the curve is nearly vertical, so the density change is associated with the change in temperature. Beneath 25 m, the curve is nearly horizontal, and the density change can be attributed to salinity.

This can be made more explicit by using a graphic technique. The region below 55 m in Fig. 3.4e is chosen to illustrate the method. To determine the temperature effect, a vertical (S=constant) line is followed from the 55 m value to the temperature of the bottom water (6.3°C). The isopycnal crossing this point has the density the bottom water would have had, if the salinity had remained constant. A line drawn from the 55 m point on the TS curve to that isopycnal is therefore the temperature effect on σ_t below 55 m. Similarly, the line drawn from the 55 m point to the isopycnal passing through the point whose temperature is the same as that at 55 m and whose salinity is that of the bottom water, represents the salinity effect on σ_t below 55 m. In Fig. 3.4e, these effects are shown by arrows. The temperature contribution (the short arrow) is actually in the direction of decreasing density with depth, but the salinity contribution (long

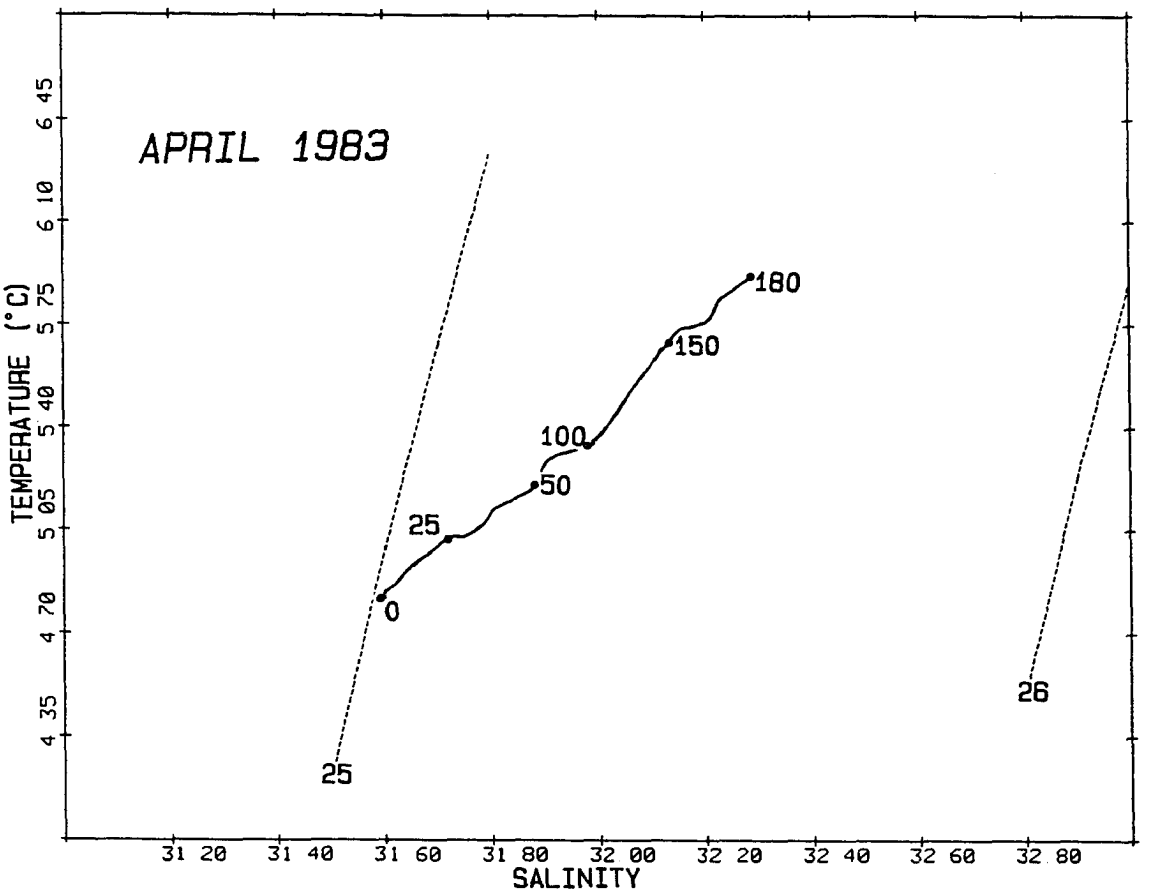

Fig. 3.4a. April, 1983

Fig. 3.4. TS diagrams at CF 4 (59° 49'N, 148° 50'W). a) April, 1983; b) June, 1983; c) September, 1983; d) October, 1983; e) May, 1984; f) June, 1984; g) August, 1984; h) October, 1984.

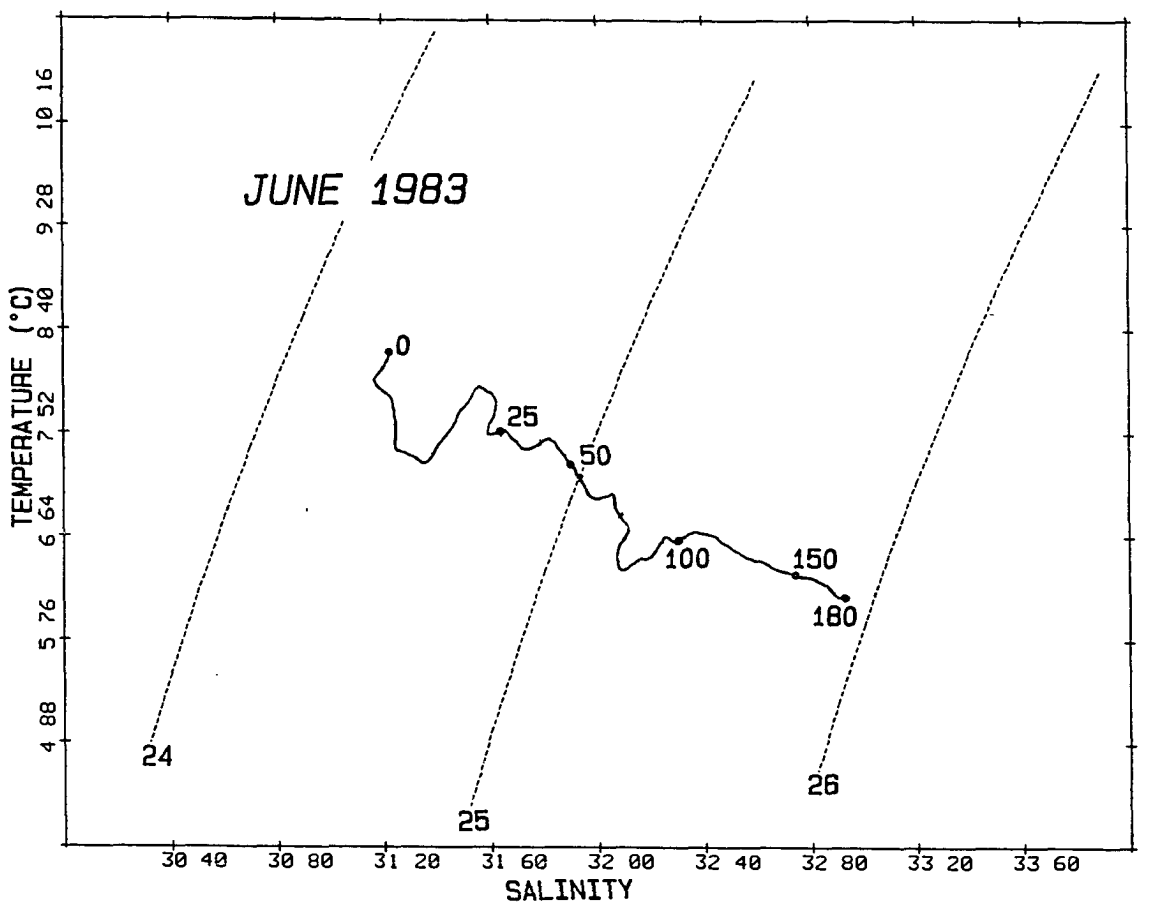

Fig. 3.4b. June, 1983

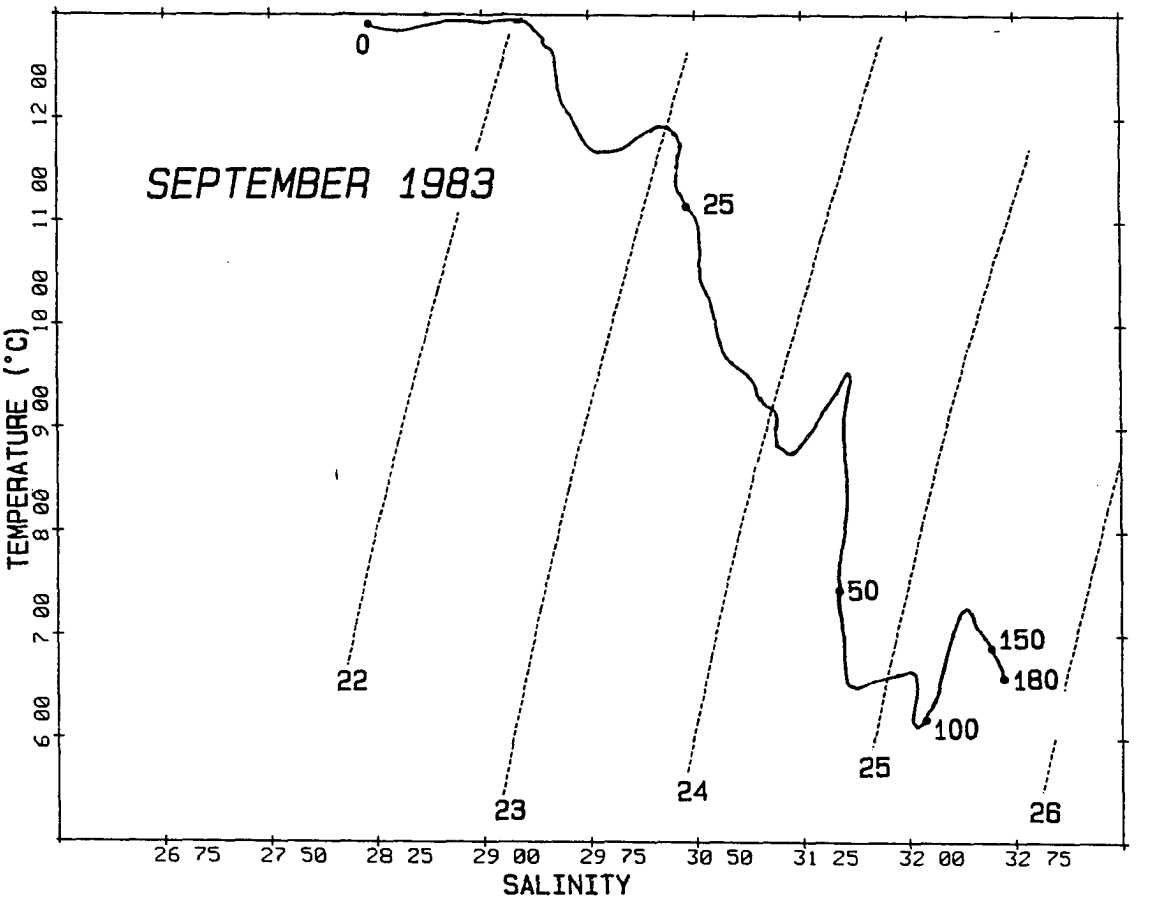

Fig. 3.4c. September, 1983

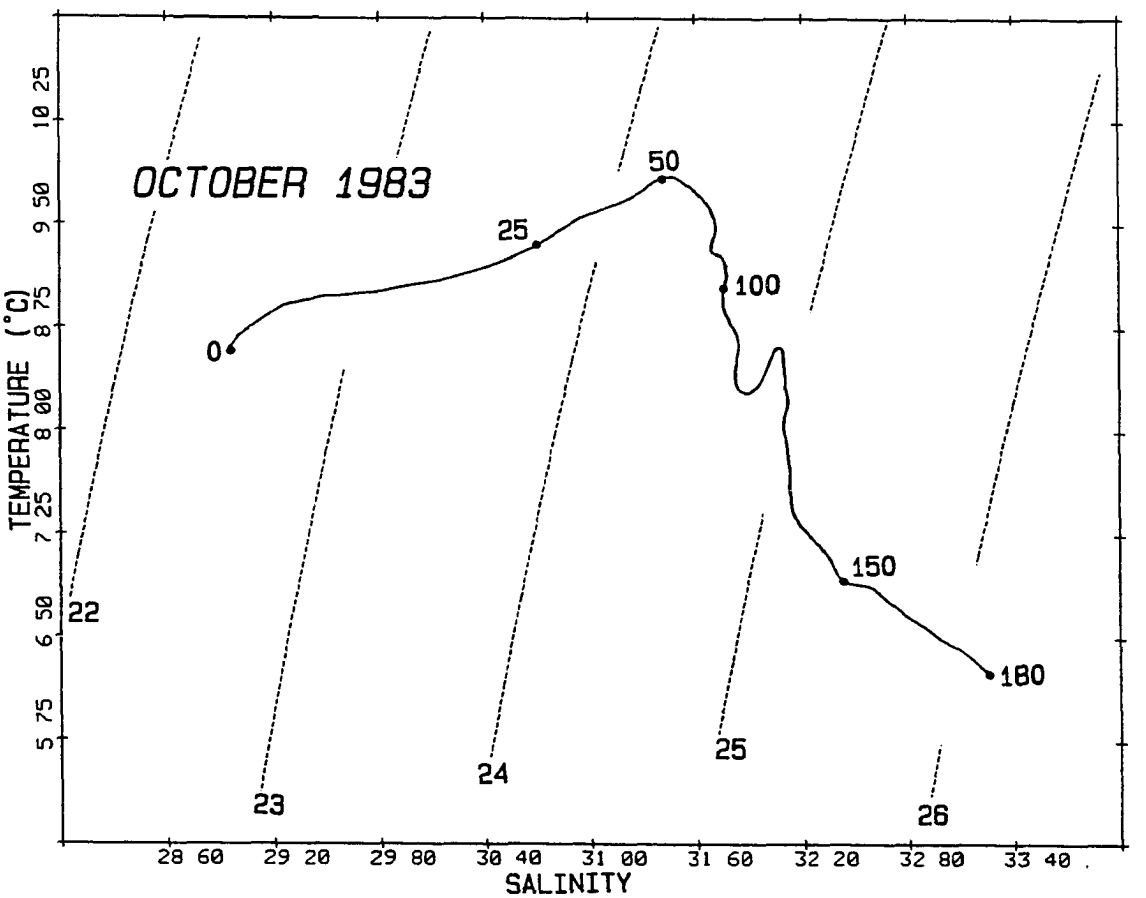

Fig. 3.4d. October, 1983

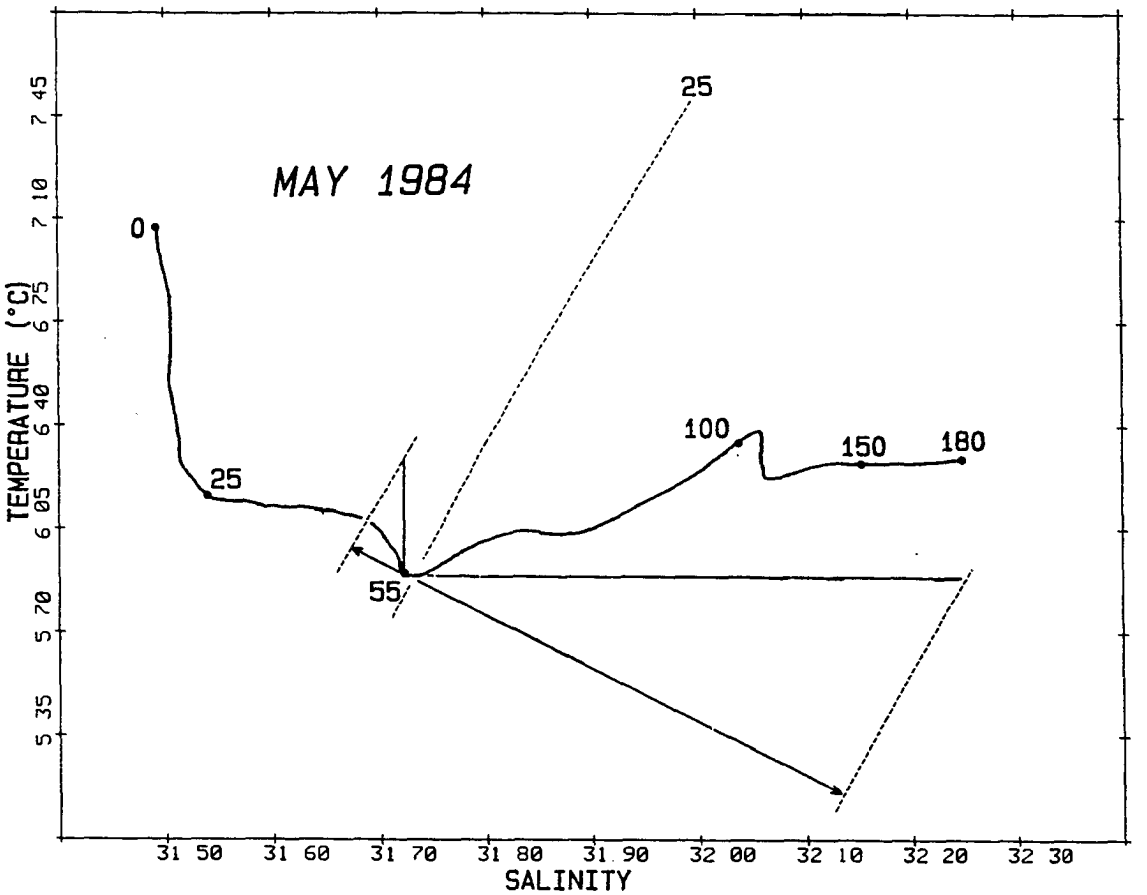

Fig. 3.4e. May, 1984

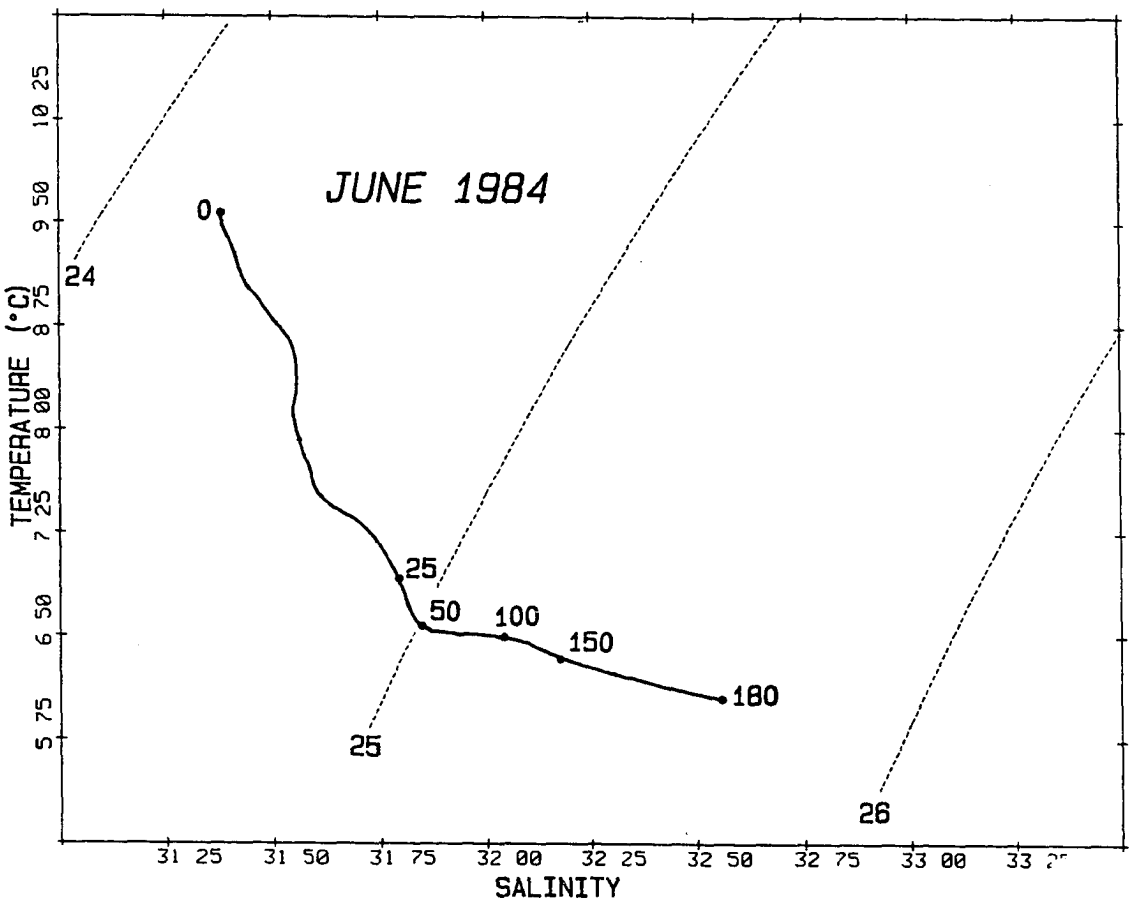

Fig. 3.4f. June, 1984

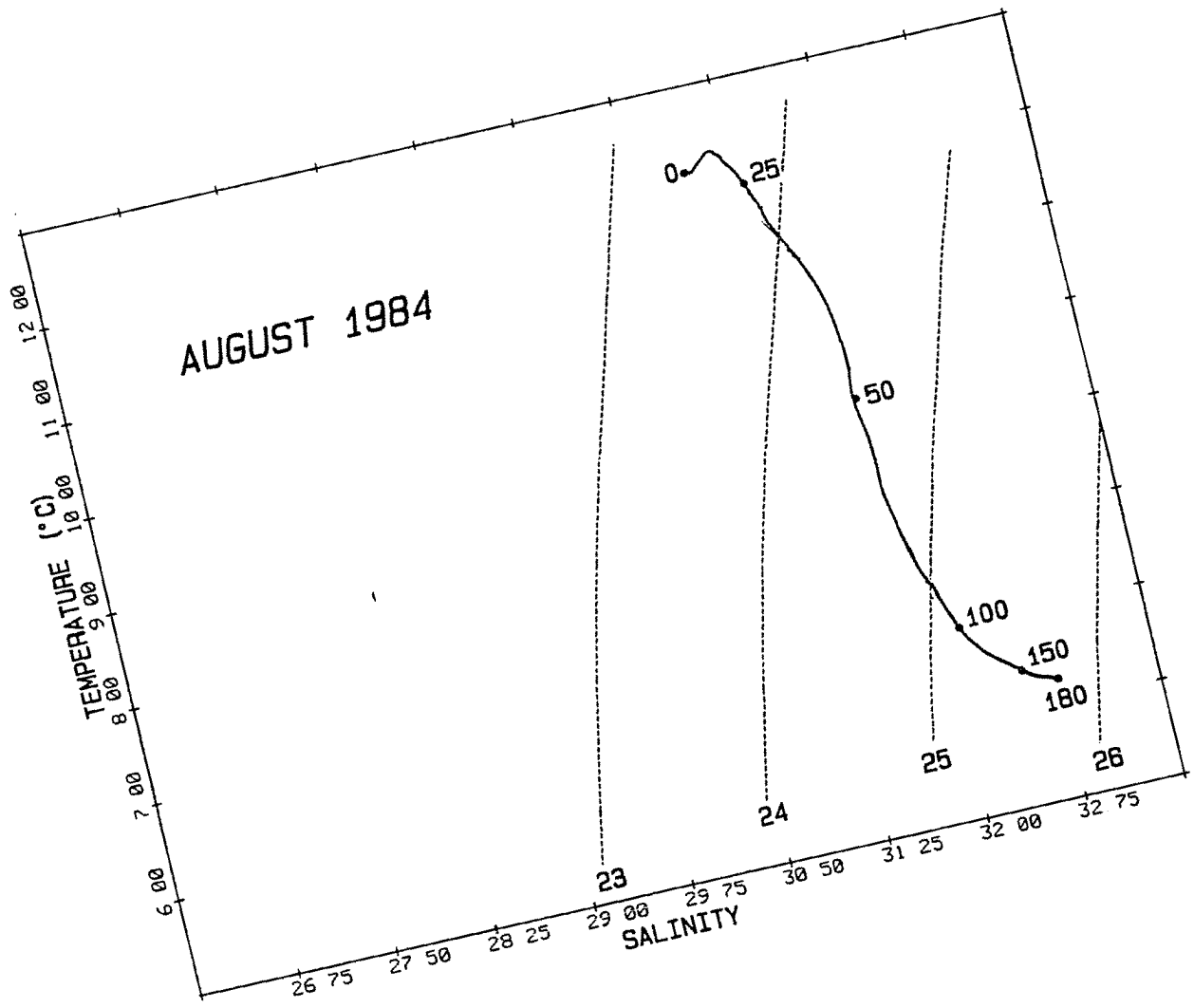

Fig. 3.4g. August, 1984

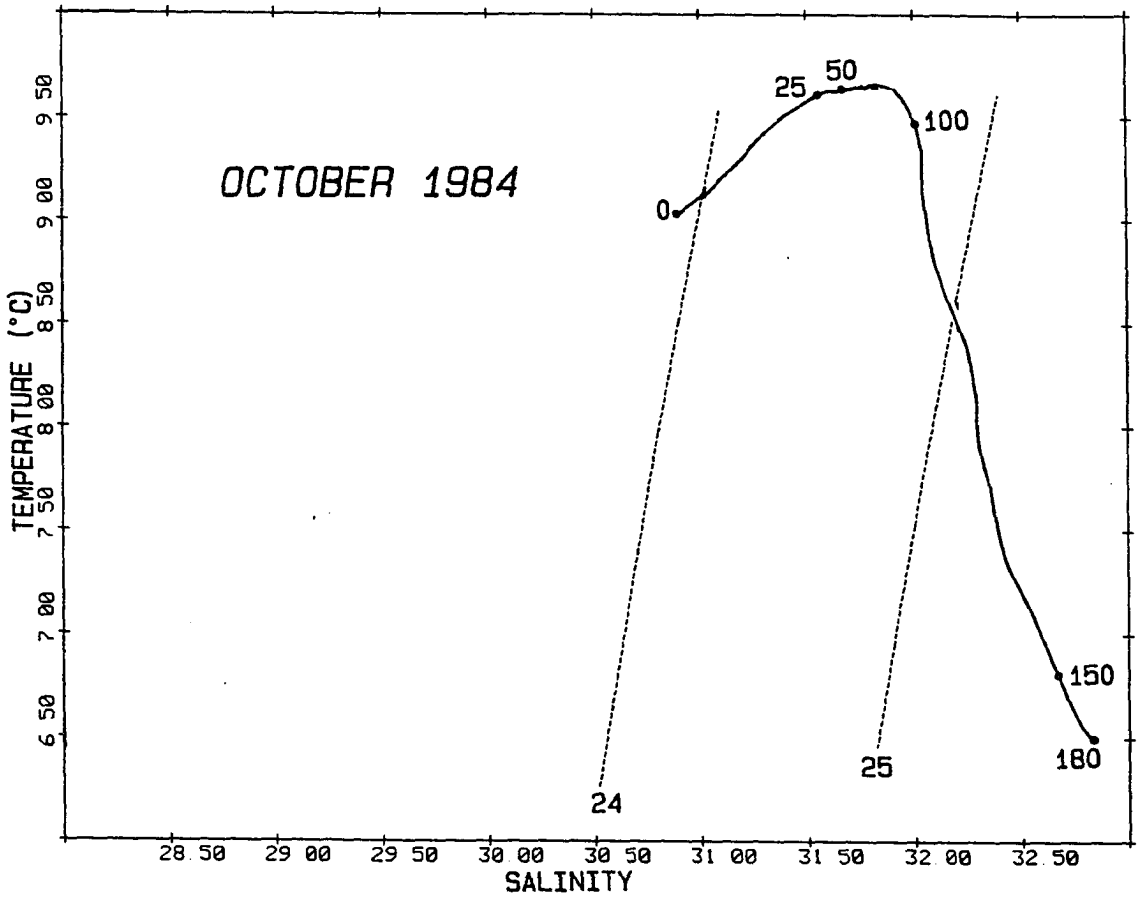

Fig. 3.4h. October, 1984

arrow) causes density to increase with depth. This situation, where stability is maintained by the haline component, appears frequently, particularly in winter. The results are tabulated in Table 3.1 for each of the TS plots in Fig. 3.4. In the "late winter" profile (April, 1983), $\Delta\rho_T$ is negative at all depths. $\Delta\rho_T$ is also negative below 55 m in May, 1984, and near the surface in the late fall (October 1983, and November 1984). $\Delta\rho_S$ is positive in all cases.

In only one instance does the thermal effect play a dominant role in determining the vertical density gradient: in May, 1984, in the upper 25 meters. At this time the gradient of σ_t is minimal, but solar heating has begun to warm the upper layers. Below 25 m the temperature gradient disappears; reversing below 50 m. Stability is maintained by a salinity increase. The situation also occurs three weeks later, on 4 June, when the thermal and salinity effects are equal in the upper 50 m. While the salinity gradient usually maintains the vertical stability, the thermal gradient is an important factor throughout the year.

Table 3.1. Temperature and salinity contributions to change of density with depth at a position just offshore of the mooring.

	Depth Range (m)	Δρ (Total)	Δρ (T only)	Δρ (S only)
9 APR 1983	0/180	0.5	-0.1	0.6
7 JUN 1983	0/180	1.6	0.3	1.3
8 SEP 1983	0/180	4.5	1.1	3.4
25 OCT 1983	0/50	2.1	-0.3	2.4
25 OCT 1983	50/180	2.2	0.6	1.6
10 MAY 1984	0/25	0.1	0.1	0.0
10 MAY 1984	25/55	0.1	0.0	0.1
10 MAY 1984	55/180	0.3	-0.1	0.4
4 JUN 1984	0/50	0.8	0.4	0.4
4 JUN 1984	50/180	0.6	0.0	0.6
16 AUG 1984	0/180	2.2	0.9	1.3
1 NOV 1984	0/80	0.5	-0.3	0.8
1 NOV 1984	80/180	1.2	0.4	0.8

The spring transition from winter to summer conditions is apparent when comparing the April 1983 (Fig. 3.4a) and June 1984 (Fig. 3.4b) TS diagrams. The temperature increases with depth in April; by June the situation has reversed. During this time the salinity range increases by more than one salinity unit, as the top layer freshens and the bottom layer becomes more saline.

The initial stage of fall transition with a temperature "inversion" can be detected in the change between the August, 1984 (Fig. 3.4g) and October, 1984 (Fig. 3.4h) TS diagrams as well as in Table 3.1. This is clearly a "top-down" process caused by cooling at the surface, aided by increasingly vigorous wind mixing and a weakening pycnocline (between 20m and 100m, the August, 1984 change in σ_t is more than one unit; in October, 1984, the change is about half a unit).

The same approach may be taken to investigate which variable establishes the horizontal density gradients. For this purpose the September, 1983 Cape Fairfield section was chosen because of its importance to the model of Chapter 5. In Fig. 3.5 the four curves connect points taken at the same depth at 2 nm intervals offshore. A σ_t front appears at 50 m between stations 3 and 4 (Fig. 3.3). Offshore of this front, the temperature gradient reverses, and decreases in temperature with distance offshore can be seen at all depths. The effect of this decrease is to reverse the horizontal σ_t gradient over a short distance. The reversal is apparently not extensive enough to result in a reversal of the baroclinic, geostrophic current (0/100 db), but it does drop from 109 cm/s to 37 cm/sec (Fig. 3.6). As in the vertical, the change in salinity generally controls the density gradient, with the thermal effect limited to a secondary role, sometimes adding to, and sometimes reducing, the buoyancy driving force.

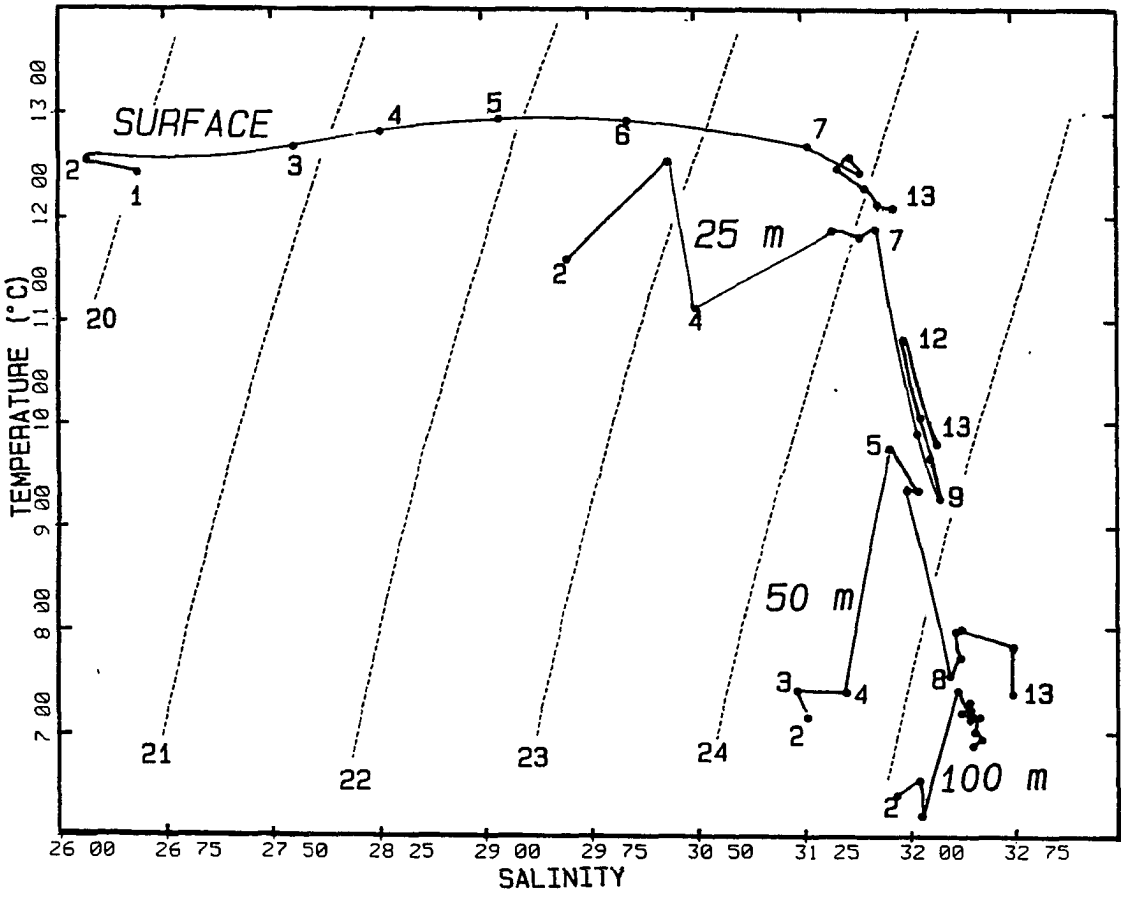

Fig. 3.5. TS diagrams of horizontally distributed points at the following levels: surface, 25 m, 50 m, and 100 m. CF 2 - CF 13, September 8, 1983.

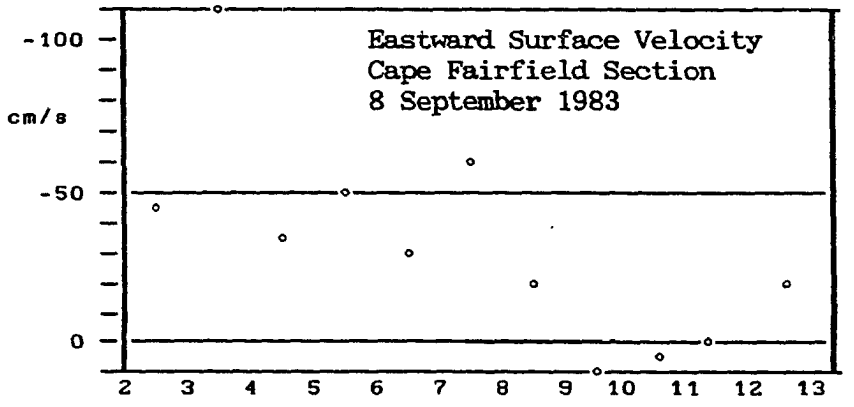

Fig. 3.6 Eastward surface velocity (cm/s), CF 2 - CF 13, computed using the dynamic method, 100 db reference level.

The offshore gradient of σ_t is reversed at the surface between stations 1 (only 27 m deep) and 2. This reversal, which can be seen at the surface in Fig. 3.5, apparently is caused by the meltwater from Excelsior Glacier, just northeast of Cape Fairfield. The outflow flows offshore before turning westward, then flows alongshore separated by $\frac{1}{2}$ and $2\frac{1}{2}$ n.m. from the coast.

3.3 The origins of Blying Sound water masses

Water entering Blying Sound from the east primarily originates from one of two sources (Royer, 1983): the "outside" source, that is, the portion of the ACC which flows along the southern side ("outside") Montague Island (Fig. 1.1), and the Prince William Sound ("PWS") source, which enters Blying Sound between Montague Island and the mainland.

The usual water property cross-sections (Figs. 3.1, 3.2, and 3.3) do not suggest the presence of two distinct water masses over the shelf. When the vertical profiles from each of the stations on a cross-shelf section (the "CF" section) are plotted on a single TS diagram, however, the inner and outer stations can be clearly distinguished (Fig. 3.7). The origins of these two water masses can be traced by reference to the TS diagram (Fig. 3.8) containing all the

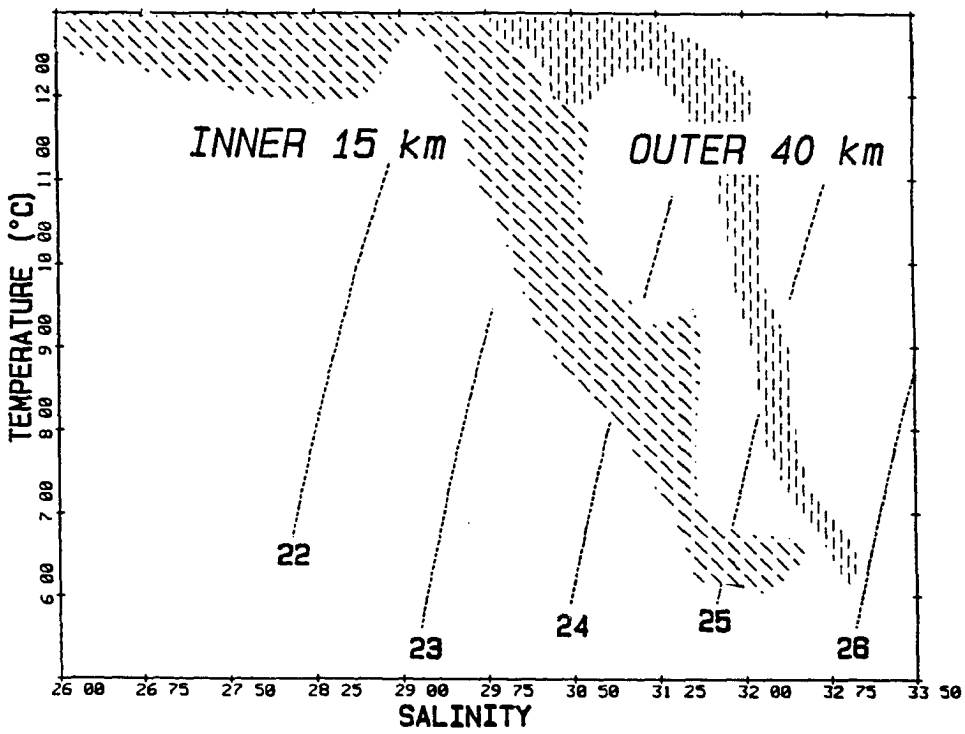

Fig. 3.7. Envelope of TS plots of CF section, 8 Sept. 1983.

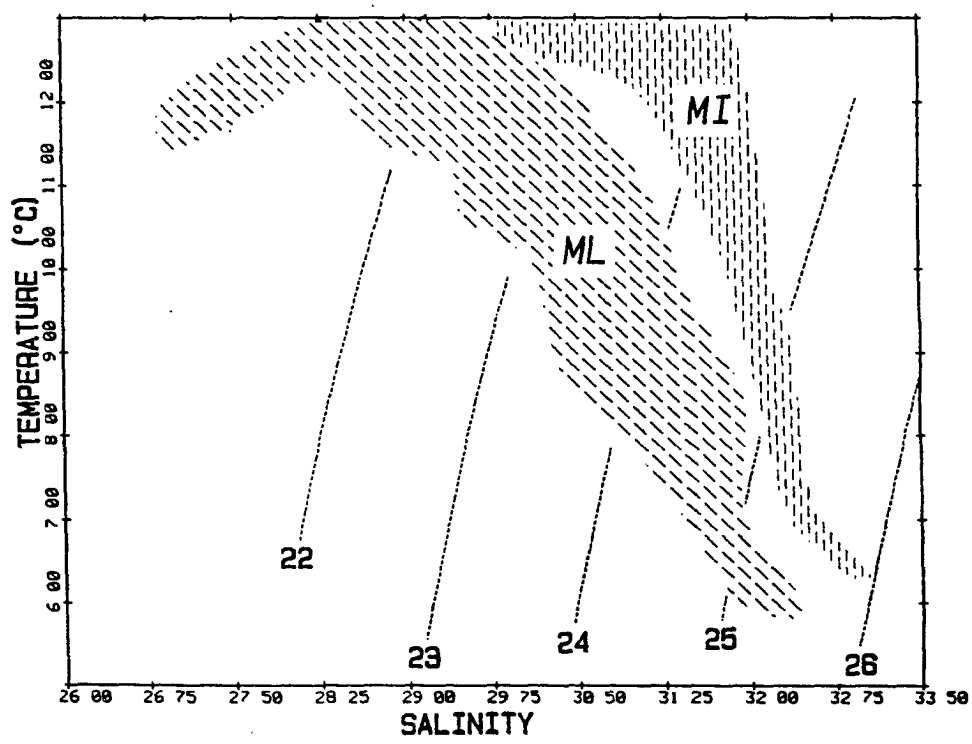

Fig. 3.8. Envelopes of TS plots of MI & ML sections, Sept. 1983.

profiles from two "upstream" sections: the "ML" section, extending across the western exit from Prince William Sound from the continental shore to Montague Island, and the "MI" section, running southward from Montague Island. Only the "envelopes" of the TS curves are shown, not the individual curves. Comparing Figs. 3.7 and 3.8, it can be seen that the TS profiles from the inner 15 km of the CF section (the innermost 4 stations) overlie the ML profiles (i.e., the PWS outflow), and likewise, those outside 15 km overlie the outside waters. It is also interesting to note the narrowness of the envelope containing the "outside" water mass, despite the distance it has travelled since formation in the eastern Gulf of Alaska.

The fate of the PWS outflow in Blying Sound can be traced by use of an alternative polynomial combination of temperature and salinity known as τ (Jackett and McDougall, 1985), also known as the density flux function (Tomczak, 1986) or spiciness (Munk, 1981). Isolines of τ intersect the isopycnals on a TS diagram at approximately 45°. As a result, a cross-section across a portion of shelf composed of two water masses of similar densities may have horizontal isopycnals, and yet show a distinct vertical front in the contours of τ (Luick *et al.*, 1987b). The oceanographic significance of τ is its usefulness in the discrimination water masses; it does not appear to have any intrinsic dynamical meaning. The actual magnitude is a matter of definition; the range over which it varies, arbitrarily selected as a matter of convenience, is similar to that of σ_t (Jackett and McDougall, 1985).

The ML section (PWS outflow, Fig. 3.9a) was composed almost entirely of water of $\tau<22.3$, while the MI section (outside PWS, Figure 3.9b) was almost entirely $\tau>22.3$ (the number 22.3 is simply a characteristic cutoff value). The AC section (Fig. 3.9c) is very similar to the MI section, indicating that the coastal current follows the bottom contours (Fig. 2.1) turning northward around Montague Island. After entering Blying Sound, the PWS outflow moves at maximum velocities of between 25 and 125 cm/s westward (Johnson *et al.*, 1988), being joined immediately by the coastal water flowing around Montague

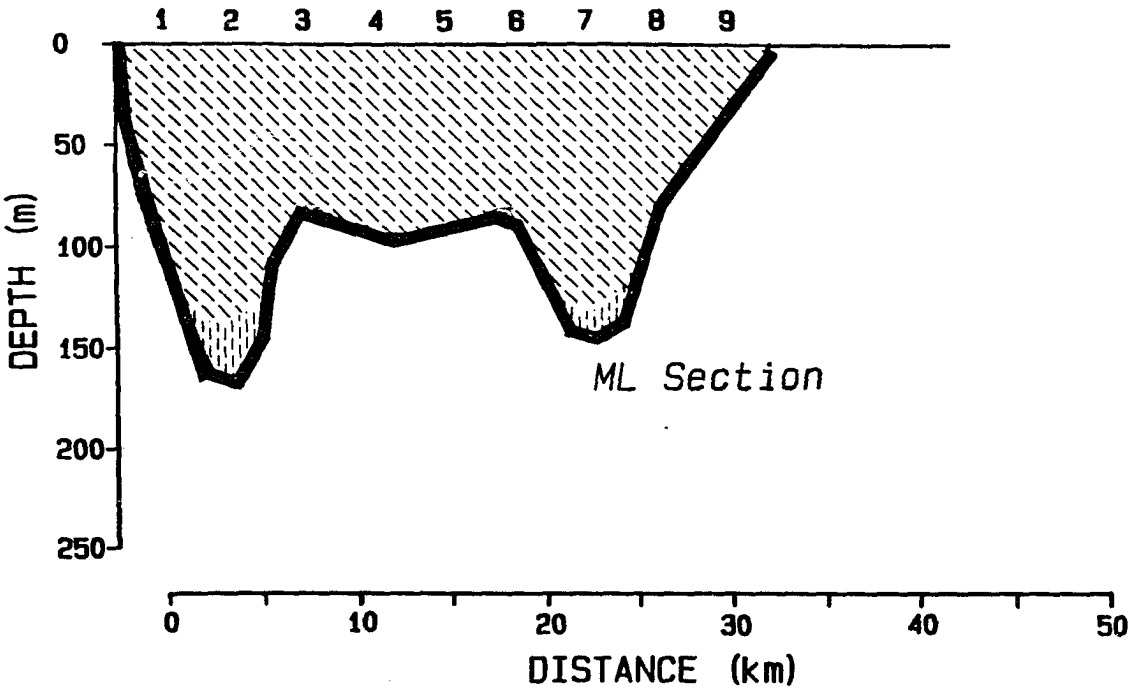

Fig. 3.9a. ML Section

Fig. 3.9. Density flux function (τ) for consecutive sections, September, 1983. For locations of sections see Fig. 2.1. The diagonally hatched region denotes $\tau<22.3$; the vertically hatched region denotes $\tau>22.3$. The hatching corresponds approximately to that of Figs. 3.7 and 3.8.

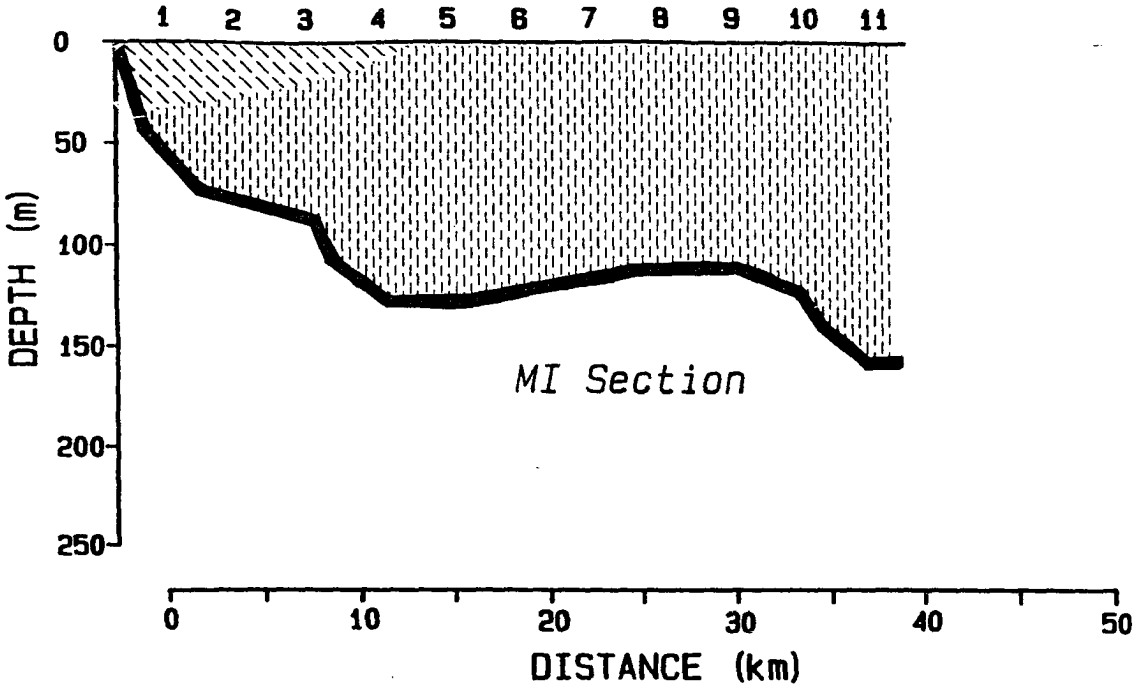

Fig. 3.9b. MI Section

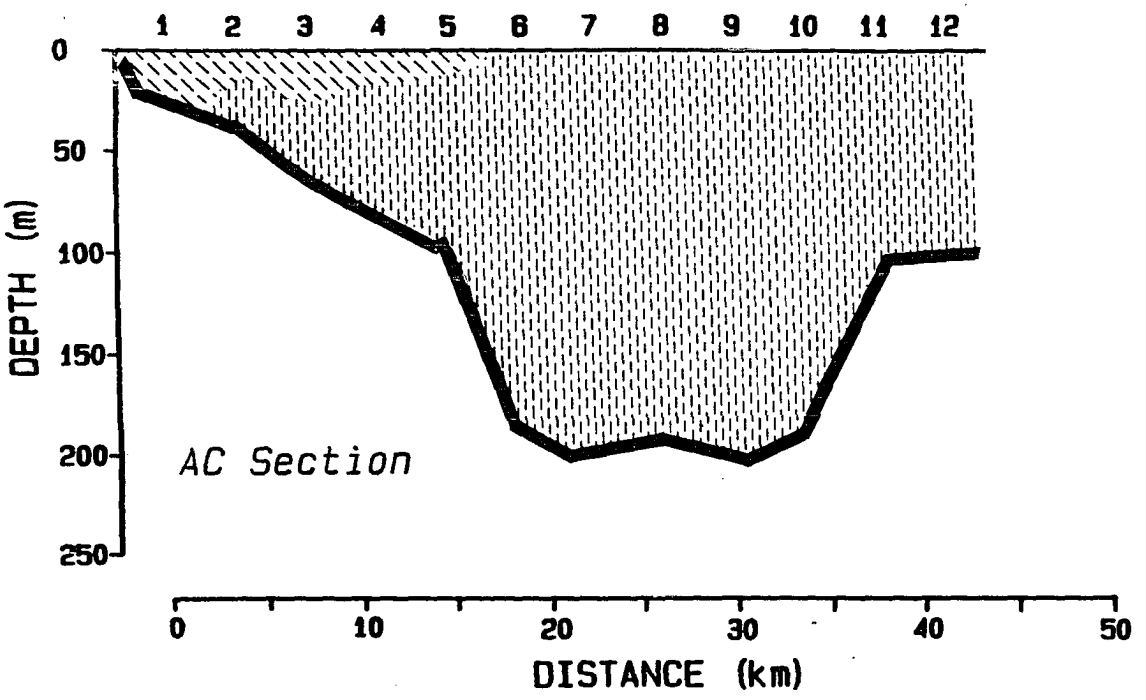

Fig. 3.9c. AC Section

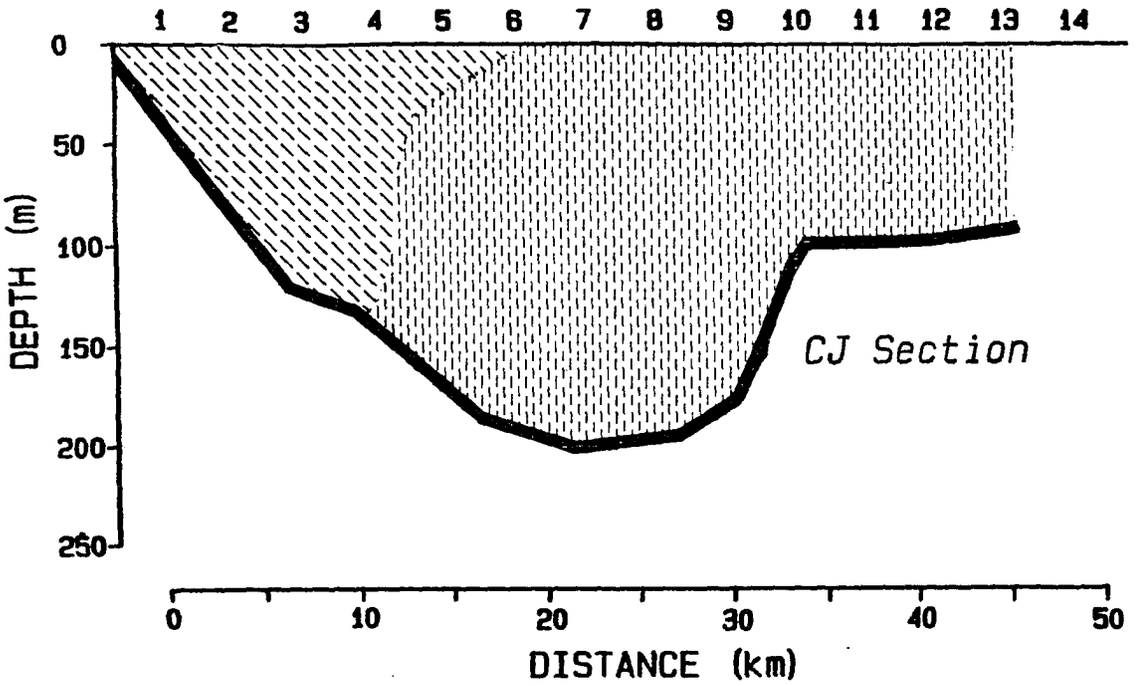

Fig. 3.9d. CJ Section

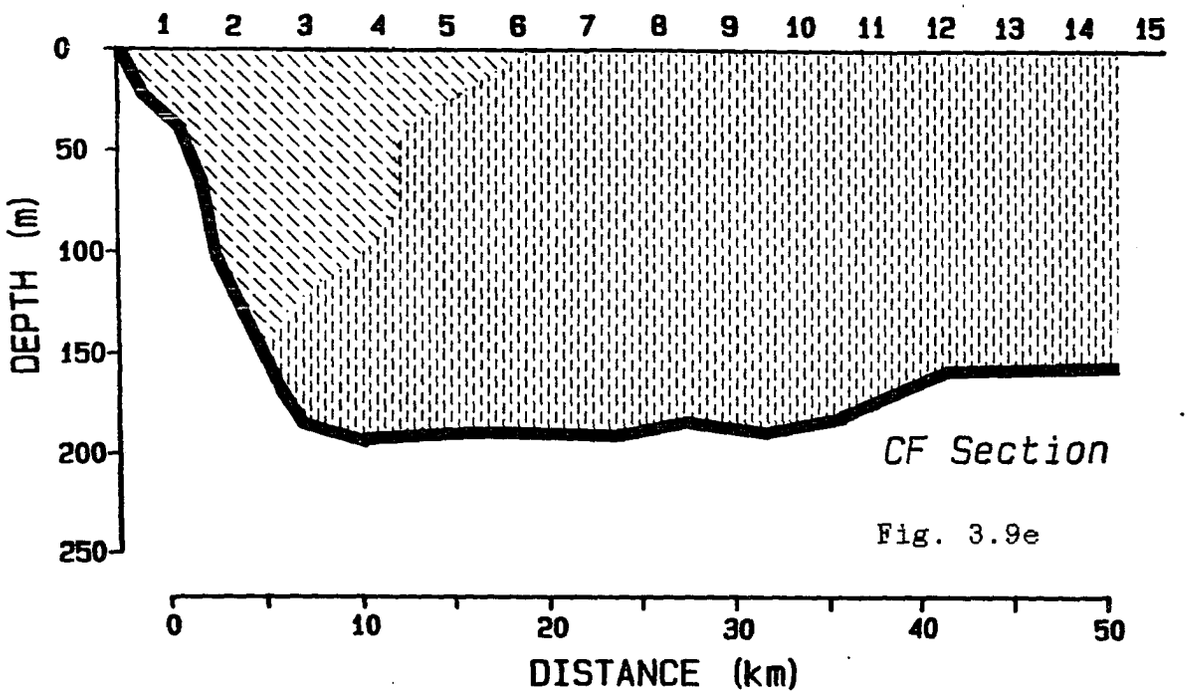

Fig. 3.9e

Fig. 3.9e. CF Section

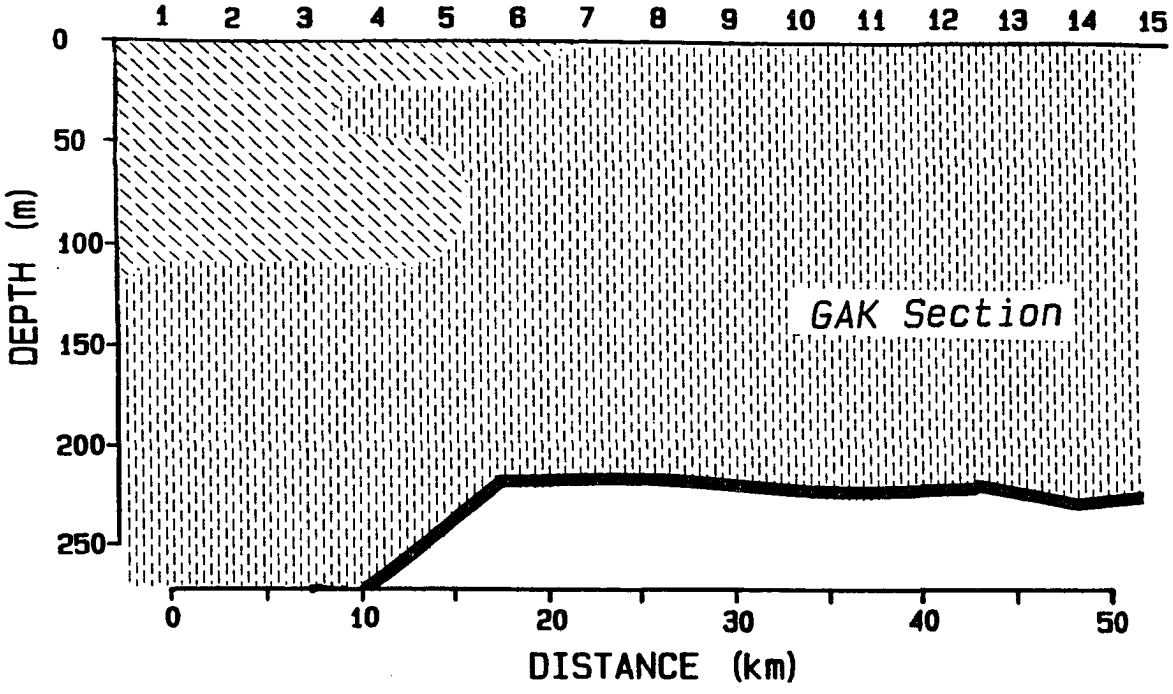

Fig. 3.9f. GAK Section

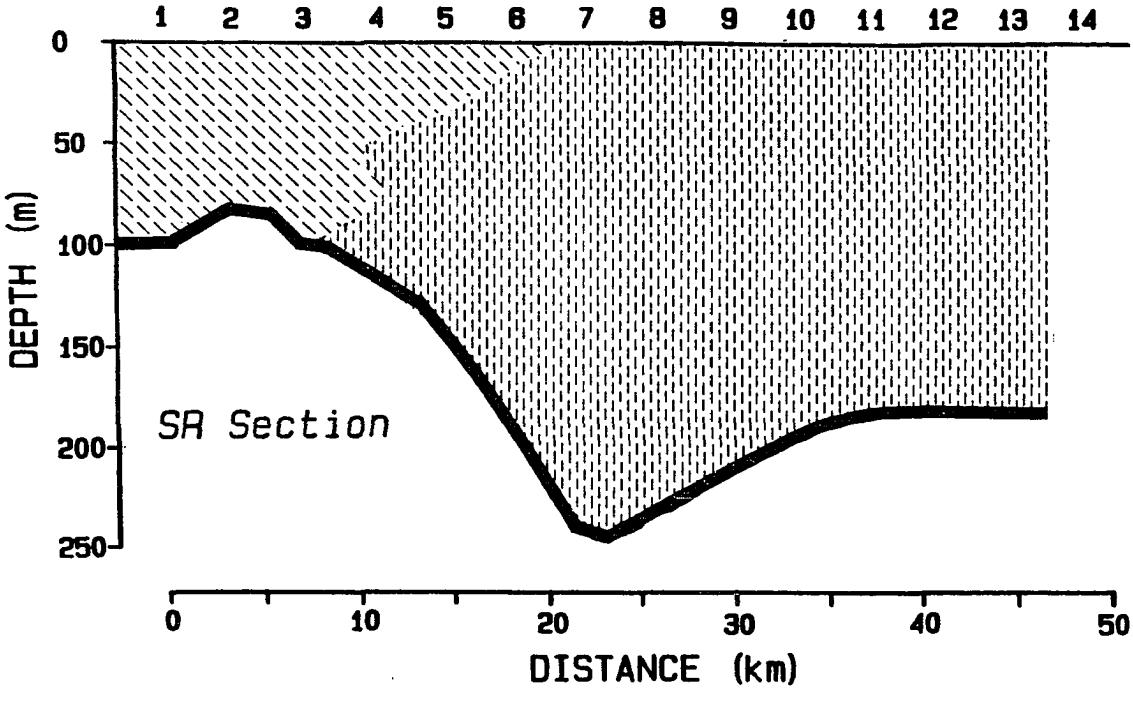

Fig. 3.9g. SR Section

Island. Sections CJ, CF, GAK, and SR (Figs. 3.9d, 3.9e, 3.9f, and 3.9g) intersect the coastal current consecutively further downstream. Through all these sections, a traverse requiring about 4 inertial periods, the PWS outflow remains a distinct water mass on the inner shelf.

3.4 Fresh water inflow per unit coastline

Royer (1981) presented a hydrologic model of the Gulf of Alaska coastline which estimated the total runoff based on precipitation, temperature, and glacial meltoff. Inasmuch as Prince William Sound acts as a dilution basin with a known shoreline length, it serves as an independent test of the model. This is the first attempt to verify the hydrology model using marine salinity observations.

If the $\tau<22.3$ area in Fig. 3.9d (from September 1983) is assumed to represent PWS outflow, then together with estimates of speed and salinity anomaly, the total freshwater entering PWS through the coastline can be approximated as:

FWO (m^3/s) = AREA (m^2) X ANOMALY (%) X SPEED (m/s)

where

FWO = is the net freshwater flux out of PWS which did not enter PWS via Hinchinbrook Entrance,

AREA = 15×10^3 is the vertical cross-sectional area of discharge from PWS, assumed to be equal to the region where $\tau<22.3$ in Figure 3.7d,

ANOMALY = 10 % is the salinity defect between the PWS discharge and the portion of the ACC flowing south of Montague Island, and

SPEED = 15 cm/s is the average speed of the PWS discharge. This value was arrived at by averaging the 0/50 db geostrophic velocities across the ML section.

With these estimates, FWO = 2.25×10^4 m^3/s .

Dividing the total freshwater input to PWS (FWO) by the length of the PWS coastline, 600 km, the estimated discharge per meter coastline is .037 $m^3/s/m$. The hydrologic model of Royer (1981) was used to

estimate the September, 1983 discharge; according to the model, the total influx for the entire coastline between Yakutat and Seward, Alaska, was 20,655 m^3/s. Dividing this estimate by the 600 km drainage area quoted in the model, the discharge per meter coastline is .034 $m^3/s/m$.

Interpretation of the above result is complicated by the fact that two different definitions of coastline length have been used. The 600 km drainage area of Royer (1981) is the length of a smooth arc extending from Yakutat to Seward, Alaska, including the entire PWS coastline. The coastline used here is the actual PWS coastline, itself approximately 600 km in length. It can be argued that a major portion of the freshwater entering the coast between Yakutat and Seward directly enters PWS, thereby eliminating the difficulty. However, the primary purpose of this section is to demonstrate a potentially useful check, whose full exploitation is beyond the scope of the thesis.

3.5 Dynamic topography and the density distribution

The method of "dynamic topography" can be used to provide an integrated view of the density distributions. Two maps are presented to illustrate extreme conditions. Dynamic heights are referenced to 100 db. The first (Fig. 3.10), from April 1983, exhibited the minimum relief; this is the season of minimum baroclinic, geostrophic transport (Chapter 4, Table 4.1). The density contrast across the shelf is weak owing to reduced coastal discharge, but the ACC and the PWS discharge are still evident. The second map (Fig. 3.11), from September 1983, exhibits the maximum relief, and likewise, maximum transport . The dynamic height is largest near the coast (0.155 dyn. m) and is relatively small (0.025 dyn. m) in the offshore region.

The 0/100 db baroclinic geostrophic current is proportional to the gradient of 0/100 db dynamic topography and theoretically follows

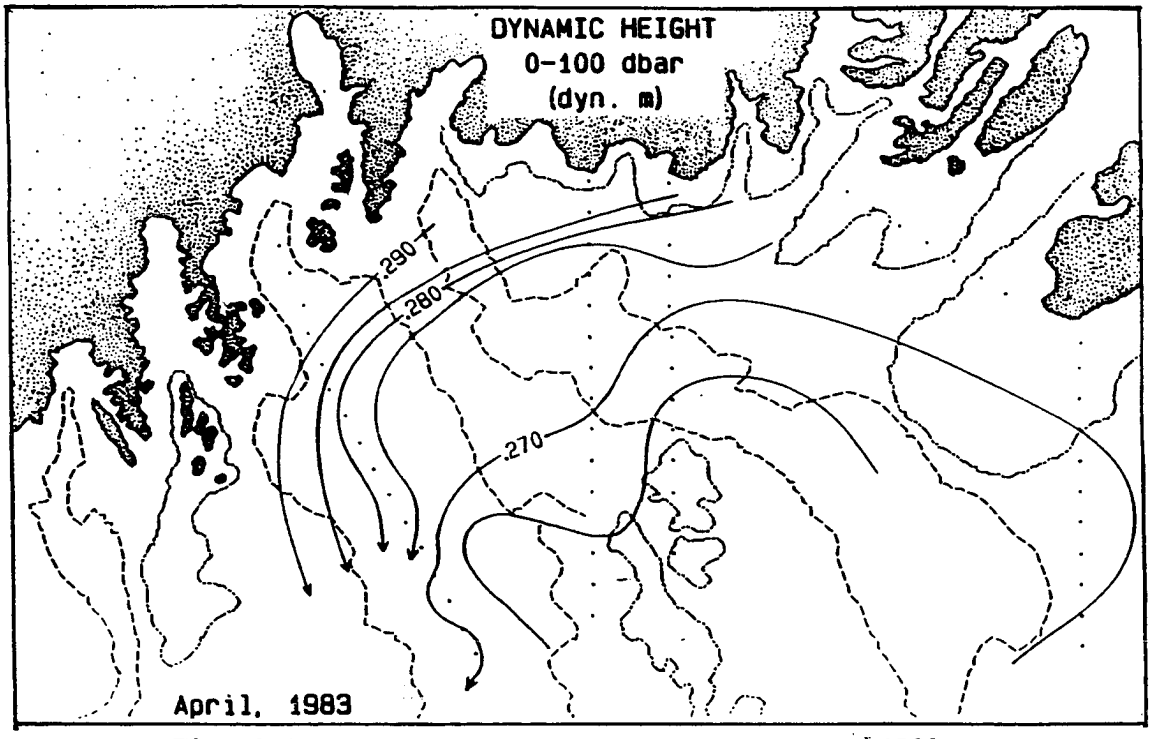

Fig. 3.10. Dynamic height topography, April, 1983.

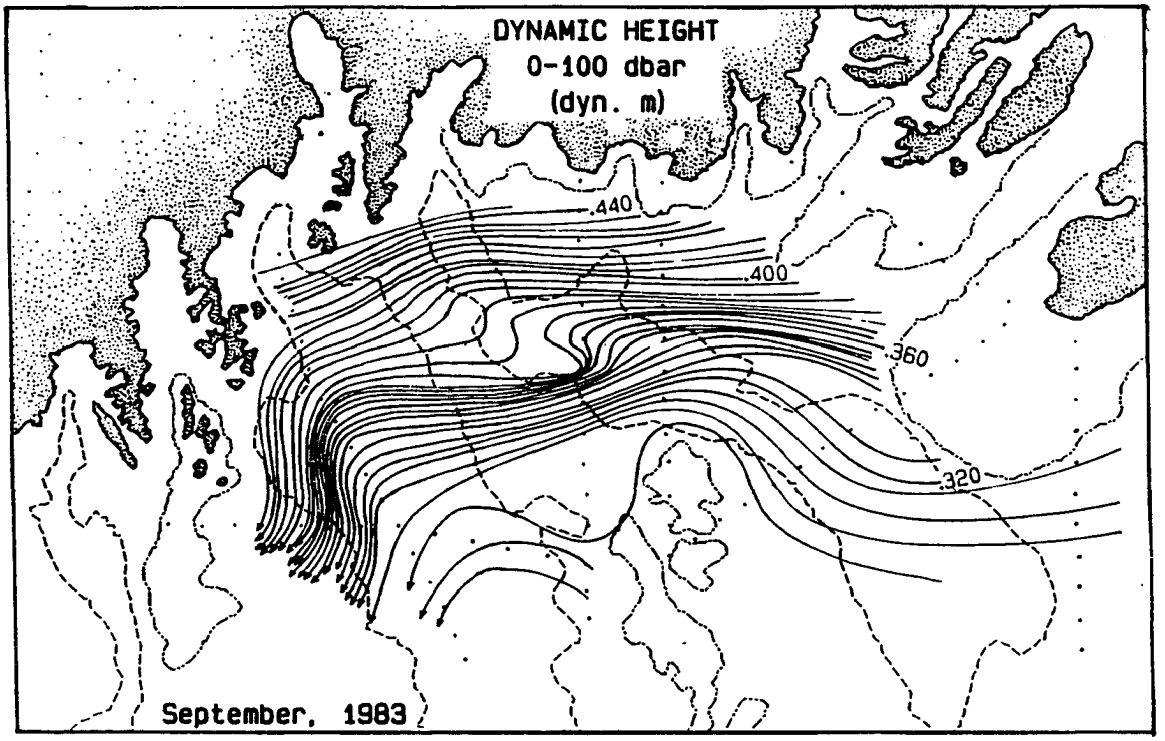

Fig. 3.11. Dynamic height topography, September, 1983.

its contours. Figs. 3.10 and 3.11 demonstrate that this component of the flow does not follow the isobaths in a region of large bathymetric variability. Some turning does occur around the shoaling region in the middle shelf, and some distortion is associated with the 175 m channel running diagonally between the shoal and the shoreline. In the triangular region between the CF line and the GAK line the positioning of the contours is somewhat speculative due to the lack of coverage. Considering the fact that the scale of topographic variability is approximately equal to the two-layer Rossby radius (Royer, 1981), it is possible that significant detail is lost, particularly during periods when the dynamic topography shows significant curvature. For example, in September 1983 (Fig. 3.11), the distortion over the 175 m channel in the vicinity of the CF and CJ transect crossings may actually extend northwestward (further up the shelf), but it is not possible to resolve with the available data. Conversely, the similarity of the water properties of widely separated transects discussed in section 3.3 supports the smoothed appearance of the dynamic topography, and by extension, the hypothesis that the flow is detached from bottom irregularities. In the following chapters the bottom topography will be shown to exert a strong influence on the path of the ACC.

Chapter 4. OBSERVATIONS OF TRANSPORT AND VARIABILITY

In this chapter the transport along and across the shelf is described using the data from the moored current meters and the profiling current meter. There are several reasons why such a description is required. The velocity field predicted by the steady state model of Chapter 5 is premised on the assumptions that high frequency fluctuations such as tidal currents average to zero over a cycle, and that accelerations associated with lower frequency changes contribute relatively small terms to the momentum balance. The observations of transport and mixing are necessary to determine the temporal scales of motion over the shelf, and will be important in the interpretation of the model results. There is also an intrinsic value in the observational evidence, not directly connected any particular model. This often takes the form of a statistical description, such as the depth/phase progression of water properties over seasons discussed by Luick *et al.* (1986). The observational evidence will be particularly valuable to the to the characterization of transport and variability in the cross-shelf direction.

4.1 Mixing across the shelf

Where the continental shelf is repeatedly cut by underwater canyons and the shoreline is highly irregular, "cross-shelf" is not generally synonomous with "cross-isobath". In other words, a coastal current following an average shoreline must repeatedly cross isobaths. In order for a line source of buoyancy acting along the average shoreline to maintain a wedge-like band of fresh water (often used as a convenient idealization), net "offshore" advection is required to replace loss due to entrainment, across the outer leg of the wedge. This "offshore" flow may in some cases be along isobaths. One difficulty of applying analytic models in such an area is that it is impossible to simplify the geometry to a sufficient extent without sacrificing the physical meaning.

The current meter data can be used to define a rotation angle for the along- and cross-shelf components. In a topographically complex region, the area over which the computed angle is valid is limited. In the case of the COJET moorings, this range probably extends less than 50 km offshore, the approximate distance between the mooring and the shoaling region to the south.

Two methods were used to compute an angle of rotation. The first method calculates the major axis orientation θ, or clockwise rotation from true north of the axis of greatest variance (Kundu, 1976):

$$\theta = \frac{1}{2} \tan^{-1} \frac{2\langle uv \rangle}{\langle u^2 \rangle - \langle v^2 \rangle} .$$

Here, the brackets denote the time average. This is also the angle which makes the covariance between the north and south components of the flow equal to zero. The second method, which requires considerably more effort, computes an angle from the smoothed co- and quadrature spectral estimates (Jenkins and Watts, 1968; see, for example, eq. 9.3.11). This is a function of the frequency band selected. The method also gives an estimate of smoothed squared coherency, sometimes called "ellipse stability", a measure of the reliability of the angle.

The above analyses were carried out using 200 days of data starting 11 September 1983. This segment was chosen to encompass the period of maximum flow. The data were lowpass filtered with a half-power period of 35 hours. The results were similar for the 50 m, the 70 m, and the 110 m current meters. Using the Kundu (1976) technique, the major axis orientation, θ, was $270^\circ \mp 3^\circ$.indicating zero rotation. For the Jenkins and Watts technique, the results were very similar for the three depths. The only frequency with significant ellipse stability was $10^{-6} s^{-1}$, correspondeding to a period of 11 days. The major axis direction for this frequency was also 270°. Therefore, no rotation was performed on the data, and the general east-west trend of the coastline was taken to define the alongshore component in the vicinity of the current meter mooring.

The maps of dynamic topography (Figs. 3.10 and 3.11) provide a broadened perspective to the discussion of cross-shelf exchange

because the irregularities in the bottom and short term temporal fluctuations tend to be smoothed out, while retaining much of the overall effect of buoyancy and wind forcing as well as the bottom topography. "Cross-shelf exchange" can then be defined as the transfer of properties between the shoreline and the middle shelf. In Blying Sound, which has a shoaling region 50 km offshore, the term may apply both along and across isobaths.

The primary mechanism by which transfer occurs across the continental shelf is advection (Csanady, 1982). The advecting flow may be a steady cross shelf circulation, a short term pulse such as a response to a wind storm, a oscillatory tidal current, a deep compensation current (often associated with flow up a submarine canyon), a headland plume or separation, a small scale eddy, or a chaotic fluctuation. Ahlnaes *et al.* (1987) presented satellite photographs of the coastal current in the region of Kayak Island, just offshore in the Northeast Gulf of Alaska, in which a turbid plume and numerous small ($\approx$ 26 km) eddies are visible separating from the coast. In the following, the effect of processes which advect salt and heat but are independent of the mean alongshore flow, are assumed to be sufficiently constant in time that mixing may be represented by a single coefficient of turbulent diffusion.

In Chapter 3, the cross-sections of τ (Fig. 3.9) indicated that water flowing out of PWS retained its identity after entering Blying Sound and as it continued westward along the coast. Between 50 and 100 m depth, however, a tongue of PWS water appears to extend further offshore in successive sections (Figs. 3.9 d through g). The extension may be partly due to mixing at the interface, either by oscillatory tidal currents or by turbulence. This possibility is not ruled out by the current meter evidence. During the period in question, the standard deviation of the offshore flow at the 76 m current meter was larger than the mean of the residuals (6.18 cm/s vs. 5.2 cm/s southward; the residuals were formed by subtracting six primary tidal constituents from the time series, which had already been low-pass filtered with a half-power period of 2.86 hours in order

to reduce the high frequency noise). However, the net effect of mean flow advection for property transfers, when present, generally far outweighs that of turbulent diffusion in stratified shelf waters (Csanady, 1982). The ratio of horizontal advection and diffusion terms (the Peclet number) in the advection - diffusion equation for salt (or heat, with $k = k_s \approx k_t$, where k_s and k_t are coefficients of turbulent diffusion of salt and heat), is $\frac{V \cdot L}{k}$. Here v is a typical cross shelf velocity and L is a typical length scale. Estimates of k vary between 10^2 cm^2/s and 10^4 cm^2/s (Ramming and Kowalik, 1980; Csanady, 1982). With v = 5 cm/s, $L = 5 \cdot 10^5$ cm, and $k = 10^2$ cm^2/s the ratio equals 25,000. If $k = 10^4$ cm^2/s, the advective effects still outweigh diffusion by a factor of 250. While turbulent diffusion may have a significant local effect such as the distortion of an interface, advection is of greater significance to net transport.

If the tongue of PWS water extending further offshore in successive sections in Fig. 3.9 is due to advection, it should provide a check on the mean offshore flow just discussed. The mean September offshore flow at 76 m is 5.2 cm/s. The tongue appears to move approximately 1 km offshore per 8 km downstream travel; that is, at an average alongshore speed of 40 cm/s (at the location of the front), an offshore speed of 5 cm/s is implied. While the two estimates show good agreement, the result should be taken as qualitative, due to the approximations involved.

Offshore flow at mid-depth is predicted by the basic "Ekman model" in the presence of wind blowing with the shore on its right in the northern hemisphere (e.g., see Neumann and Pierson, 1966). Johnson *et al.* (1988), using statistical mode analysis on the monthly-averaged data, found that increased westward (alongshore) winds in fall were accompanied by increased offshore (southward) flow at the 70 m current meter, in keeping with the Ekman model. This offshore flow may not, however, be due to the dynamics of the Ekman model. For example, during the week prior to occupying the sections shown in Fig. 3.7 (Sept. 1 through Sept. 7, 1983), the FNOC derived wind was directed generally to the southeast (Fig. 4.1), for which the Ekman model would

predict onshore flow. This contradicts the 5.2 cm/s offshore flow at 70 m previously discussed. Likewise, the statistical result at the surface (Johnson *et al.*, 1988), was that when the downwelling-favorable winds increased in fall, the surface current meter recorded more southward (offshore) flow, too, in opposition to the Ekman model. It is likely that additional considerations, such as the complex bottom topography, are required to avoid misleading conclusions based on simpler models.

The offshore flow at mid-depth in September contradicts Kao (1981). In a three dimensional model of a buoyancy driven coastal current, onshore flow at mid-depth was predicted over the inner shelf at equilibrium. Equilibrium was said to occur 14 inertial days following a freshening event. Several explanations are possible for the contradiction. These include the alongshore length scale, the time scale, and wind, which was not included in the Kao model. In particular, the southward-trending bottom just onshore of the mooring deflects the flow offshore. This illustrates the difficulty of applying analytic coastal circulation models to the ACC region.

A number of unanswered questions have been raised in the foregoing discussion. At this point, the "dynamic method" is turned to in order to provide a qualitative description of the flow. The focus will continue to be on the September, 1983 data. This was a time when buoyancy effects were clearly visible in the data, winds were relatively light, two PCM sections were performed, and all the current meters were operative. However, perspective will first be broadened to include every available instance when the CF section was occupied.

4.2 Baroclinic, geostrophic transport

In this section the westward (approximately alongshore) baroclinic, geostrophic (BG) transport of the ACC will be presented in order to describe the "shape" of the ACC. Unless otherwise explicitly

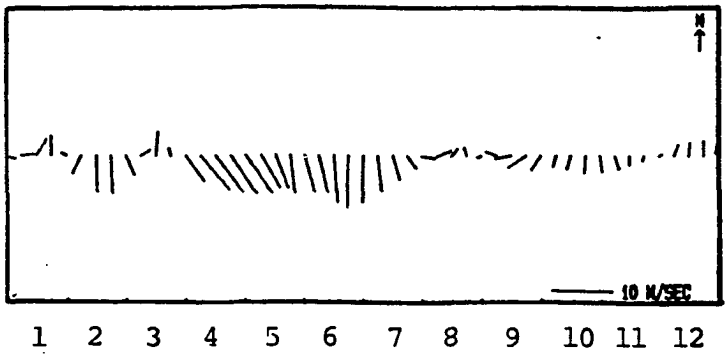

Figure 4.1. Wind vectors at 60 N, 149 W, Sept. 1 - 12, 1983.

stated, transport will refer to the westward component of transport.

The CF section was used to compute the BG transport over the upper 100 db. CF sections occupied prior to and since the COJET project are included in Table 4.1. The largest BG transport, 0.46 Sv, occurred in November, 1986. This transport occurred within the first 22 km (first seven stations). Beyond this, the circulation reversed. This is usually apparent in Table 4.1 since the the transport for column e, the transport between CF2 and the pair where the circulation drops to zero or reverses, is larger than column c, the transport over the entire line. Of the 42 sections in Table 4.1, this situation, where the net transport is eastward "outside" of a pair where it goes to zero, occurs 17 times. Over the inner portion, the transport was always westward, and it becomes zero somewhere along the section. On five occasions, notably HX 104 (10 September 1987), the pair with the largest transport (column f) was outside the pair where it went to zero. The above description is consistent with the observations of occasional double maxima, and occasional reversals in the outer portion observed in the profiling current meter cross-sections (Johnson *et al*, 1988).

It was pointed out in Johnson *et al.* (1988) that the PCM transports are generally much higher than the 0/100 db BG transports. Rapidly changing components and any other nongeostrophic, baroclinic components are not included in the BG computation. Also, the selection of a "level of no motion" (where pressure surfaces are level) is rather arbitrary particularly over the shelf. As a test of how much BG transport was missed by excluding the portion of the water column between the bottom and 100 db, the BG transport computation was repeated using the deepest common depth of each station pair as the level of no motion. The September 8, 1983 CF section was chosen for this comparison. The result (Fig. 4.2) indicates that the choice of a 0/100 db surface does underestimate the BG transport, in this case by about one fifth. Qualitatively, the results are unchanged: in both cases, the increase in BG transport is greatest inside station pair CF 5/6, then increases little or not at all between stations CF 6 and

Table 4.1 Westward baroclinic, geostrophic transport and velocity for CF sections, 1980 through 1988. All transports are in Sv ($10^6 m^3/s$), and all computations are for 0/100 db. By column:

a) Cruise Number
b) Date of start of section
c) Westward transport between stations CF 2 - CF 13
d) Outside boundary (station pair where transport goes to zero or turns eastward)
e) Westward transport between station CF 2 and pair in column d
f) Station pair with maximum westward transport
g) Transport of pair in column f
h) Maximum velocity (cm/s) of pair in column f.

(see following page...)

a	b	c	d	e	f	g	h
HX 10	21 NOV 1980	.34	CF11/12	.36	CF2/3	.07	54.9
HX 23	14 NOV 1981	.45	CF8/9	.40	CF3/4	.10	55.8
HX 23	14 NOV 1981	.45	CF12/13	.45	CF5/6	.08	67.0
HX 23	15 NOV 1981	.40	CF12/13	.40	CF2/3	.08	41.4
HX 24	18 NOV 1981	.36	CF4/5	.11	CF9/10	.12	82.5
HX 24	21 NOV 1981	.35	CF5/6	.22	CF3/4	.09	82.5
HX 24	22 NOV 1981	.38	CF12/13	.38	CF3/4	.09	57.5
HX 24	23 NOV 1981	.37	CF11/12	.38	CF2/3	.12	88.0
HX 24	23 NOV 1981	.36	CF5/6	.27	CF3/4	.13	77.2
HX 24	23 NOV 1981	.31	CF11/12	.33	CF2/3	.13	78.8
HX 30	20 JUL 1982	.23	CF8/9	.15	CF4/5	.06	52.1
HX 37	11 NOV 1982	.38	CF12/13	.41	CF2/3	.07	45.7
HX 37	11 NOV 1982	.23	CF12/13	.23	CF2/3	.08	59.7
HX 42	2 APR 1983	.08	CF6/7	.05	CF2/3	.04	26.3
HX 42	7 APR 1983	.07	CF9/10	.05	CF2/3	.02	16.4
HX 42	8 APR 1983	.09	CF6/7	.06	CF8/9	.03	20.7
HX 42	9 APR 1983	.05	CF8/9	.08	CF5/6	.02	12.8
HX 45	7 JUN 1983	.22	CF7/8	.21	CF4/5	.07	38.4
HX 45	8 JUN 1983	.15	CF11/12	.17	CF5/6	.05	33.1
HX 45	10 JUN 1983	.18	CF9/10	.19	CF5/6	.05	39.3
HX 45	11 JUN 1983	.20	CF12/13	.20	CF2/3	.05	33.4
HX 51	7 SEP 1983	.29	CF6/7	.15	CF7/8	.09	102.3
HX 51	8 SEP 1983	.34	CF9/10	.32	CF7/8	.07	60.6
HX 54	25 OCT 1983	.39	CF10/11	.40	CF6/7	.10	43.9
HX 55	9 MAY 1984	.17	CF12/13	.19	CF2/3	.05	36.8
HX 58	4 JUN 1984	.08	CF10/11	.10	CF3/4	.03	26.5
HX 58	7 JUN 1984	.12	CF9/10	.12	CF2/3	.03	17.5
HX 61	14 AUG 1984	.10	CF3/4	.04	CF11/12	.05	25.6
HX 61	15 AUG 1984	.15	CF5/6	.06	CF10/11	.07	51.7
HX 65	30 OCT 1984	.33	CF7/8	.36	CF6/7	.09	44.5
HX 65	2 NOV 1984	.14	CF8/9	.24	CF6/7	.07	29.4
HX 67	26 MAR 1985	.17	CF11/12	.18	CF2/3	.05	27.1
HX 79	14 MAR 1986	.21	CF8/9	.22	CF2/3	.08	38.6
HX 79	15 MAR 1986	.14	CF6/7	.14	CF2/3	.07	45.4
HX 81	11 MAY 1986	.11	CF10/11	.01	CF2/3	.05	20.5
HX 92	11 NOV 1986	.43	CF10/11	.46	CF7/8	.09	54.0
HX 94	12 DEC 1986	.35	CF9/10	.34	CF2/3	.08	66.9
HX 95	17 FEB 1987	.17	CF6/7	.18	CF2/3	.06	34.9
HX 98	24 MAY 1987	.16	CF8/9	.21	CF2/3	.04	38.1
HX 104	10 SEP 1987	.18	CF7/8	.13	CF8/9	.06	38.2
HX 108	1 DEC 1987	.35	CF7/8	.29	CF3/4	.08	54.2
HX 111	4 APR 1988	.21	CF11/12	.21	CF2/3	.06	33.1

CF 7, then undergoes a secondary increase at station pair CF 7/8 (a double maximum).

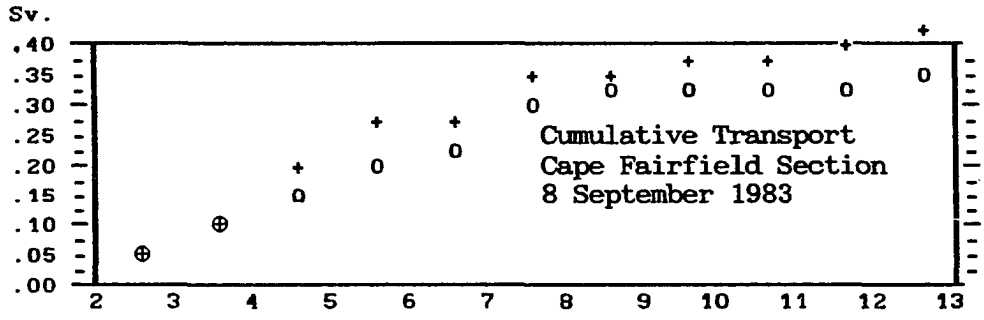

Fig. 4.2. Cumulative transport (westward) for the CF section, CF 2 - CF 13. Transport computed using the dynamic method, and two reference levels: (o) = 100 db, (+) = deepest common depth of each pair.

Between November 14 and November 23, 1981, the CF section was occupied nine times (Table 4.1). Although the 0/100 db transport between the shore and the pair where the transport was zero or reversed varied by a factor of four during that period, the total transport was comparatively steady, with a mean of .38 Sv and standard deviation of .05 Sv. A similar situation was discussed in Luick *et al.* (1986), in the data from the cruise HX 42 (Table 4.1) in April, 1983. It was observed that, in response to a storm which occurred after the first time the CF line was occupied on HX 42, the cross-sectional distribution of density at the CF section was radically altered, but the total transport was unchanged. What apparently happens is the core of the ACC moves back and forth across the shelf, occasionally splitting to form a double maximum; this apparently can occur in less than one a day. This is a possible explanation for the observation that within a cruise, the pair with maximum transport frequently changes (Table 4.1, column f). In most instances, the transport of the new pair is essentially the same. The variability of the offshore position of the core is associated with the internal density distribution.

The apparent unresponsiveness of the BG transport to local wind

events does not mean that significant changes in the transport do not occur over two or three days. During cruise HX 65 (October/November 1984), the total BG transport underwent more than a twofold change in less than three days (Table 4.1). Evidence exists that wave or surge-like features do periodically cause large short term changes in the local transport. In September, 1983 (Table 4.1 and Johnson *et al.* 1988), the profiling current meter was operated over the CF section on two occasions (September 8 and September 11) separated by three days; on the second pass the westward PCM transport between CF 2 and CF 13 was one fourth that of the first pass. Changes of this magnitude are unlikely to occur simply as a result of local relaxation of internal density surfaces.

4.3 Profiling current meter *vs.* time-averaged velocity

In this section the September 8, 1983 PCM profile is compared to the September 11, 1983 PCM profile based upon their resemblences to the mean current meter velocities. The purpose of this comparison will become evident in Chapter 5, when the PCM velocities are integrated across the shelf and vertically to provide estimates of the transport streamfunction. Basically, the question is which of the two September, 1983 PCM transects is more representative of the mean condition. The comparisons are of the PCM velocities at the depth of the current meters, to the velocities measured by the moored current meters. To estimate the spatial variability, data from two PCM profiles are used: one from CF3, the station nearest to the mooring, and one from CF4, 3.7 km south of CF3. The current meter data was averaged over a 29 day interval centered at the time of the PCM sections. This will be referred to as the 29d data.

The magnitude of the PCM velocity was greater than those of the current meter on twelve of sixteen occasions. The exceptions were 1) at the surface at CF 3, 2) at 75 m at CF 3, 3) at 115 m at CF3, and at 115 m at CF4 (Figs. 4.3b and 4.3d). The greatest discrepancy was observed at CF 4, particularly on the first pass. This is not

surprising since the core of the current is "outside" the mooring at this time (Johnson *et al.*, 1988). Nevertheless, the 29d averages are in qualitative agreement with the sense of the change of the PCM velocity both at CF 3 and CF 4. This implies that the seasonal cycle in the moored current meter data is representative of the ACC as a whole.

An interesting feature is that the PCM velocity at 115 m on the second pass (Fig. 4.3b) is slightly eastward, in agreement with the 29d data. This close comparison, combined with the fact that the PCM velocities on the second pass are generally closer to the current meter velocities than those of the first pass, lends strength to the argument that the second PCM transect is more representative of the longer term mean circulation. The cause of the high velocities on the first pass is not clear, but two possibilities can be ruled out. Local winds during and prior to this period were too weak (Section 4.1), and maximum tidal velocities were too small to account for the difference (Section 4.6).

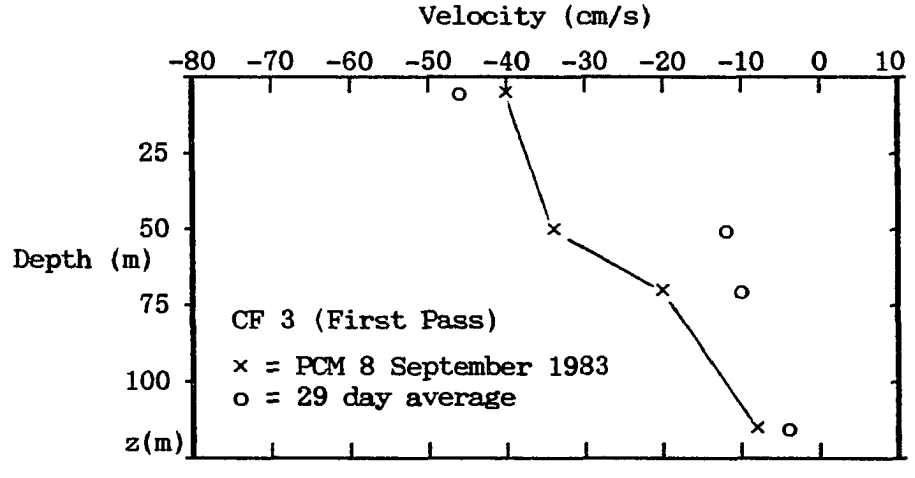

Fig. 4.3a. Comparison of PCM and current meter data at CF3.

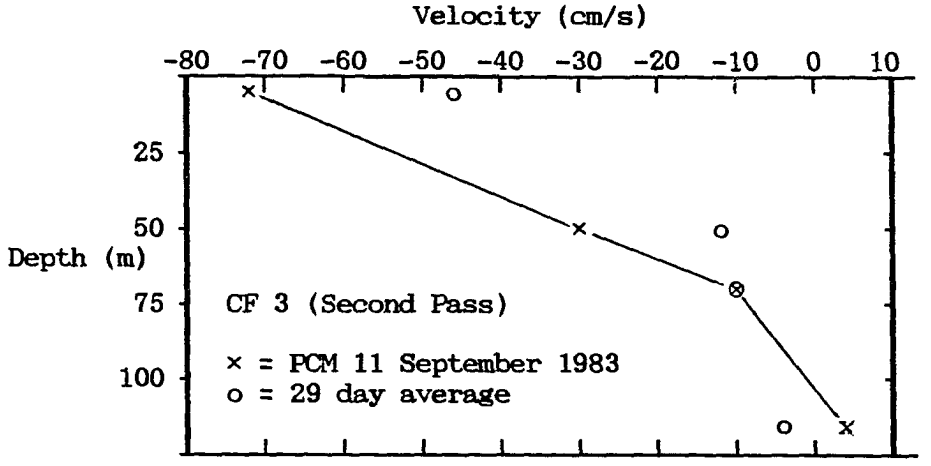

Fig. 4.3b. Comparison of PCM and current meter data at CF3.

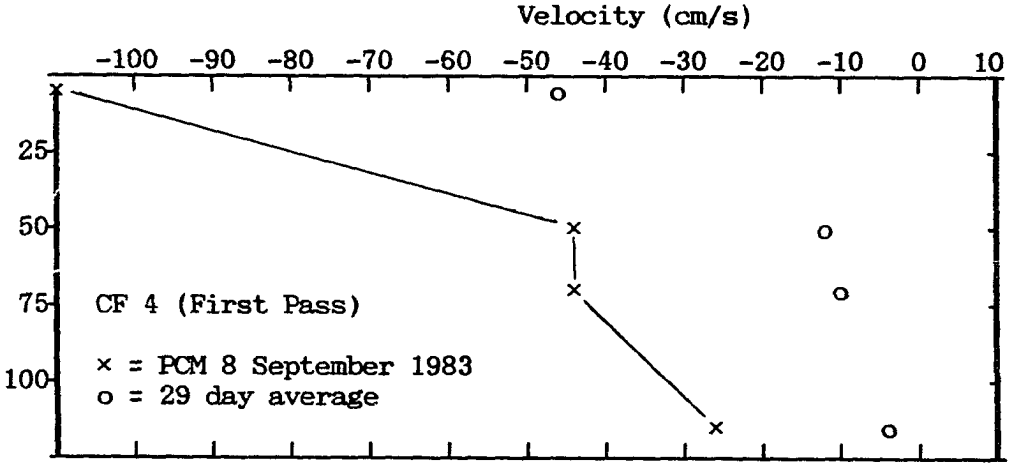

Fig. 4.3c. Comparison of PCM and current meter data at CF4.

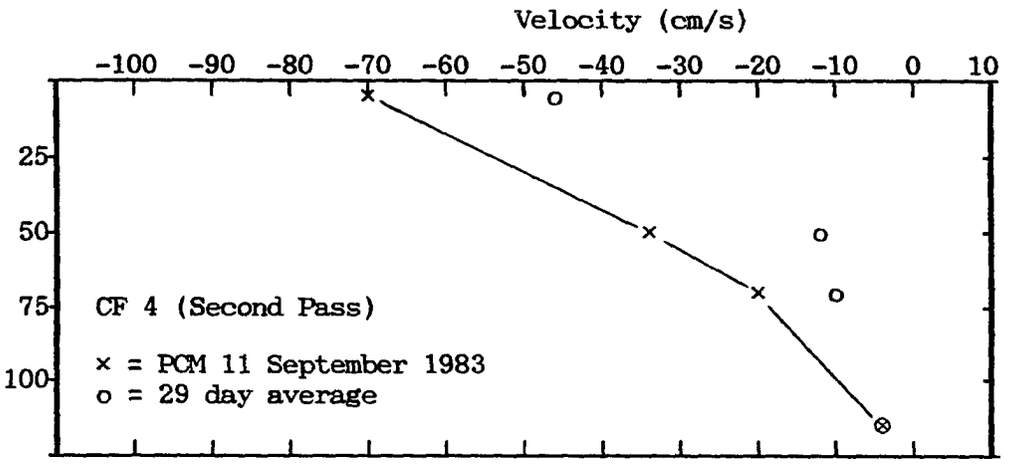

Fig. 4.3d. Comparison of PCM and current meter data at CF4.

4.4 The 3.7 day to 15 day variability

Some velocity variability at the mooring can be explained by a shift in the position of the core of the current. The two PCM sections from September, 1983, separated by three days, exhibit both a redistribution of velocity and a large reduction in integrated transport. No hydrographic data were available for the second section, so any changes in the density distribution are unknown. However, the current meter velocities are available to evaluate the subtidal variability.

In Fig. 4.4, eastward (90 T) and northward (0 T) components are presented along with the "stick plots". In order to focus on subtidal variations, the data were 35-hour lowpass filtered. Note that the velocity scale changes with depth.

The highest speed (mean = 46.4 cm/s) is that of the 2 m current meter (Fig. 4.4a). The wind, which was light and variable over most of the interval, is unlikely to be the cause of this. More probably, it is associated with the distribution of mass (i.e., buoyancy driven), as suggested by the dynamic height distribution (Section 3.5). The standard deviation of the speed (σ = 28.5 cm/s) is also highest at the surface. However, the stick plots for the 2 m data show that the flow was uniformly westward, varying by less than 45° to the north or south

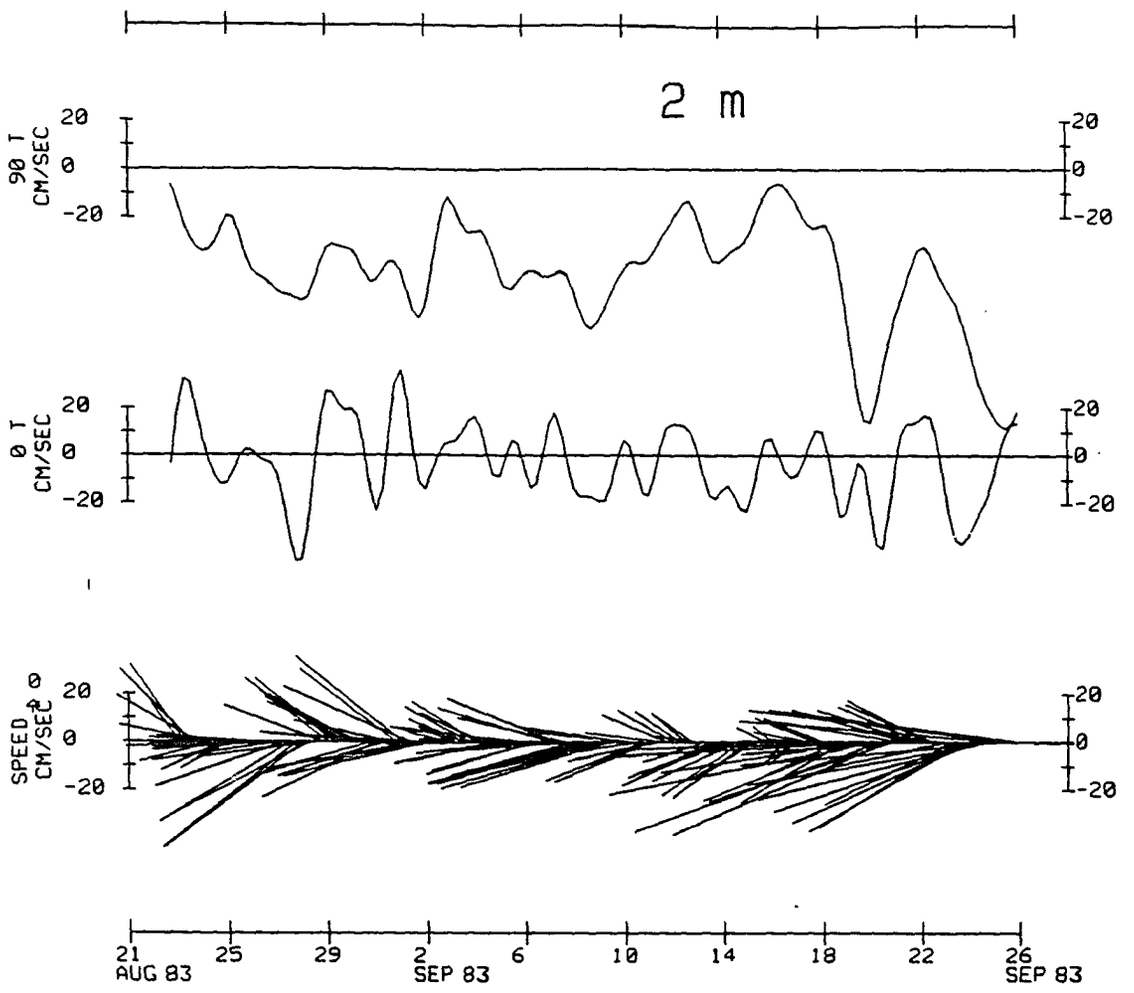

Fig. 4.4a. 2 m

Fig. 4.4. Time series of velocity at mooring. Data lowpass filtered with 35 hr half-power point. Nominal depths a) 2 m; b) 50 m; c) 70 m; d) 110 m; e) 175 m.

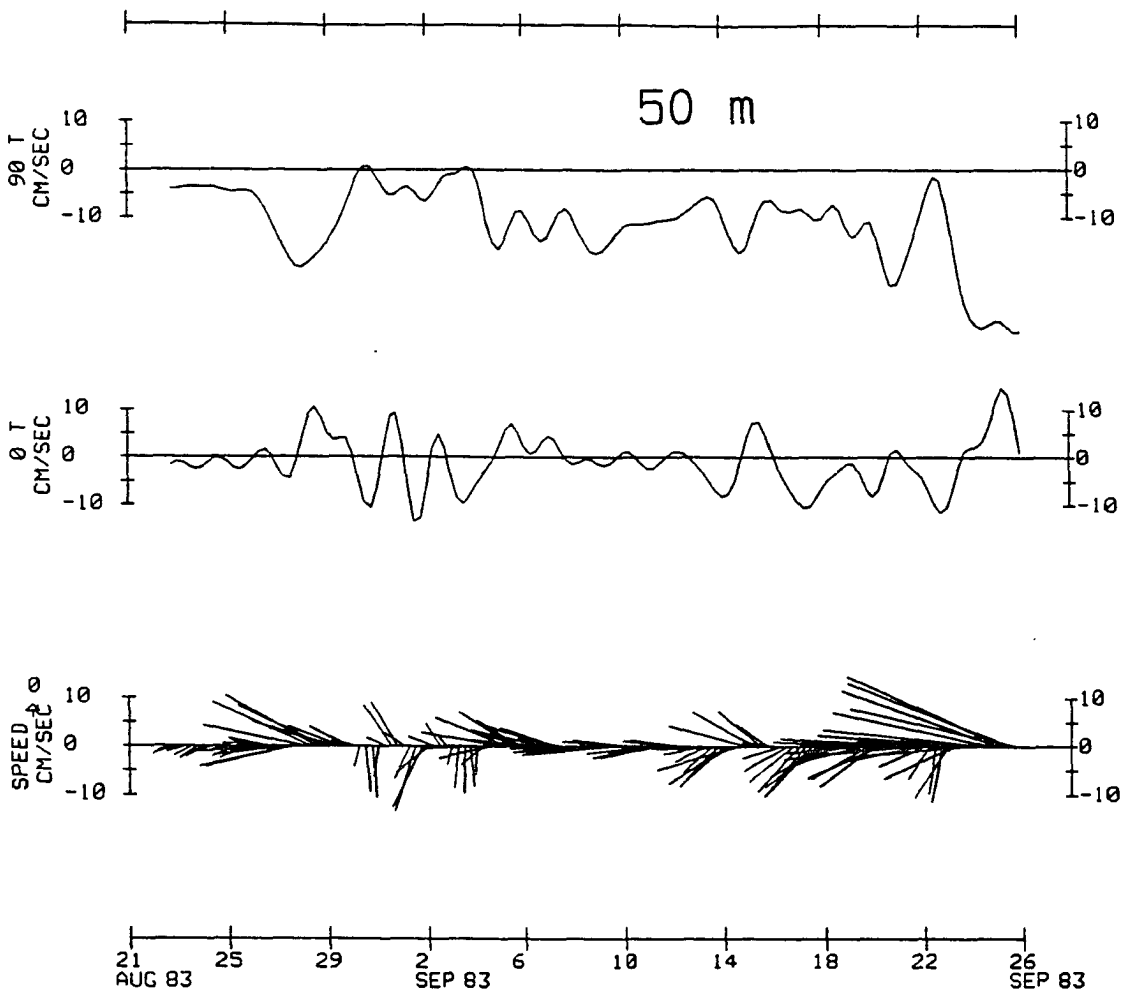

Fig. 4.4b. 50 m

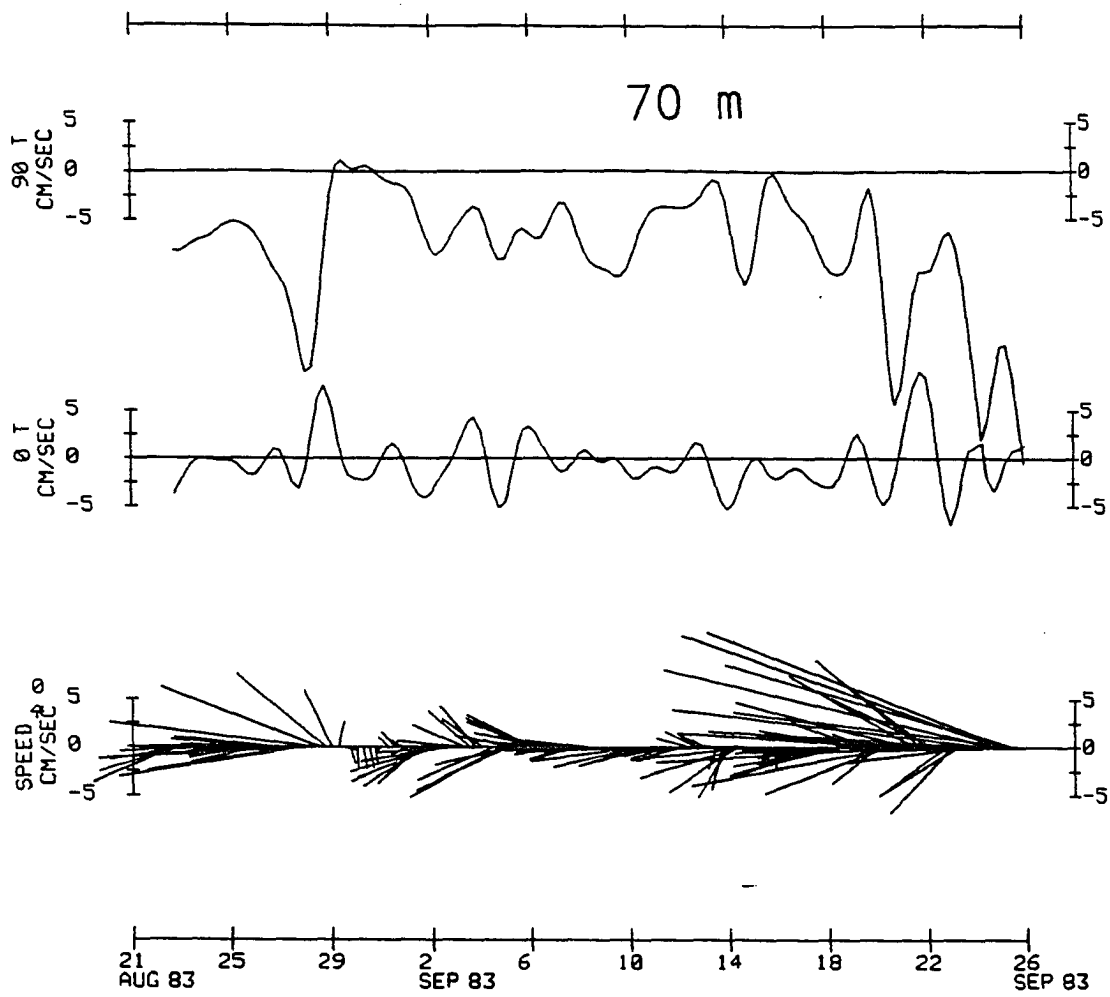

Fig. 4.4c. 70 m

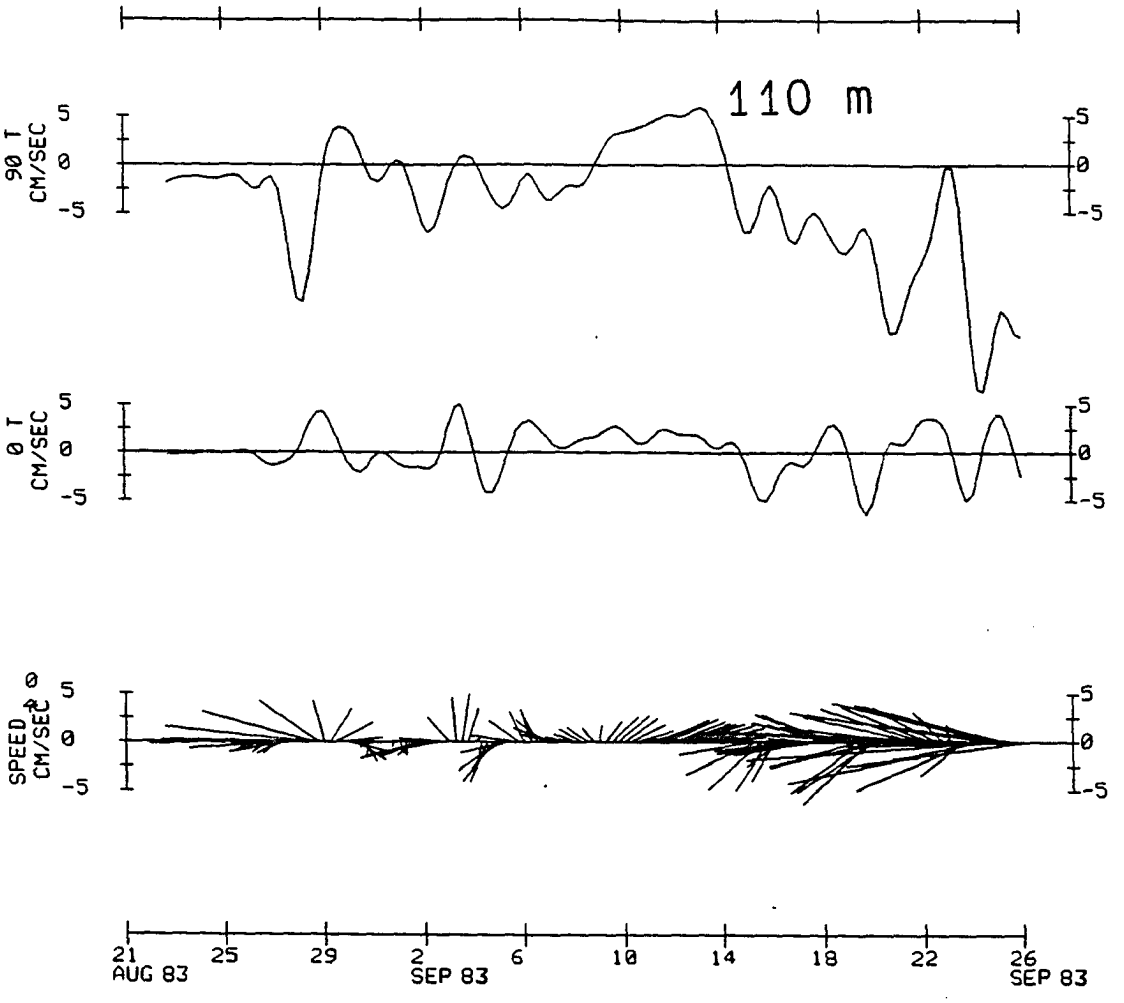

Fig. 4.4d. 110 m

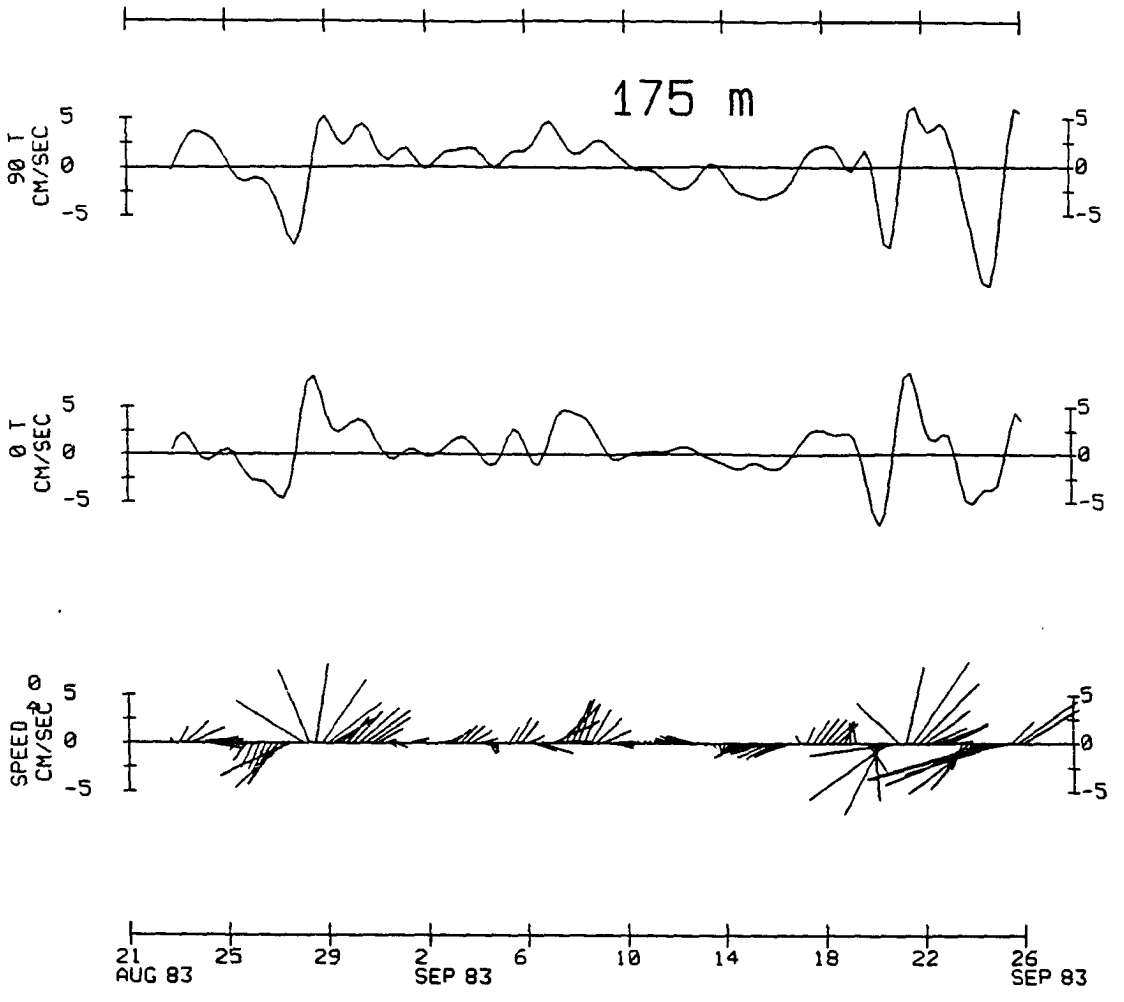

Fig. 4.4e. 175 m

of east.

The east-west components at 50 m and 70 m appear relatively steady over the period 6 September - 20 September (Fig. 4.4b,c), although the flow fluctuates in the north-south direction, according to the stick plots. This suggests that the slopes of the main isopycnal surfaces responsible for the flow remained constant. The internal mass distribution can completely compensate for the surface pressure gradient at some point below 100 m. At 110 m the slope of the isopycnals is less than the density surfaces above or below it. It is at 115 m where the current undergoes a reversal for several days (Fig. 4.4d), while at 175 m, the current was reversed over much of the period (Fig. 4.4e). The stick plots for the two deep current meters do not show a consistent pattern.

The power spectrum of velocity at the 50 m moored current meter during fall, 1983, is a maximum at the six day period (Table 4.2). This is illustrated in a table, rather than a plot, in order to make clear the distribution of periods involved.

Table 4.2. Variance in $(cm/sec)^2/cpd$ contained in frequency bands centered at the indicated periods. Data from 50 m current meter, 200 days starting 11 September 1983. The 95% confidence interval range is +.49, -.31.

Period, days	Variance
15.35	.86
11.08	.92
8.67	1.03
7.13	1.64
6.05	2.29
5.25	1.07
4.64	1.19
4.16	1.38
3.76	1.16

The peak at six days is not associated with lunisolar tides, as there are none with that period, although Greisman (1985) did detect significant energy at the fortnightly (MSF) period (see following section). The source of this variability is unclear, but a probable cause is wind forcing, which also has significant energy at the six day band (Luick *et al.*, 1986; Thomson, 1983).

4.5 Seasonal variability

The COJET current meter moorings were deployed for nineteen months, enough time to provide a preliminary description of the seasonal variability of the ACC. The purpose of this section is to discuss some aspects of the monthly-averaged time series which were not included in Johnson *et al.* (1986).

Data were 35-hour lowpass filtered to remove the tidal signal, then averaged over the monthly intervals of the COJET project. Gaps of a few days or less at the beginning or end of the mooring lifetimes were ignored. For example, the data start at about 0300 on 2 April, 1983, and two days are lost at the beginning due to the 35-hour filter, so the April average excludes the first three days. This is unlikely to result in a misleading description of the seasonal cycle. The 95% confidence limits of the means (± 1.96 standard deviations) are shown as vertical bars through the dot representing the mean (Fig. 4.5a,b). The "+" marks denote the maximum or minimum value for the month. Fig. 4.5a contains the east-west component (positive westward), and Fig. 4.5b contains the north-south flow (positive northward).

The westward surface flow at the mooring peaked in January or February, 1984, although the range (difference between minimum and maximum for the month) peaked earlier, in September or October (Fig. 4.5a). This was demonstrated in the time series of kinetic energy spectral density at 50 m depth, which also peaked in September and October, 1983 (Johnson *et al.*, 1988). However, the mean east-west flow over all the meters changed very little between September and October, 1983, the period chosen for the model of Chapter 5. A significant strengthening of the current occurs below the surface in November. At both the 110 m and 175 m levels, the east-west flow was not significantly different from zero much of the year, except from January through April. It is this feature which has led some authors to dub this type of current a "floating" or "supernatant" jet (LeBlond *et al.*, 1986a; Pettigrew and Murray, 1986). Although the mean

Fig. 4.5. Monthly averages of a) eastward (0 T) and b) northward 90 T) velocity at mooring. Square dots are the monthly averages; vertical bars through averages are 95% confidence limits; "+" marks are maxima and minima for month.

(*see following page...*)

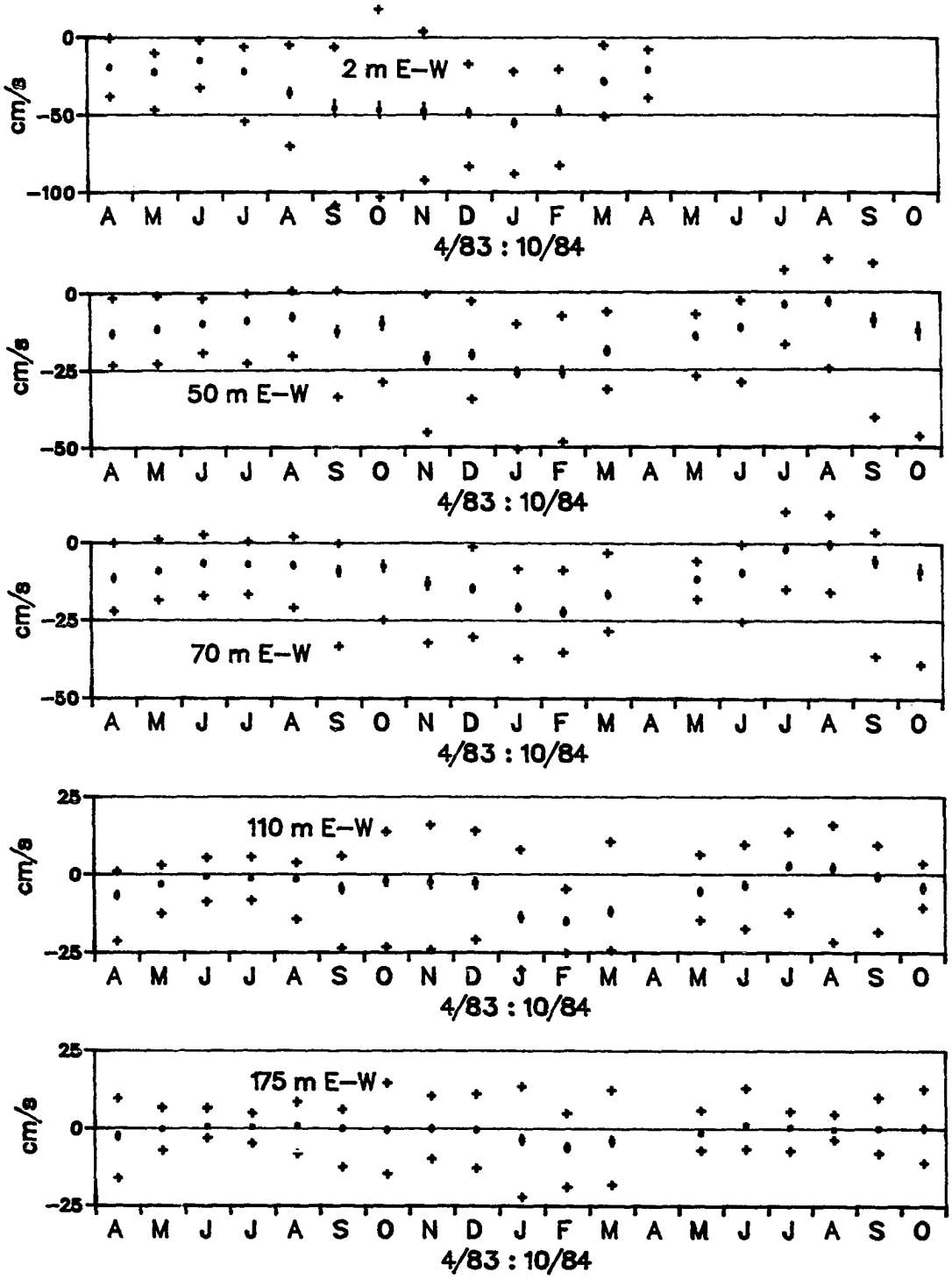

Fig. 4.5a. Eastward velocity

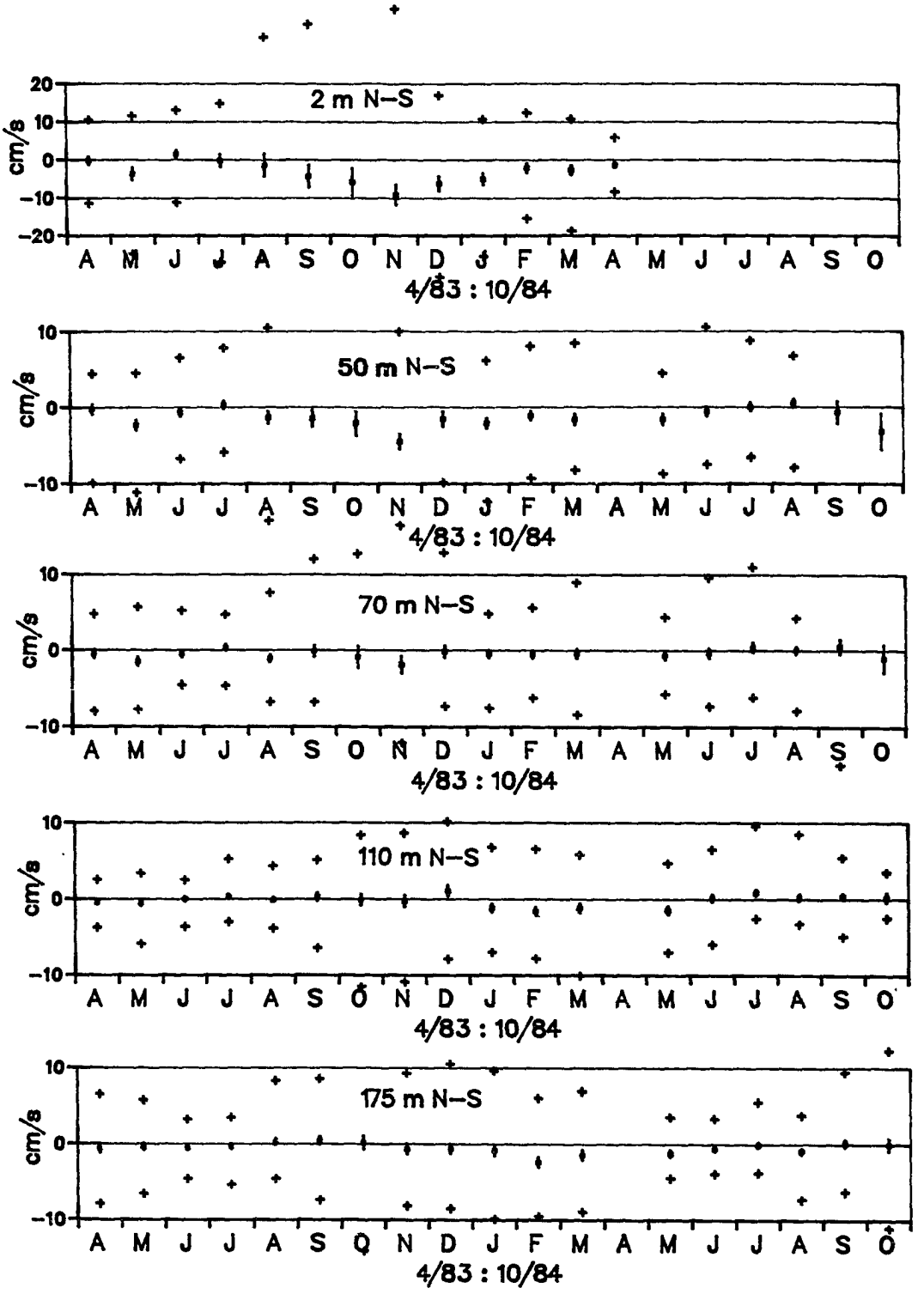

Fig. 4.5b. Northward velocity

east-west flow is small below 100 m, the range is large, with both eastward and westward bursts as high as 20 cm/s.

The mean southward flow at the 2 m, the 50 m, and the 70 m current meters peaked in November, 1983, two months earlier than the westward flow (Fig. 4.5b). This lends credence to the zero rotation of the current meter data: had the ACC been consistently deflected offshore at the mooring, the westward component, which is much larger than the southward, would have determined the timing of the peak. However, at 110 m and 175 m, the peak coincided more closely with that of the westward component. This is consistent with the concept of a leftward (southward) Ekman transport in the bottom layer of a westward flow.

Mean offshore flow at the surface (Fig. 4.5b, top panel) throughout the fall and winter is unexpected for an area dominated by downwelling-favorable winds. From the foregoing discussion, this is not a result of the southward-trending bottom topography. The large variability of the north-south component in the surface layer in October and November suggest that short term strong onshore flows, probably associated with storms moving through the area, are superimposed on the background offshore flow.

4.6 Tides and tidal mixing

The tides in Blying Sound are mixed, mainly semi-diurnal, as indicated by F, the form factor (computed using the tide gauge data), which is approximately equal to 0.5. The tidal range is relatively large, between 2 m and 4 m, depending upon the point in the fortnightly cycle. The tidal currents vary with depth and season; generally they are less than 15 cm/s at any depth and less than 5 cm/s below 50 m; however, during times of increased stratification the surface tidal currents may reach 33 cm/s and below 50 m may become as high as 10 cm/s (Table 4.3). April and September, 1983, were chosen for this comparison as they represent the unstratified and stratified cases, respectively.

Table 4.3 was formed by computing the amplitudes and phases of sixteen major tidal constituents and adding them in the form of sine waves. Thus, the entries represent the statistics of "predicted" time series of purely tidal motions.

Table 4.3. Predicted tidal currents (cm/s) and zero-mean tide gauge range (decibars) during April, 1983 and September, 1983. Statistics from 29-day harmonic analysis. The last column contains the standard deviation (SD).
*scalar pressure fluctuation

		April, 1983			September, 1983		
Depth	Component	Max	Min	SD	Max	Min	SD
2 m	u	13.06	-13.54	5.79	33.83	-26.65	11.80
2 m	v	10.10	-11.06	4.77	28.55	-31.00	11.92
50 m	u	3.65	-3.97	1.68	9.82	-9.13	3.89
50 m	v	5.23	-5.74	2.65	7.42	-7.42	3.10
70 m	u	3.05	-3.59	1.50	5.94	-5.33	2.17
70 m	v	2.23	-3.02	1.22	6.63	-7.81	3.14
110 m	u	4.47	-4.58	2.18	3.61	-4.92	1.92
110 m	v	3.01	-2.57	1.32	7.59	-7.77	3.59
175 m	u	4.23	-4.25	1.64	5.52	-5.53	2.83
175 m	v	2.68	-3.03	1.44	-6.91	6.71	2.69
185 m	*	1.96	-2.17	0.97	2.03	-2.25	0.98

The increased energy at tidal frequencies in September is shown in the size of the standard deviations of the predicted tidal currents (Table 4.3). With the exception of u at 110 m,the SD increased at each depth, by factors up to 6.3. The SD is greatest near the surface. In April the SD at 2 m was about three times that at 50 m and below; in September the effect extended down to the 50 m level.

Neither the mean nor the SD of the predicted tidal series are strongly polarized, in contrast to those of the ACC. In fact, the v components are often larger than the u components, particularly below the surface. The largest amplitude tidal velocity in Table 4.3, 33.83 cm/s for the alongshore component in September is only slightly larger than the cross-shelf component. Hence, tidal mixing is nearly isotropic. At 50 m, the amplitude of the tidal current at that time drops to below 10 cm/s.

The tide gauge extremes and SD did not change appreciably between

April and September, 1983. The changes in the tidal currents, are therefore probably associated with the internal mass distribution, that is, the scattering of energy into internal tides. Greisman (1985) analyzed data from a widely spaced array of tide gauges and current meters located near Shelikov Straits in the western Gulf of Alaska, between 150 and 400 km southwest of Blying Sound. The two areas are similar in terms of water properties (Reed *et al.*, 1986), although the proximity of Shelikov Strait and Cook Inlet greatly alter the tidal currents due to their geometry. Greisman, using vertical mode analysis, predicted the existence of large baroclinic velocities for the M2 tidal component. He also predicted large vertical excursions of the isopycnals. Because of the velocity shears involved, the internal tides affect the thermohaline structure and promote mixing to an extent beyond that of the surface tide (Hendershott, 1981). Another difficulty is that the vertical displacements can contribute errors to the hydrographic sampling. Greisman (1985) predicted 30 m displacements in 65 m of water in Cook Inlet. He suggests that in order to measure the amplitude of the displacements, it is necessary to sample the temperature and salinity using a CTD repeatedly over the tidal cycle and average the results. The proximity of Prince William Sound suggests that Greisman's results also apply to our study area, although to a lesser degree, since the salinity variations at the current meter, to which the amplitudes are directly proportional in Greisman's model, are about a tenth those of Cook Inlet.

Chapter 5. THE MOMENTUM BALANCE

5.1 Overview

The balance of forces that produces the Alaska Coastal Current was investigated by means of a numerical model. The model is diagnostic in the sense that the internal density gradients and the wind stress are prescribed from measured data. A time-independent, Boussinesq formulation is used. A central feature of the model is that, similarly to Kantha *et al* (1981), the second order equations are reduced to first order by initially ignoring the bottom stress, which is then accounted for in an iterative fashion. This eliminates the requirement for two boundary conditions. Instead, a single boundary condition is required and the solution is extended away from the boundary by integration along characteristics.

The diagnostic method was largely developed in the Soviet Union by A.S. Sarkisyan. Sarkisyan (1977) provided a comprehensive review of current progress. The basic motivation is to take advantage of the relatively steady and well sampled density field to eliminate an unknown in the momentum balance equations. In this respect it is a generalization of the classical dynamic method of computing currents, but instead of assuming a "level of no motion", the entire water column and the slope of the ocean bottom is included. The method was adapted by Galt and Watabayashi (1984) to interpret the OCSEAP data on the continental shelf in the Northeast Gulf of Alaska. The focus of those studies was shelf-width processes, and the ACC was not well resolved. Kantha *et al.* (1982) solved the linear, first order, steady state equations diagnostically over a region encompassing the Mid-Atlantic Bight. The model presented here is largely a combination of the approaches of Kantha *et al.* (1982), and Kantha *et al.* (1981).

5.2 Description of the model

The steady-state, Boussinesq, linear momentum balance equations

in a rotating spherical system of co-ordinates may be written as follows (Sarkisyan, 1977):

$$-fv\rho_0 = -\frac{1}{R\cos\phi}\frac{\partial p'}{\partial \lambda} + \rho_0 \frac{\partial}{\partial z}\left(N_z \frac{\partial u}{\partial z} \right), \tag{5.1}$$

$$fu\rho_0 = -\frac{1}{R}\frac{\partial p'}{\partial \phi} + \rho_0 \frac{\partial}{\partial z}\left(N_z \frac{\partial v}{\partial z} \right), \tag{5.2}$$

$$\frac{\partial}{\partial z}(p_0+p') = -g(\rho_0+\rho') \tag{5.3}$$

Here λ is the longitude (positive east), ϕ is the latitude, z is the local vertical (positive upwards from z = 0 at the sea surface), and R is the radius of the earth. The balance between the downward-acting gravitational force and the vertical pressure gradient is represented by Eq. 5.3. Pressure and density are expressed in terms of basic state (p_0 and ρ_0) and perturbation (p' and ρ') quantities.

Eq. 5.3 is integrated between depth z and the free surface (ζ) in order to obtain an expression for p' which can be substituted into Eqs. 5.1 and 5.2:

$$\int_{p_0(z)}^{p_0(\zeta)} dp_0 + \int_{p'(z)}^{p'(\zeta)} dp' = -\int_z^\zeta g\rho_0 \, dz - \int_z^\zeta g\rho' \, dz \, .$$

The oceanic basic state pressure can only be positive, and it will be defined to be zero at or above z=0. Therefore the upper limit on the first integral vanishes. Integrating for pressure on the left hand side, and breaking the integral of basic state density (ρ_0) into depth intervals (z,0) and (0,ζ),

$$-p_0(z) + p'(\zeta) - p'(z) = -\int_z^0 g\rho_0 \, dz - \int_0^\zeta g\rho_0 \, dz - \int_z^\zeta g\rho' \, dz \, .$$

The equation of hydrostatic balance is written $\frac{\partial}{\partial z}p_0 = -g\rho_0$. Integrating this equation over (z,0),

$$\int_{p_0(z)}^{p_0(0)} dp_0 = -\int_z^0 g\rho_0 \, dz \, , \text{ or}$$

$-p_0(z) = -\int_z^0 g\rho_0 \, dz$. As before, the upper limit on the integration

of basic state density vanishes. Using this expression, and noting that $p'(\zeta) = p_a$, the atmospheric pressure, the vertical balance becomes

$$p_a - p'(z) = - \int_0^\zeta g\rho_0 \, dz - \int_z^\zeta g\rho' \, dz \ .$$

Solving for $p'(z)$,

$$p'(z) = p_a + \int_0^\zeta g\rho_0 \, dz + \int_z^\zeta g\rho' \, dz \ .$$

On substitution into 5.1 and 5.2, p' is differentiated with respect to λ and ϕ. These derivatives take the form

$$\frac{\partial p'}{\partial \lambda} = g\rho_0(\zeta) \frac{\partial \zeta}{\partial \lambda} + \frac{\partial}{\partial \lambda} \int_z^\zeta \rho' g \, dz \ , \text{ and}$$

$$\frac{\partial p'}{\partial \phi} = g\rho_0(\zeta) \frac{\partial \zeta}{\partial \phi} + \frac{\partial}{\partial \phi} \int_z^\zeta \rho' g \, dz \ .$$

In the differentiations, the steady state assumption was applied to the surface atmospheric pressure gradients. In other words, the ocean is no longer under adjustment as an "inverse barometer". Hence $\frac{\partial p_a}{\partial \lambda} = \frac{\partial p_a}{\partial \phi} = 0$.

Substituting the expressions for $\frac{\partial p'}{\partial \lambda}$ and $\frac{\partial p'}{\partial \phi}$ into Eqs. 5.1 and 5.2,

$$- fv\rho_0 = - \frac{1}{R \cos \phi} \left[\rho_0(\zeta) g \frac{\partial \zeta}{\partial \lambda} + \frac{\partial}{\partial \lambda} \int_z^\zeta \rho' g \, dz\right] + \rho_0 \frac{\partial}{\partial z} \left(N_z \frac{\partial u}{\partial z} \right), \tag{5.4}$$

$$fu\rho_0 = - \frac{1}{R} \left[\rho_0(\zeta) g \frac{\partial \zeta}{\partial \phi} + \frac{\partial}{\partial \phi} \int_z^\zeta \rho' g \, dz\right] + \rho_0 \frac{\partial}{\partial z} \left(N_z \frac{\partial v}{\partial z} \right). \tag{5.5}$$

These are essentially the Ekman equations. The current is caused by pressure gradients due to sealevel and density stratification and by wind stress which enters as a boundary condition into the last term, representing the vertical exchange of horizontal momentum. Before attempting to solve for velocity, an additional equation for the unknown sealevel gradients must be introduced. The solution will proceed as follows. The Ekman equations are first integrated vertically over the entire depth. Wind stress is introduced as an

upper boundary condition. The sealevel gradient terms ($\frac{\partial\zeta}{\partial\lambda}$ and $\frac{\partial\zeta}{\partial\phi}$) are then eliminated by cross-differentiation, resulting in a single expression with two unknowns (the horizontal components of the gradient of mean velocity). These unknowns are expressed in terms of a streamfunction, the solution for which will finally be related back to sealevel gradient, which in turn is used to solve the Ekman equations.

Integrating upwards from the bottom, $z = -H(x,y)$, to $z = \zeta$,

$$-f\rho_0\int_{-H}^{\zeta} v\,dz = -\frac{1}{R\cos\phi}\left[\rho_0(\zeta)g\int_{-H}^{\zeta}(\frac{\partial\zeta}{\partial\lambda})dz + \int_{-H}^{\zeta}(\frac{\partial}{\partial\lambda}\int_{z}^{\zeta}\rho' g\,dz)dz\right]$$

$$+ \rho_0\int_{-H}^{\zeta}(\frac{\partial}{\partial z}N_z\frac{\partial u}{\partial z})\,dz, \text{ and} \qquad (5.6)$$

$$f\rho_0\int_{-H}^{\zeta} u\,dz = -\frac{1}{R}\left[\rho_0(\zeta)g\int_{-H}^{\zeta}(\frac{\partial\zeta}{\partial\phi})dz + \int_{-H}^{\zeta}(\frac{\partial}{\partial\phi}\int_{z}^{\zeta}\rho' g\,dz)dz\right]$$

$$+ \rho_0\int_{-H}^{\zeta}(\frac{\partial}{\partial z}N_z\frac{\partial v}{\partial z})\,dz. \qquad (5.7)$$

Defining $\bar{u} = \frac{1}{(H+\zeta)}\int_{-H}^{\zeta} u\,dz$, $\bar{v} = \frac{1}{(H+\zeta)}\int_{-H}^{\zeta} v\,dz$,

$$\tau_\lambda = \rho_0 N_z\frac{\partial u}{\partial z}, \text{ and } \tau_\phi = \rho_0 N_z\frac{\partial v}{\partial z},$$

and using $\int_{-H}^{\zeta}\frac{\partial\vec{\tau}}{\partial z}dz = \vec{\tau}^w - \vec{\tau}^b$, where $\vec{\tau}^w$ and $\vec{\tau}^b$ are the wind and bottom stress vectors, eqs. 5.6 and 5.7 become

$$-\rho_0 f H\bar{v} = -\rho_0\frac{gH}{R\cos\phi}\frac{\partial\zeta}{\partial\lambda} - \frac{g}{R\cos\phi}\int_{-H}^{0}\frac{\partial}{\partial\lambda}\int_{z}^{0}(\rho' dz)dz + \tau_\lambda^w - \tau_\lambda^b,$$

and (5.8)

$$\rho_0 f H\bar{u} = -\rho_0\frac{gH}{R}\frac{\partial\zeta}{\partial\phi} - \frac{g}{R}\int_{-H}^{0}\frac{\partial}{\partial\phi}\int_{z}^{0}(\rho' dz)dz + \tau_\phi^w - \tau_\phi^b, \qquad (5.9)$$

with $H + \zeta \cong H$, and $\rho_0 = \frac{1}{H}\int_{-H}^{\zeta} \rho \, dz$. Also, ζ in the upper limits of the double integrations has been replaced by 0, since $\zeta << H$. The presence of the vertical coordinate z in the lower limit of integration in the second term on the right hand sides of Eqs. 5.8 and 5.9 presents a computational problem in the presence of a sloping bottom (Kantha *et al.*, 1982). This term can be converted to a more tractable form by use of an integral identity. This procedure was also employed in Sarkisyan (1977) and in Galt and Watabayashi (1984). The procedure will be demonstrated for Eq. 5.8 only; 5.9 follows in an analogous manner.

First the integral is broken up into two parts, and z is replaced by q as a dummy variable on the inner integral:

$$\int_{-H}^{0} \frac{\partial}{\partial\lambda}\int_{z}^{0} \rho' \, dq \, dz = \int_{-H}^{0} \frac{\partial}{\partial\lambda}\left[\int_{-H}^{0} \rho' \, dq - \int_{-H}^{z} \rho' \, dq\right] dz. \qquad (5.10)$$

Distributing the integration sign, and noting that the integration of the definite integral in the first term of 5.10 yields only H,

$$\int_{-H}^{0} \frac{\partial}{\partial\lambda}\int_{z}^{0} \rho' \, dq \, dz = H \frac{\partial}{\partial\lambda}\int_{-H}^{0} \rho' \, dz - \int_{-H}^{0} \frac{\partial}{\partial\lambda}\int_{-H}^{z} \rho' \, dq \, dz \, ,$$

or

$$\int_{-H}^{0} \frac{\partial}{\partial\lambda}\int_{z}^{0} \rho' \, dq \, dz = H \frac{\partial}{\partial\lambda} \int_{-H}^{0} \rho' \, dz - \frac{\partial}{\partial\lambda}\int_{-H}^{0} \int_{-H}^{z} \rho' \, dq \, dz \qquad (5.11)$$

The derivative was taken out of the integrand of the second term on the right hand side without having to add a term at either limit. Obviously, at the upper limit, $\frac{\partial(0)}{\partial\lambda} = 0$. At the lower limit, $\frac{\partial(-H)}{\partial\lambda}$ is multiplied by the integrand evaluated at $z = -H$, which is also zero.

The double integral on the RHS of Eq. 5.11 can now be transformed to a single integral with z in the integrand. That is, for a general function f(q), it can be shown

$$\int_{-H}^{0} \int_{-H}^{z} f(q) \, dq \, dz = - \int_{-H}^{0} z \, f(z) \, dz \, . \qquad (5.12)$$

The proof of this requires a single integration by parts. The left hand side is of the form $\int_a^b u\,dv$, with $u = \int_{-H}^{z} f(q)\,dx$, and $dv = dz$. Then, with $du = (du/dz)dz = f(z)dz$, and $v = z$, the form of the solution is $uv\big|_a^b - \int_a^b v\,du$, or $\left(\int_{-H}^{z} f(z)dz \cdot z\right)\Big|_{-H}^{0} - \int_{-H}^{0} z\,f(z)\,dz$. Since the first term of the solution is zero at both limits, 5.12 is an identity. Using this result, Eqs. 5.8 and 5.9 become

$$-\bar{f}\bar{v}H = \frac{-gH}{R\cos\phi}\frac{\partial\zeta}{\partial\lambda} - \frac{gH}{\rho_0 R\cos\phi}\frac{\partial}{\partial\lambda}\int_{-H}^{0}\rho'\,dz - \frac{g}{\rho_0 R\cos\phi}\frac{\partial}{\partial\lambda}\int_{-H}^{0} z\,\rho'\,dz$$

$$+\frac{1}{\rho_0}\left(\tau_\lambda^w - \tau_\lambda^b\right), \text{ and} \qquad (5.13)$$

$$\bar{f}\bar{u}H = \frac{-gH}{R}\frac{\partial\zeta}{\partial\phi} - \frac{gH}{\rho_0 R}\frac{\partial}{\partial\phi}\int_{-H}^{0}\rho'\,dz - \frac{g}{\rho_0 R}\frac{\partial}{\partial\phi}\int_{-H}^{0} z\,\rho'\,dz$$

$$+\frac{1}{\rho_0}\left(\tau_\phi^w - \tau_\phi^b\right). \qquad (5.14)$$

Following Kantha *et al.* (1982) these terms are defined:

$$\Pi = g\zeta + \frac{g}{\rho_0}\int_{-H}^{0}\rho'\,dz, \text{ and } \Phi = \frac{g}{\rho_0}\int_{-H}^{0} z\,\rho'\,dz.$$

With these definitions, Eqs. 5.13 and 5.14 become

$$\bar{f}\bar{v}\cos\phi = \frac{1}{R}\frac{\partial\Pi}{\partial\lambda} + \frac{1}{RH}\frac{\partial\Phi}{\partial\lambda} - \frac{\cos\phi}{\rho_0 H}\left(\tau_\lambda^w - \tau_\lambda^b\right), \text{ and}$$

$$\bar{f}\bar{u} = \frac{-1}{R}\frac{\partial\Pi}{\partial\phi} - \frac{1}{RH}\frac{\partial\Phi}{\partial\phi} + \frac{1}{\rho_0 H}\left(\tau_\phi^w - \tau_\phi^b\right).$$

Cross-differentiating with respect to λ and ϕ,

$$f\frac{\partial}{\partial\phi}\left(\bar{v}\cos\phi\right) + \bar{v}\cos\phi\frac{\partial f}{\partial\phi} = \frac{1}{R}\frac{\partial^2\Pi}{\partial\phi\partial\lambda} + \frac{1}{RH}\frac{\partial^2\Phi}{\partial\phi\partial\lambda} + \frac{1}{R}\frac{\partial\Phi}{\partial\lambda}\frac{\partial}{\partial\phi}\left(\frac{1}{H}\right)$$

$$-\frac{\partial}{\partial\phi}\left[\frac{\cos\phi}{\rho_0 H}\left(\tau_\lambda^w - \tau_\lambda^b\right)\right], \text{ and}$$

$$f\frac{\partial\bar{u}}{\partial\lambda} = \frac{-1}{R}\frac{\partial^2\Pi}{\partial\lambda\partial\phi} - \frac{\partial^2\Phi}{\partial\lambda\partial\phi} - \frac{1}{R}\frac{\partial\Phi}{\partial\phi}\frac{\partial}{\partial\lambda}(\frac{1}{H}) + \frac{\partial}{\partial\lambda}\left[\frac{1}{\rho_0 H}(\tau_\phi^w - \tau_\phi^b)\right] .$$

Adding these two expressions,

$$f\frac{\partial}{\partial\phi}(\bar{v}\cos\phi) + \bar{v}\cos\phi\frac{\partial f}{\partial\phi} + f\frac{\partial\bar{u}}{\partial\lambda} = \frac{1}{R}\left[\frac{\partial\Phi}{\partial\lambda}\frac{\partial}{\partial\phi}(\frac{1}{H}) - \frac{\partial\Phi}{\partial\phi}\frac{\partial}{\partial\lambda}(\frac{1}{H})\right]$$

$$- \frac{\partial}{\partial\phi}\left[\frac{\cos\phi}{\rho_o H}(\tau_\lambda^w - \tau_\lambda^b)\right] + \frac{\partial}{\partial\lambda}\left[\frac{1}{\rho_0 H}(\tau_\phi^w - \tau_\lambda^b)\right] .$$

We now define

$$D_1 = \left[\frac{\partial\Phi}{\partial\lambda}\frac{\partial}{\partial\phi}(\frac{1}{H}) - \frac{\partial\Phi}{\partial\phi}\frac{\partial}{\partial\lambda}(\frac{1}{H})\right] , \text{ and}$$

$$T = \frac{\partial}{\partial\phi}\left[\frac{-\cos\phi}{\rho_o H}(\tau_\lambda^w - \tau_\lambda^b)\right] + \frac{\partial}{\partial\lambda}\left[\frac{1}{\rho_0 H}(\tau_\phi^w - \tau_\phi^b)\right] .$$

Again writing the wind and bottom stress vectors as $\vec{\tau}^w$ and $\vec{\tau}^b$, T can be put in more familiar terms,

$$T = \frac{\sin\phi}{\rho_0 H}(\tau_\lambda^w - \tau_\lambda^b) + \frac{R\cos\phi}{\rho_0 H}(\text{curl}\,\vec{\tau}^w - \text{curl}\,\vec{\tau}^b) -$$

$$\frac{R\cos\phi}{\rho_0}\nabla\frac{1}{H}\times(\vec{\tau}^w - \vec{\tau}^b).$$

Remembering that $\nabla\frac{1}{H} = \frac{1}{R}(\cos\phi\frac{\partial}{\partial\lambda}(\frac{1}{H}) + \frac{\partial}{\partial\phi}(\frac{1}{H}))$, it is seen that the first term and the term involving $\nabla\frac{1}{H}$ are of order R smaller than the others, so that

$$T \cong \frac{R\cos\phi}{\rho_0 H}(\text{curl}\,\vec{\tau}^w - \text{curl}\,\vec{\tau}^b)$$

With these definitions,

$$f\frac{\partial\bar{u}}{\partial\lambda} + f\frac{\partial}{\partial\phi}(\bar{v}\cos\phi) + \bar{v}\cos\phi\frac{\partial f}{\partial\phi} = \frac{1}{R}D_1 + T . \qquad (5.15)$$

The left hand side of Eq. 5.15 can be simplified by use of the integrated equation of continuity,

$$\frac{\partial}{\partial\lambda}(\bar{u}H) + \frac{\partial}{\partial\phi}(\bar{v}H\cos\phi) = 0 ,$$

so that

$$H\bar{u}\,\frac{\partial}{\partial\lambda}\left(\frac{f}{H}\right) + H\bar{v}\cos\phi\,\frac{\partial}{\partial\phi}\left(\frac{f}{H}\right) = \frac{1}{R}D_1 + T \quad . \tag{5.16}$$

In a flat-bottomed ocean or one with zero baroclinicity ($D_1 = 0$) and no bottom stress torques, Eq. 5.16 reduces to the Sverdrup balance between northward transport and wind stress curl. The term $\frac{f}{H}$ is sometimes called "planetary potential vorticity", in that it represents the planetary part of $\frac{\eta+f}{H}$, the potential vorticity. In this context, η, the relative vorticity, must be defined as the curl of the *depth-averaged* velocities. Had either the time dependence or the nonlinear terms been included in the equations of motion (Eqs. 5.1, 5.2), η would have been included on the left side of Eq. 5.16. The left hand side can be written $H(\vec{\bar{u}}\cdot\nabla(\frac{f}{H}))$, which can be thought of as the advection of $\frac{f}{H}$, or, after dividing by cos ϕ, as the component of transport ($\vec{H\bar{u}}$) across contours of $\frac{f}{H}$. In a region where the "production" (D_1 and T) terms are zero, transport is constrained to follow contours of $\frac{f}{H}$. If local changes in H dominate those in f, then a nonzero sum of the production terms requires flow across depth contours, consequently changing the height of the water column.

The term D_1 in Eq. 5.16 is a joint interaction term. Mathematically, D_1 is proportional to the cross product of the gradients of Φ (the potential energy), and $\frac{1}{H}$. Therefore D_1 is proportional to the sine of the angle between the two gradients. In general the gradient of Φ is aligned parallel to the isopycnal slope. For example, if along a given shoreline the isopycnals and bottom depth both slope only in the offshore direction, D_1 is zero. Any misalignment, however, implies a mean flow across contours of $\frac{f}{H}$.

Surface and bottom stress torques, T, can also deflect the flow. The wind stress curl is an external forcing term. The bottom stress, on the contrary, is a function of the velocity profile within a few tens of meters of the bottom. This adds complexity to the problem. The inclusion of bottom stress in the solution for average velocities is discussed later.

The model equation can now be expressed in terms of a single variable, Ψ, defined by

$$\bar{v}HR\cos\phi = \frac{\partial\Psi}{\partial\lambda} \text{ , and } -\bar{u}HR = \frac{\partial\Psi}{\partial\phi} .$$

Ψ, a mass transport streamfunction, is guaranteed to exist by the integrated equation of continuity. Defining also $\alpha = \frac{f}{H}$, and multiplying by R, the model equation becomes

$$\frac{\partial\Psi}{\partial\phi}\frac{\partial\alpha}{\partial\lambda} - \frac{\partial\Psi}{\partial\lambda}\frac{\partial\alpha}{\partial\phi} = -(D_1 + RT) . \qquad (5.17)$$

Solving for Ψ resulted in a field which was very sensitive to the choice of depth gradients and contour paths. An improvement suggested by Kantha *et al.* (1982) tends to smooth the result by shifting the emphasis from the bottom topography to the field of Φ (potential energy), which tends to be smoother, in analogy to the dynamic topography. Their suggestion was adopted in this model. A function X is defined which has the units of streamfunction, but which differs from $\Psi(\lambda,\phi)$ by the term $\frac{\Phi}{f}$, i.e., $X = \Psi - \frac{\Phi}{f}$. With this definition,

$$\frac{\partial\Psi}{\partial\phi} = \frac{\partial X}{\partial\phi} + \frac{\partial}{\partial\phi}(\frac{\Phi}{f}) \text{ , and } \frac{\partial\Psi}{\partial\lambda} = \frac{\partial X}{\partial\lambda} + \frac{\partial}{\partial\lambda}(\frac{\Phi}{f}) .$$

Substituting these into 5.17,

$$(\frac{\partial X}{\partial\phi} + \frac{\partial}{\partial\phi}(\frac{\Phi}{f}))\frac{\partial\alpha}{\partial\lambda} - (\frac{\partial X}{\partial\lambda} + \frac{\partial}{\partial\lambda}(\frac{\Phi}{f}))\frac{\partial\alpha}{\partial\phi} = -(D_1 + RT_s) \text{ , or}$$

$$\frac{\partial X}{\partial\phi}\frac{\partial\alpha}{\partial\lambda} - \frac{\partial X}{\partial\lambda}\frac{\partial\alpha}{\partial\phi} + \frac{\partial}{\partial\phi}(\frac{\Phi}{f})\frac{\partial\alpha}{\partial\lambda} - \frac{\partial}{\partial\lambda}(\frac{\Phi}{f})\frac{\partial\alpha}{\partial\phi} = -(D_1 + RT_s) .$$

Moving the third and fourth term to the right hand side and writing D_1 in full,

$$\frac{\partial X}{\partial\phi}\frac{\partial\alpha}{\partial\lambda} - \frac{\partial X}{\partial\lambda}\frac{\partial\alpha}{\partial\phi} =$$

$$-\frac{\partial}{\partial\phi}(\frac{\Phi}{f})\frac{\partial\alpha}{\partial\lambda} + \frac{\partial}{\partial\lambda}(\frac{\Phi}{f})\frac{\partial\alpha}{\partial\phi} - \frac{\partial\Phi}{\partial\lambda}\frac{\partial}{\partial\phi}(\frac{1}{H}) + \frac{\partial\Phi}{\partial\phi}\frac{\partial}{\partial\lambda}(\frac{1}{H}) - RT_s .$$

This simplifies to

$$\frac{\partial X}{\partial \phi}\frac{\partial \alpha}{\partial \lambda} - \frac{\partial X}{\partial \lambda}\frac{\partial \alpha}{\partial \phi} = -\Phi \frac{\partial}{\partial \phi}\left(\frac{1}{f}\right) f \frac{\partial}{\partial \lambda}\left(\frac{1}{H}\right) + \frac{1}{f}\frac{\partial \Phi}{\partial \lambda}\frac{1}{H}\frac{\partial f}{\partial \phi} - RT_s \ .$$

Using $\frac{\partial}{\partial \phi}\left(\frac{1}{f}\right) = -\frac{1}{f^2}\frac{\partial f}{\partial \phi}$,

$$\frac{\partial X}{\partial \phi}\frac{\partial \alpha}{\partial \lambda} - \frac{\partial X}{\partial \lambda}\frac{\partial \alpha}{\partial \phi} = \Phi \frac{1}{f^2}\frac{\partial f}{\partial \phi} f \frac{\partial}{\partial \lambda}\left(\frac{1}{H}\right) + \frac{1}{f}\frac{\partial \Phi}{\partial \lambda}\frac{1}{H}\frac{\partial f}{\partial \phi} - RT_s \ , \text{ or}$$

$$\frac{\partial X}{\partial \phi}\frac{\partial \alpha}{\partial \lambda} - \frac{\partial X}{\partial \lambda}\frac{\partial \alpha}{\partial \phi} = \frac{1}{f}\frac{\partial f}{\partial \phi}\left(\phi \frac{\partial}{\partial \lambda}\left(\frac{1}{H}\right) + \frac{1}{H}\frac{\partial \Phi}{\partial \lambda}\right) - RT_s \ .$$

Using the product rule for differentiation,

$$\frac{\partial X}{\partial \phi}\frac{\partial \alpha}{\partial \lambda} - \frac{\partial X}{\partial \lambda}\frac{\partial \alpha}{\partial \phi} = -\left(D_2 + RT_s\right) \ , \qquad (5.18)$$

where $D_2 = -\frac{\partial}{\partial \lambda}\left(\frac{\Phi}{H}\right)\frac{1}{f}\frac{\partial f}{\partial \phi}$.

This is the defining equation for X. A further simplification is made possible by temporarily rotating the co-ordinates into a local rectangular system aligned with the contour of α. These contours are the mathematical "characteristics" of the differential equation; hence, the rotation reduces the number of degrees of freedom by one.

Fig. 5.1 illustrates the rotation. Angle β is the counter-clockwise angle between λ and the tangent to the contour α = constant at some point (λ,ϕ). The tangent line and its orthogonal form a local coordinate system $(\hat{s},\hat{n})$.

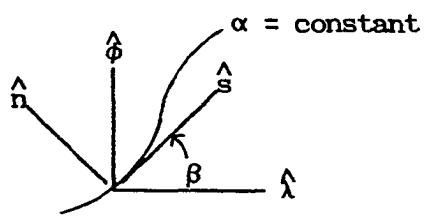

Fig. 5.1. Rotation into local $(\hat{s},\hat{n})$ frame.

In the rotated frame, the differentials ds and dn are expressed in terms of the unrotated differentials $d\lambda$ and $d\phi$ as

$$ds = R \cos\phi \cos\beta \, d\lambda + R \sin\beta \, d\phi$$

$$dn = - R \cos\phi \sin\beta \, d\lambda + R \cos\beta \, d\phi. \qquad (5.19)$$

These equations are derived by first transforming to the non-rotated local rectangular (x,y) frame, and noting that $dx = R \cos\phi \, d\lambda$, $dy = R \, d\phi$, and applying the rotation matrix to (dx,dy).

Using the chain rule, the partial derivatives in $(\hat{s},\hat{n})$ are written

$$\frac{\partial X}{\partial \phi} = \frac{\partial X}{\partial s}\frac{\partial s}{\partial \phi} + \frac{\partial X}{\partial n}\frac{\partial n}{\partial \phi}$$

$$\frac{\partial X}{\partial \lambda} = \frac{\partial X}{\partial s}\frac{\partial s}{\partial \lambda} + \frac{\partial X}{\partial n}\frac{\partial n}{\partial \lambda}$$

$$\frac{\partial \alpha}{\partial \phi} = \frac{\partial \alpha}{\partial s}\frac{\partial s}{\partial \phi} + \frac{\partial \alpha}{\partial n}\frac{\partial n}{\partial \phi} = \frac{\partial \alpha}{\partial n}\frac{\partial n}{\partial \phi}$$

$$\frac{\partial \alpha}{\partial \lambda} = \frac{\partial \alpha}{\partial s}\frac{\partial s}{\partial \lambda} + \frac{\partial \alpha}{\partial n}\frac{\partial n}{\partial \lambda} = \frac{\partial \alpha}{\partial n}\frac{\partial n}{\partial \lambda}$$

Comparing the identities

$ds = \frac{\partial s}{\partial \lambda} d\lambda + \frac{\partial s}{\partial \phi} d\phi$, and $dn = \frac{\partial n}{\partial \lambda} d\lambda + \frac{\partial n}{\partial \phi} d\phi$, with their counterparts in 5.19, it is seen that

$$\frac{\partial s}{\partial \phi} = R \sin\beta \ ,$$

$$\frac{\partial s}{\partial \lambda} = R \cos\beta \cos\phi \ ,$$

$$\frac{\partial n}{\partial \phi} = R \cos\beta \ , \text{ and}$$

$$\frac{\partial n}{\partial \lambda} = - R \sin\beta \cos\phi \ ,$$

so that the previous partial derivatives become

$$\frac{\partial X}{\partial \phi} = \frac{\partial X}{\partial s} R \sin\beta + \frac{\partial X}{\partial n} R \cos\beta \ ,$$

$$\frac{\partial X}{\partial \lambda} = \frac{\partial X}{\partial s} R \cos\beta \cos\phi - \frac{\partial X}{\partial n} R \sin\beta \cos\phi \ ,$$

$$\frac{\partial\alpha}{\partial\phi} = \frac{\partial\alpha}{\partial n} R \cos\beta \ , \text{ and}$$

$$\frac{\partial\alpha}{\partial\lambda} = - \frac{\partial\alpha}{\partial n} R \sin\beta \cos\phi \ .$$

These expressions are substituted into Eq. 5.18:

$$- R^2 \left(\frac{\partial X}{\partial s} \sin\beta + \frac{\partial X}{\partial n} \cos\beta\right) \frac{\partial\alpha}{\partial n} \sin\beta \cos\phi$$

$$- R^2 \left(\frac{\partial X}{\partial s} \cos\beta \cos\phi - \frac{\partial X}{\partial n} \sin\beta \cos\phi\right) \frac{\partial\alpha}{\partial n} \cos\beta = - (D_2 + RT_s),$$

or

$$\left(\frac{\partial X}{\partial s}\frac{\partial\alpha}{\partial n} \sin^2\beta \cos\phi + \frac{\partial X}{\partial n}\frac{\partial\alpha}{\partial n} \sin\beta \cos\beta \cos\phi\right)$$

$$+ \left(\frac{\partial X}{\partial s}\frac{\partial\alpha}{\partial n}\cos^2\beta \cos\phi - \frac{\partial X}{\partial n}\frac{\partial\alpha}{\partial n} \sin\beta \cos\beta \cos\phi\right) = \frac{(D_2 + RT_s)}{R^2} \ .$$

Simplifying,

$$\frac{\partial X}{\partial s}\frac{\partial\alpha}{\partial n} \cos\phi \ (\sin^2\beta + \cos^2\beta) = \frac{(D_2 + RT_s)}{R^2} \ , \text{ or}$$

$$\frac{\partial X}{\partial s}\frac{\partial\alpha}{\partial n} \cos\phi = \frac{(D_2 + RT_s)}{R^2\cos\phi} \ . \qquad (5.20)$$

Along a contour of s (i.e., α = constant), the partial derivative $\frac{\partial X}{\partial s}$ may be written $\frac{dX}{ds}$. Therefore, if X is known at any one point along a contour of s, Eq. 5.20 may be solved for dX, and integrated along s to find X(s). Before doing so, however, it is useful to transform back to the (λ,ϕ) frame in order to eliminate derivatives with respect to the "local" coordinates. Solving for X in 5.20, using Eq. 5.18 for ds, and using the chain rule for $\frac{\partial\alpha}{\partial n}$,

$$dX = \frac{(D_2 + RT_s)}{R^2\cos\phi} \frac{R \cos\phi \cos\beta \, d\lambda + R \sin\beta \, d\phi}{\frac{\partial\alpha}{\partial\phi}\frac{\partial\phi}{\partial n} + \frac{\partial\alpha}{\partial\lambda}\frac{\partial\lambda}{\partial n}} \ .$$

The inverse rotation procedes similiarly to the original rotation, and results in differentials $d\lambda$ and $d\phi$ defined in terms of ds and dn as follows:

$$d\lambda = \frac{\cos\beta}{R\cos\phi}\, ds - \frac{\sin\beta}{R\cos\phi}\, dn, \text{ and}$$

$$d\phi = \frac{\sin\beta}{R}\, ds + \frac{\cos\beta}{R}\, dn\ .$$

Remembering that

$$d\lambda = \frac{\partial\lambda}{\partial s}\, ds + \frac{\partial\lambda}{\partial n}\, dn, \text{ and } d\phi = \frac{\partial\phi}{\partial s}\, ds + \frac{\partial\phi}{\partial n}\, dn,$$

and identifying the partial derivatives in this pair of equations with the corresponding terms in the inverse rotation, then

$$\frac{\partial\lambda}{\partial s} = \frac{\cos\beta}{R\cos\phi}\ ,\ \frac{\partial\lambda}{\partial n} = -\frac{\sin\beta}{R\cos\phi}\ ,\ \frac{\partial\phi}{\partial s} = \frac{\sin\beta}{R}\ ,\ \text{and}\ \frac{\partial\phi}{\partial n} = \frac{\cos\beta}{R}\ .$$

A relationship between $\cos\beta$ and $\sin\beta$ can be found using the above equations and

$$\frac{\partial\alpha}{\partial s} = \frac{\partial\alpha}{\partial\lambda}\frac{\partial\lambda}{\partial s} + \frac{\partial\alpha}{\partial\phi}\frac{\partial\phi}{\partial s} = 0. \text{ Substituting in,}$$

$$\frac{\partial\alpha}{\partial\lambda}\frac{\cos\beta}{R\cos\phi} + \frac{\partial\alpha}{\partial\phi}\frac{\sin\beta}{R} = 0. \text{ Solving for } \sin\beta\ ,$$

$$\sin\beta = -\frac{\partial\alpha/\partial\lambda}{\partial\alpha/\partial\phi}\frac{\cos\beta}{\cos\phi}\ .$$

Thus dX becomes

$$dX = \frac{D_2 + RT_s}{R\cos\phi}\ \frac{\cos\beta\,\cos\phi\, d\lambda + \left(\dfrac{\partial\alpha/\partial\lambda}{\partial\alpha/\partial\phi}\dfrac{\cos\beta}{\cos\phi}\right) d\phi}{\dfrac{\partial\alpha}{\partial\phi}\dfrac{\cos\beta}{R} - \dfrac{\partial\alpha}{\partial\lambda}\dfrac{1}{R\cos\phi}\left(\dfrac{\partial\alpha/\partial\lambda}{\partial\alpha/\partial\phi}\dfrac{\cos\beta}{\cos\phi}\right)\dfrac{\cos\beta}{\cos\phi}}\ .$$

Simplifying,

$$dX = \frac{D_2 + RT_s}{\cos\phi}\left\{\frac{\dfrac{\partial\alpha}{\partial\lambda}\, d\phi - \cos^2\phi\,\dfrac{\partial\alpha}{\partial\phi}\, d\lambda}{\cos^2\phi\left(\dfrac{\partial\alpha}{\partial\phi}\right)^2 + \left(\dfrac{\partial\alpha}{\partial\lambda}\right)^2}\right\}\ . \qquad (5.21)$$

Eq. 5.21 is the final model equation for X. In order to solve for X over a domain it is necessary to estimate the streamfunction along a transect crossing contours of $\frac{f}{H}$ within the model domain (a single boundary condition). Integration of Eq. 5.21 then proceeds along the $\frac{f}{H}$ contours. On the initial integration the bottom stress which is a function of the as-yet-unknown near-bottom velocity, is assumed to be zero.

Once X is known along contours, Ψ is solved for using the definition $\Psi = X + \frac{\Phi}{f}$. Once the derivatives of Ψ are found, the sealevel slopes $\frac{\partial \zeta}{\partial \lambda}$ and $\frac{\partial \zeta}{\partial \phi}$ are easily computed using Eqs. 5.13 and 5.14. The sealevel slopes, windstress, and slopes of the isopycnals are used to solve the Ekman equations (5.5 and 5.6) for the profiles of u and v. Following Kantha *et al.* (1986), bottom stress is assumed to be a linear function of bottom velocity (details of the Ekman equation solution and bottom stress computation are in following sections). The solution for streamfunction is repeated using the new bottom stress vectors, and proceeds iteratively until convergence is achieved. A relative convergence criterion is used: the difference between the present value of bottom stress and the value at the previous iteration, divided by the present value, must be less than .01 at all points. A new profile of u and v is computed on each iteration.

5.3 Solution for $\vec{u}(z)$ and bottom stress

The horizontal velocity profile is determined by using the tri-diagonal or line inversion method (Ramming and Kowalik, 1980). For simplicity, equations 5.4 and 5.5 are re- written in normal rectangular co-ordinates:

$$- fv = - g \frac{\partial \zeta}{\partial x} - \frac{1}{\rho_0} \frac{\partial}{\partial x} \int_z^0 \rho' g \, dz + \frac{\partial}{\partial z} \left(N_z \frac{\partial u}{\partial z} \right),$$

$$fu = - g \frac{\partial \zeta}{\partial y} - \frac{1}{\rho_0} \frac{\partial}{\partial y} \int_z^0 \rho' g \, dz + \frac{\partial}{\partial z} \left(N_z \frac{\partial v}{\partial z} \right).$$

These two equations are re-expressed as a single equation by adding the first equation to i times the second ($i=\sqrt{(-1)}$):

$$if(u + iv) = - g \left(\frac{\partial \zeta}{\partial x} + i \frac{\partial \zeta}{\partial y}\right) - \frac{1}{\rho_0} \left(\frac{\partial \Pi}{\partial x} + i \frac{\partial \Pi}{\partial y}\right) + \frac{\partial}{\partial z} \left(N_z \frac{\partial}{\partial z} (u+iv)\right),$$

or, with $\mathbf{S} = u + iv$, and $\mathbf{P} = g \left(\frac{\partial \zeta}{\partial x} + i \frac{\partial \zeta}{\partial y}\right) + \frac{1}{\rho_0} \left(\frac{\partial \Pi}{\partial x} + i \frac{\partial \Pi}{\partial y}\right)$,

$$\frac{\partial}{\partial z}(N_z\frac{\partial \mathbf{S}}{\partial z}) - if\mathbf{S} = \mathbf{P} \ .$$

Fig. 5.2 illustrates how the derivative of a function ("f") can be put in finite difference form when the size of the Δx bins vary along x.

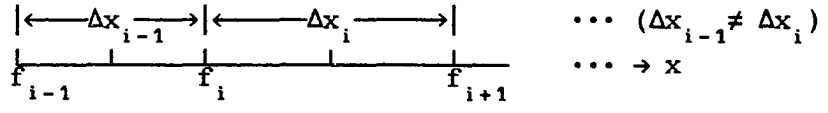

Fig. 5.2. General scheme for first derivative.

The forward difference form for the derivative $\frac{\partial f}{\partial x}$ is $\frac{f_{i+1} - f_i}{\Delta x_i}$. If the function f is defined as $f(x) = g(x)\frac{\partial \mathbf{S}(x)}{\partial x}$, the derivative $\frac{\partial f}{\partial x}$ can be written

$$\frac{\partial}{\partial x}(g\frac{\partial \mathbf{S}}{\partial x}) = \frac{g_i\frac{\mathbf{S}_{i+1} - \mathbf{S}_i}{\Delta x_i} - g_{i-1}\frac{\mathbf{S}_i - \mathbf{S}_{i-1}}{\Delta x_{i-1}}}{\frac{\Delta x_i + \Delta x_{i-1}}{2}} \ .$$

To put the derivative into terms of the z co-ordinate, it is useful to define the counting variable so that l = 0 where z = 0 (undisturbed sea surface), but that as z increases in the negative sense downwards, l increases positively (Fig. 5.3). Also, the function g(x) is now identified as Nz(l), the eddy viscosity, and the bins Δx_i and Δx_{i-1} are written as simply $\Delta(l)$ and $\Delta(l+1)$, respectively.
With this notation,

$$\frac{\partial}{\partial z}(N_z\frac{\partial \mathbf{S}}{\partial z}) = \frac{N_z(l)\frac{\mathbf{S}(l-1)-\mathbf{S}(l)}{\Delta(l)} - N_z(l+1)\frac{\mathbf{S}(l)-\mathbf{S}(l+1)}{\Delta(l+1)}}{\frac{\Delta(l)+\Delta(l+1)}{2}} \ .$$

Nz(l) is evaluated at point midway between points where **S** is evaluated. Simplifying the finite difference expression and inserting it into the Ekman equation evaluated for S(l),

$$- \frac{2\,Nz(l)}{\Delta(l)(\Delta(l)+\Delta(l+1))}\,S(l-1) +$$

$$\left(\frac{2(Nz(l)\Delta(l+1)+Nz(l+1)\Delta(l))}{\Delta(l)\cdot\Delta(l+1)(\Delta(l)+\Delta(l+1))} + if \right) S(l) -$$

$$\frac{2\,Nz(l+1)}{\Delta(l+1)(\Delta(l)+\Delta(l+1)}\,S(l+1) = -P$$

This equation has the identical three-point form to Eq. 2.77 in Ramming and Kowalik (1980), with the following coefficients:

$$a(l) = \frac{2\,Nz(l)}{\Delta(l)(\Delta(l)+\Delta(l+1))} ,$$

$$b(l) = \frac{2(Nz(l)\Delta(l+1)+Nz(l+1)\Delta(l))}{\Delta(l)\cdot\Delta(l+1)(\Delta(l)+\Delta(l+1))} + if ,$$

$$c(l) = \frac{2\,Nz(l+1)}{\Delta(l+1)(\Delta(l)+\Delta(l+1)} , \text{ and}$$

$$d(l) = -P .$$

This equation is solved in Ramming and Kowalik using the line inversion method. The method solves for $S(l)$ as a function of $S(l+1)$ in terms of a two point equation $S(l)=s1(l)S(l+1)+e(l)$, where

$$s1(l) = \frac{c(l)}{b(l)-a(l)s1(l-1)} , \text{ and } e(l) = \frac{d(l)+a(l)e(l-1)}{b(l)-a(l)s1(l)} .$$

The upper boundary condition is that stress is continuous across the interface, i.e., stress $= \vec{\tau}^{w} = \rho_w N_z \frac{\partial S}{\partial z}$. (In this section vector quantities are understood to be complex. Hence $\vec{\tau}^{w} = \tau_x^{w} + i\tau_y^{w}$). Fig. 5.3 illustrates the points near the sea surface.

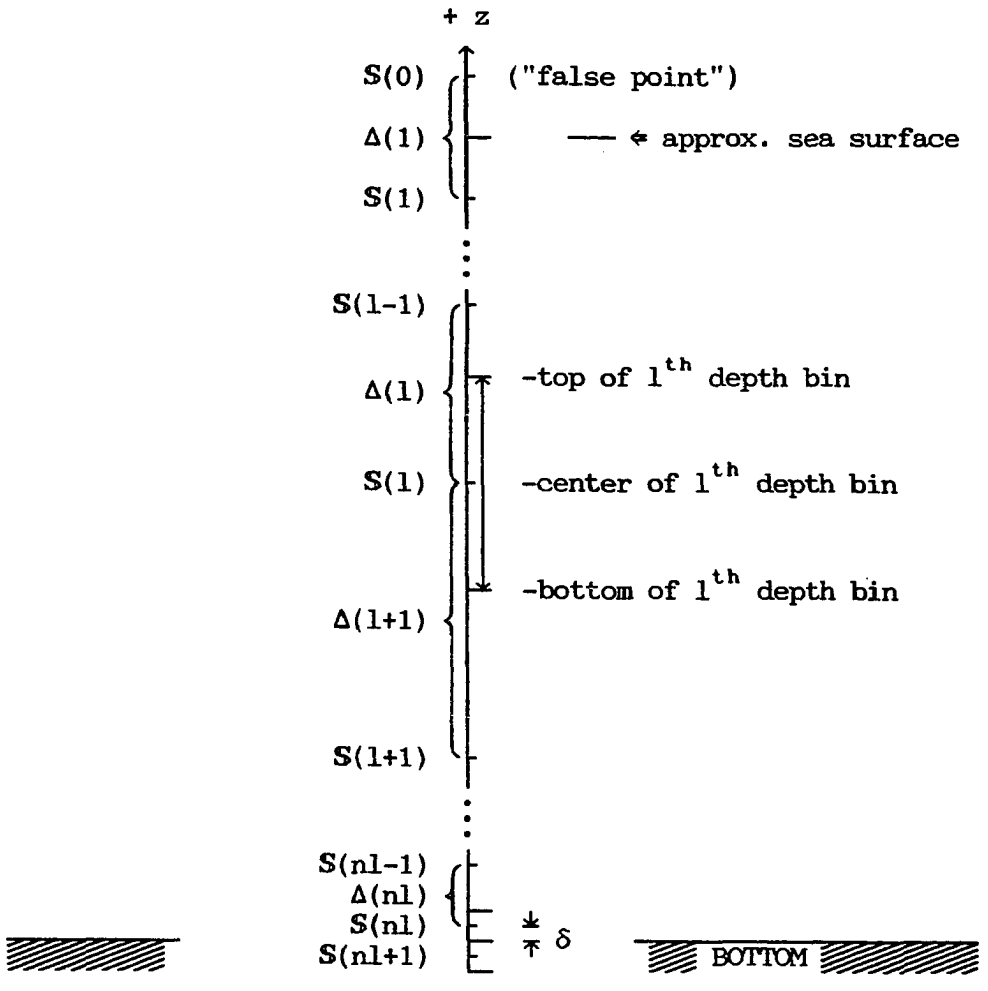

Fig. 5.3. Scheme for finite differences.

The three-point equation at the surface is

$$-a(1)S(0) + b(1)S(1) - c(1)S(2) = d(1).$$

S(0) can be solved for using the formula for windstress

$$\tau^w = \rho_w N_z \frac{\partial S}{\partial z} = \rho_w N_z(1) \frac{S(0)-S(1)}{\Delta(1)} \quad , \text{ so that}$$

$$S(0) = \frac{\Delta(1)\ \tau^w}{\rho_w N_z(1)} + S(1) \ .$$

Entering this expression for S(0) in the three point equation at the surface and solving for S(1),

$$S(1) = \underbrace{\frac{c(1)}{b(1)-a(1)}}_{e(1)} S(2) + \underbrace{\frac{\Delta(1) + \frac{a(1)\Delta(1)\tau^w}{\rho_w N_z(1)}}{b(1) - a(1)}}_{s1(1)}$$

Since every s1(1) and e(1) is a function only of known quantities such as a, b, c, and d, and the $(1-1)^{th}$ value of s1 and e, it is now possible to compute s1(1) and e(1) recursively starting at 1=2 and moving down the z axis to 1 = nl.

Once s1(1) and e(1) are computed for each 1, the velocities are computed recursively upwards by assuming that the velocity is zero at the actual bottom and by using the two-point formula.

For computational convenience, in computing bottom stress, a bin is added beneath the bottom bin (a so-called "false point"). The center of the sub-bottom bin, refered to as "S(nl+1)" in Fig. 5.3, is the same distance, δ, below bottom as the center of the nl^{th} bin is above bottom. The bottom stress, $\tau^b = \rho_w N_z \frac{\partial S}{\partial z}$, is assumed to be constant over the bottom two bins, implying a linear velocity profile between the false point and the nl^{th} point. In difference form, $\tau^b = \rho_w N_z \frac{S(nl)-(-S(nl))}{2\delta(nl)} = \rho_w N_z \frac{S(nl)}{\delta(nl)}$. The computed bottom stress is saved for entry into the general solution. The interaction between the bottom stress condition and the general solution is discussed in the following section.

In the previous section N_z was not assumed to be a constant with depth, but nothing was said about how it was computed. Officer (1976, p.213) provides a functional relationship between N_0, the zero-stratification, zero-mean-shear eddy viscosity, and N_z: $N_z = \frac{No}{1+Ri}$. Here, Ri is the Richardson number, $Ri = \frac{-g\frac{\partial \rho}{\partial z}}{\rho\left(\frac{\partial s}{\partial z}\right)^2}$, where s is the scalar speed, $(SS^*)^{1/2}$. N_z defined in this manner is maximum near the surface, where the turbulence is generated by wind stress, and to diminish with depth, particularly within the thermocline.

With no *a priori* knowledge of the velocity profile, an iterative process must be used to incorporate N_z. A velocity profile is first computed using N_0, and these velocities are used to compute Ri and the

profile of N_z.

5.4 Implementation of the model

Two restrictions existed on the extent of the modeled domain. The first restriction was data coverage; hydrographic data were available only for an area roughly 100 by 100 km. Within that area, coverage was inadequate in certain corners, which were therefore excluded. The second restriction was that of the geometry of the shelf floor. The technique of characteristic tracing restricts the solutions to points which lie along the $\frac{f}{H}$ contours. For the limited area considered these contours closely follow the bathymetry. This was particularly a problem "downstream" of the central part of the transect, where a broad area exists with a uniform depth of 175m. The only contours which could be drawn with certainty were those adjacent to this flat area (Fig. 5.4). This leaves a broad area with no streamfunction computations.

A rectangular grid consisting of 26 X 29 nodes at 2 nm spacing was placed over the domain. Not all points on the grid were computed; those which are on land or too far from a hydrographic measurement are outside the boundary in Fig. 5.4. The 2 nm spacing was chosen to take advantage of the accuracy with which the bathymetry was known, thereby reducing the uncertainty of the integration path.

After digitizing the depths, each point was converted to a value of $\frac{f}{H}$, and the $\frac{f}{H}$ contours were drawn. Points were then chosen along each contour leading away from the location where it crossed the PCM transect. The spacing along the contour where the streamfunction is solved for (the "contour points") is approximately 2 nm intervals, or slightly less where required by the curvature of the contour. They do not in general lie on grid nodes.

The data from the profiling current meter transect on 11 September 1983 was used to estimate the streamfunction boundary condition. The transect bisects the model domain, crossing all the contours in Fig. 5.4. These data were found in the previous chapter

(see Table 4.2) to be the best representation of the "average" conditions. The time elapsed between the start and finish of the transect was 14 hours. Using these data to estimate a subinertial mean streamfunction inevitably results in errors from shorter period processes such as tidal velocities and inertial currents. The effect of these errors is most important in the mean velocity field which is computed from the streamfunction gradients as a check on the velocities computed by the Ekman solutions. The sealevel slopes are less affected by errors in the streamfunction gradients.

Before the characteristic tracing model (CTM) is run, the forcing function and depth gradient fields are computed. The density observations are interpolated at every five meters of depth from top to bottom over the grid. Various interpolation schemes were considered for this purpose. The scheme that was chosen uses the six nearest observations and weights them according to inverse distance to the fourth power. Once the three dimensional density distribution over the rectangular grid has been determined, the forcing functions such as Φ were determined through integration over depth. The horizontal gradients of the density-related variables such as Φ were computed by central finite differencing. A cubic spline method originally used for this purpose proved unsatisfactory due to problems at the endpoints.

Integration along contours begins at the transect/contour crossings, on the CF line (Fig. 5.4), where Ψ is known, and proceeds along a specified direction until the value of Ψ at the endpoint has been computed. The integration then reverses, and proceeds back through the starting point to the far end of the contour. The new (computed) value of Ψ at the CF transect crossing is checked against the input value to assure no errors have been generated.

When Ψ has been computed along the contours, it is necessary to transform to the rectangular grid domain to compute derivatives. This is performed by interpolating Ψ to the grid nodes using the four nearest estimates and inverse fourth power weighting. When a value of streamfunction has been assigned to each node, the derivatives $\frac{\partial \Psi}{\partial \lambda}$ and $\frac{\partial \Psi}{\partial \phi}$ are calculated using central differences.

Eqs. 5.13 and 5.14 express the gradient of sealevel in terms of the gradients of streamfunction, depth, density anomaly, and surface and bottom stresses. Ignoring bottom stress on the first iteration, these equations are used to calculate a first estimate of sealevel gradient. After sealevel gradients are estimated over the domain, a five-point bi-directional filter is run over the computed values to remove small spatial scale noise arising from the numerical procedure.

The sealevel slopes, z-dependent gradient of integrated density anomaly, the density profile itself, the depth, and the windstress vector are passed to the Ekman solution subroutine at each grid node. The velocity profile is returned along with an estimate of bottom stress. The values of bottom stress are used in the second iteration for Ψ, and the computation procedes iteratively until convergence is achieved. A relative convergence criterion is used to test each new value of bottom stress. When the relative change from the previous iteration is less than .01 at every node, computation is ended.

5.5 Model results

The grid-interpolated matrix of Ψ was machine-contoured by SURFACE II, and the results reproduced in Fig. 5.5. At the shoreline, Ψ goes to zero; it also gets smaller in the middle shelf, over a shoaling region. Water approaching along a streamline from the east is forced to the north or south of the shoaling region. The streamlines passing to the south appear to bend north after passing the shoaling region. The streamlines between $-4 \cdot 10^5 m^3/s$ and $-7 \cdot 10^5 m^3/s$ on the northern side tend to become slightly crowded in the vicinity of the CF line, which may explain the commonly observed double maximum in the Alaska Coastal Current (Johnson *et al.* 1988): a more offshore maximum may be associated with the streamlines bending north of the shoaling region, and another maximum closer to shore associated with water exiting from Prince William Sound.

Four terms enter into the computation of sealevel slope (Eqs. 5.13, 5.14). Over most of the grid, the dominant term is the

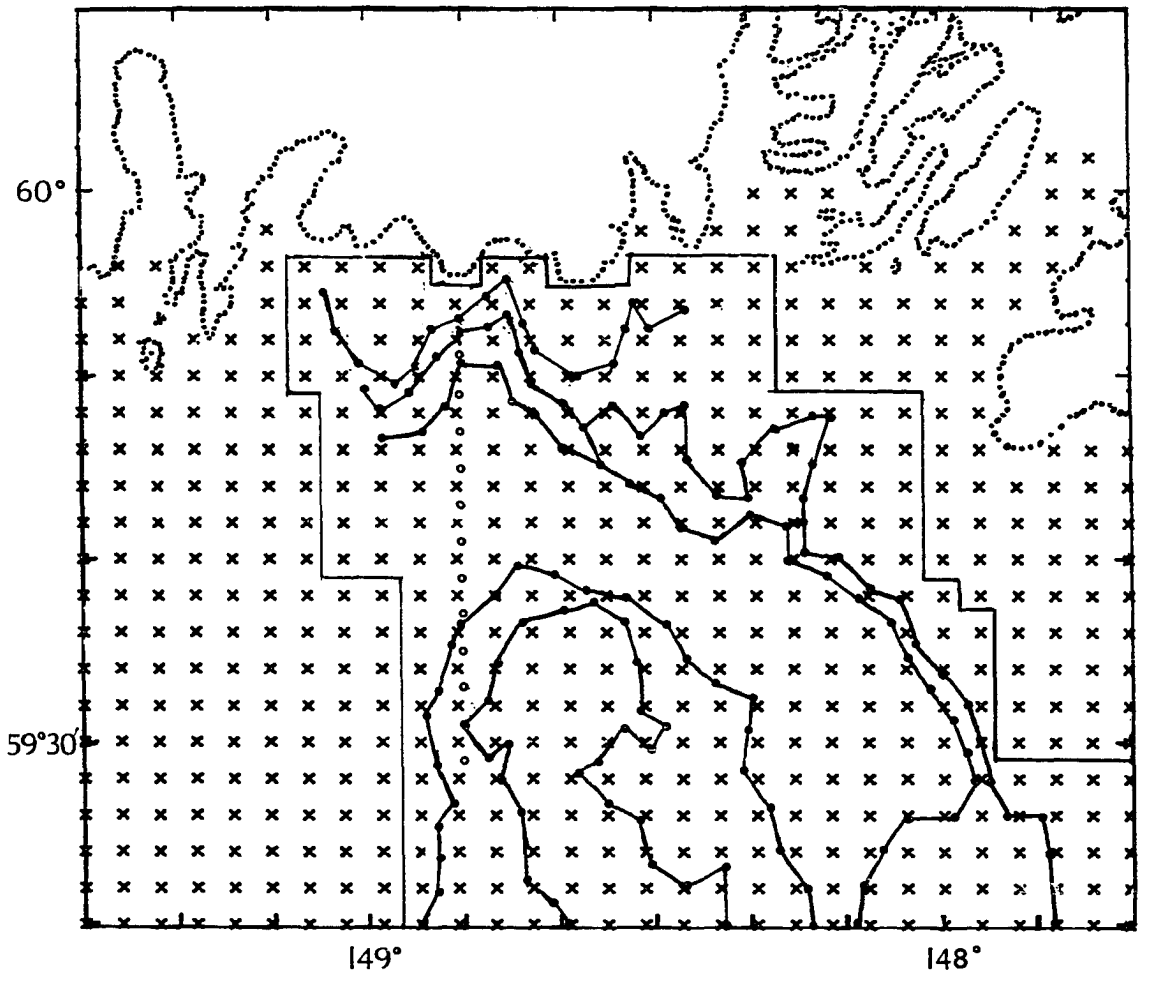

Fig. 5.4. Numerical grid (indicated by crosses), and contours of f/H . Points for computation of Ψ along contours are indicated by dots. Small circles represent PCM stations (locations where Ψ is considered known). Computation of sealevel, velocity, etc. was restricted to the enclosed subregion.

integrated density anomaly. The derivatives of Ψ and Φ occasionally have the largest magnitude (of the four), but in general, they are perhaps half the size of the integrated density anomaly. The bottom and surface stresses enter as relatively small corrections, usually about a tenth the size of the integrated density anomaly term. This might be the result of the data used in the model having been collected during and following a period of light and variable winds. The contribution of the density gradients to the sealevel slopes is nonetheless indicative of the importance of the density distribution and hence the freswater inflow as a driving force.

Sealevel above a reference level at the southeast corner was calculated by integration of the gradient first along the southern boundary, and then northward to the northern boundary (Fig. 5.6). The sealevel rises sharply up over the inner third of the shelf. This supports the statistical results of Royer (1981), who concluded that the coastal current was separated from outer shelf sealevel gradients by the mid-shelf region. While the change in sealevel between the coast and the southern boundary of the domain is as large as 25 cm in less than 70 km, the sealevel fluctuates within a range of 3 cm along the 75 km southern boundary.

The vertically averaged horizontal velocities are presented in Figs. 5.7 and 5.8. The averages are computed in two different ways as a model test. The first method (Fig. 5.7) computes an average of the velocity profile (Ekman solution) over the vertical. The second method (Fig. 5.8) is determined through differentiation of the streamfunction. Although the two methods do not give identical results, they are very similar.

The vertically averaged PCM velocity profiles are compared with the model profiles from the nearest gridpoint in Fig. 5.9. The u components (primarily alongshore) tend to agree quite well. The first column of arrows in Fig. 5.9 represents the mean velocity vector from the PCM data, the second column are the model results for the same points, according to the vertical integration of the Ekman profiles, and the third column are also model results, except $\bar{u}$ and $\bar{v}$ are

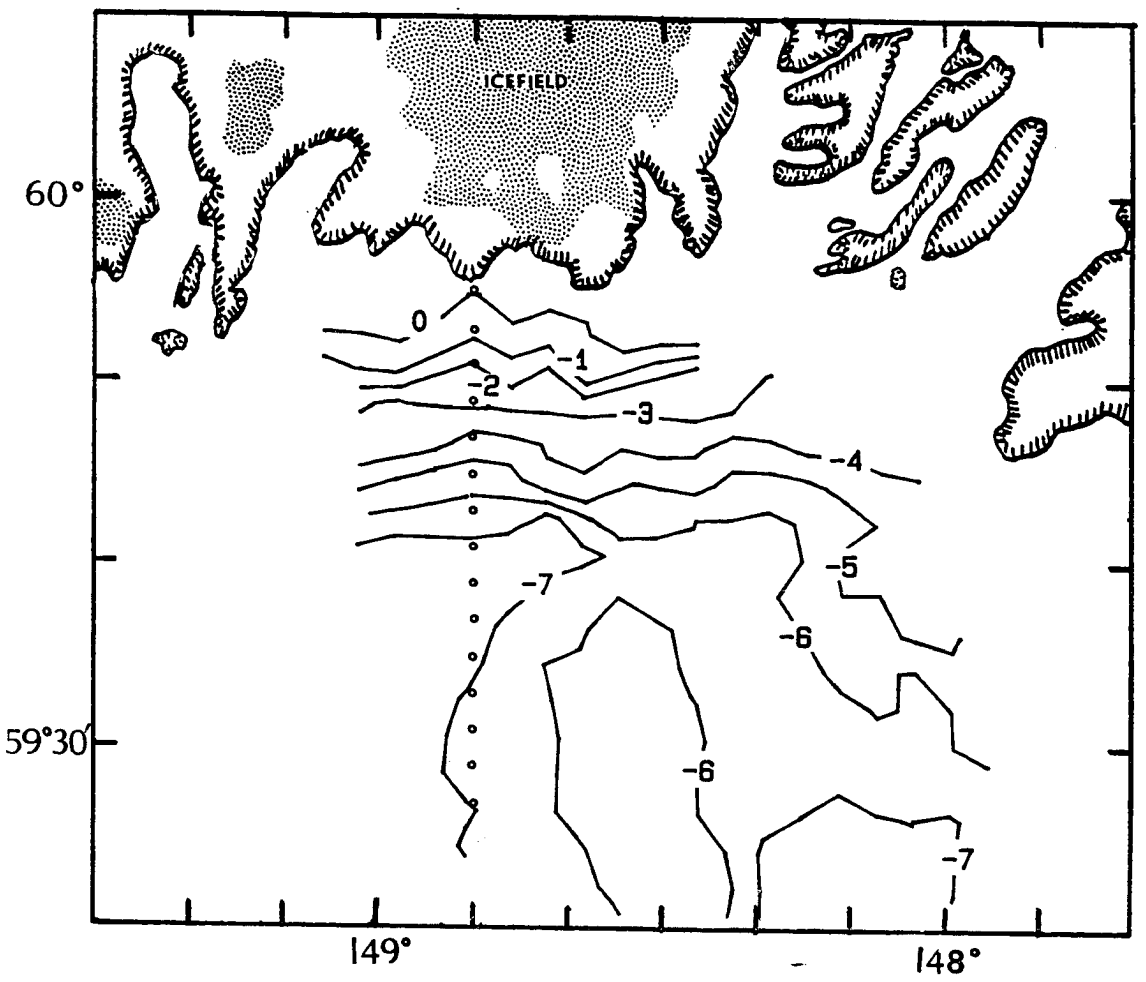

Fig. 5.5. Streamfunction (Ψ) contours in units of $10^5 \frac{m^3}{s}$.

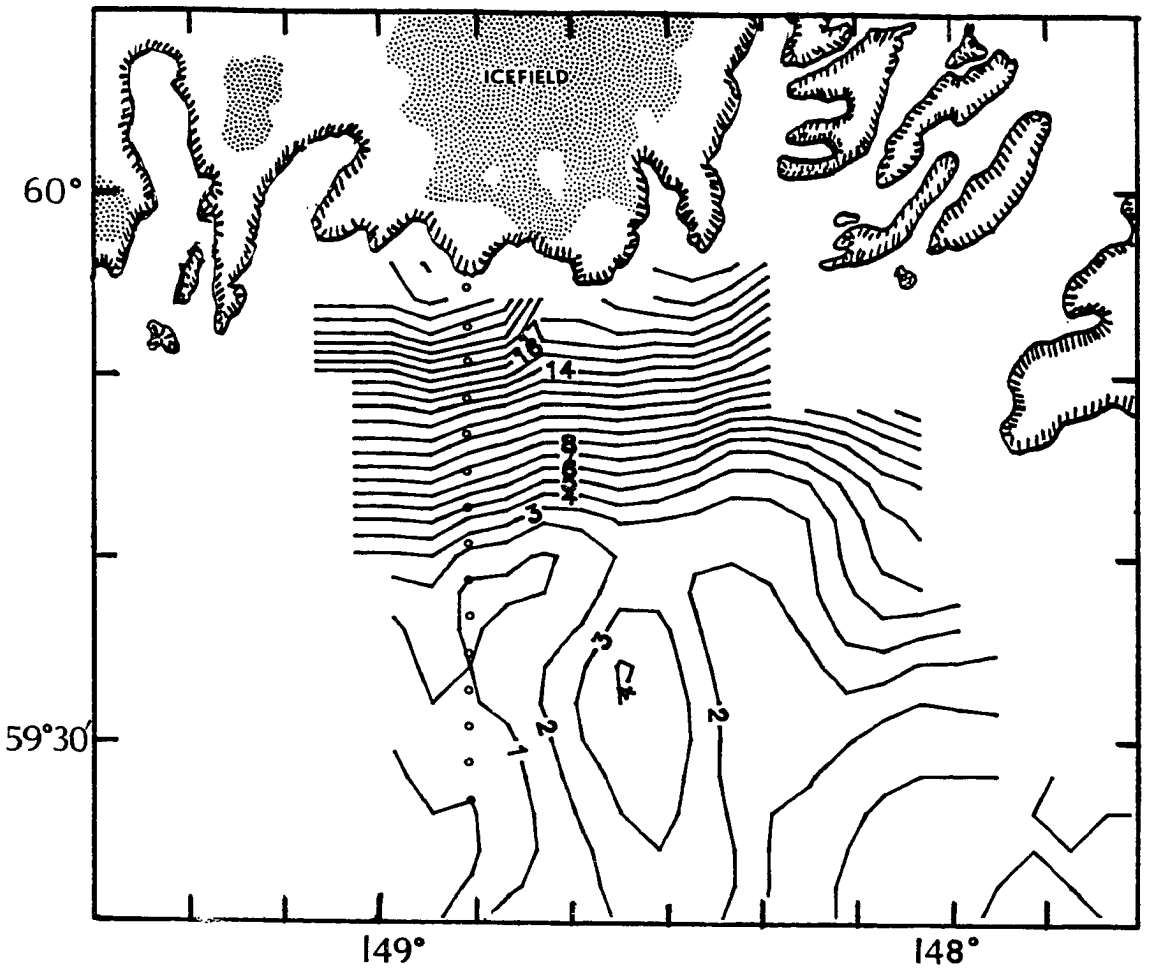

Fig. 5.6. Sealevel (cm) referenced to arbitrary zero in lower right hand corner.

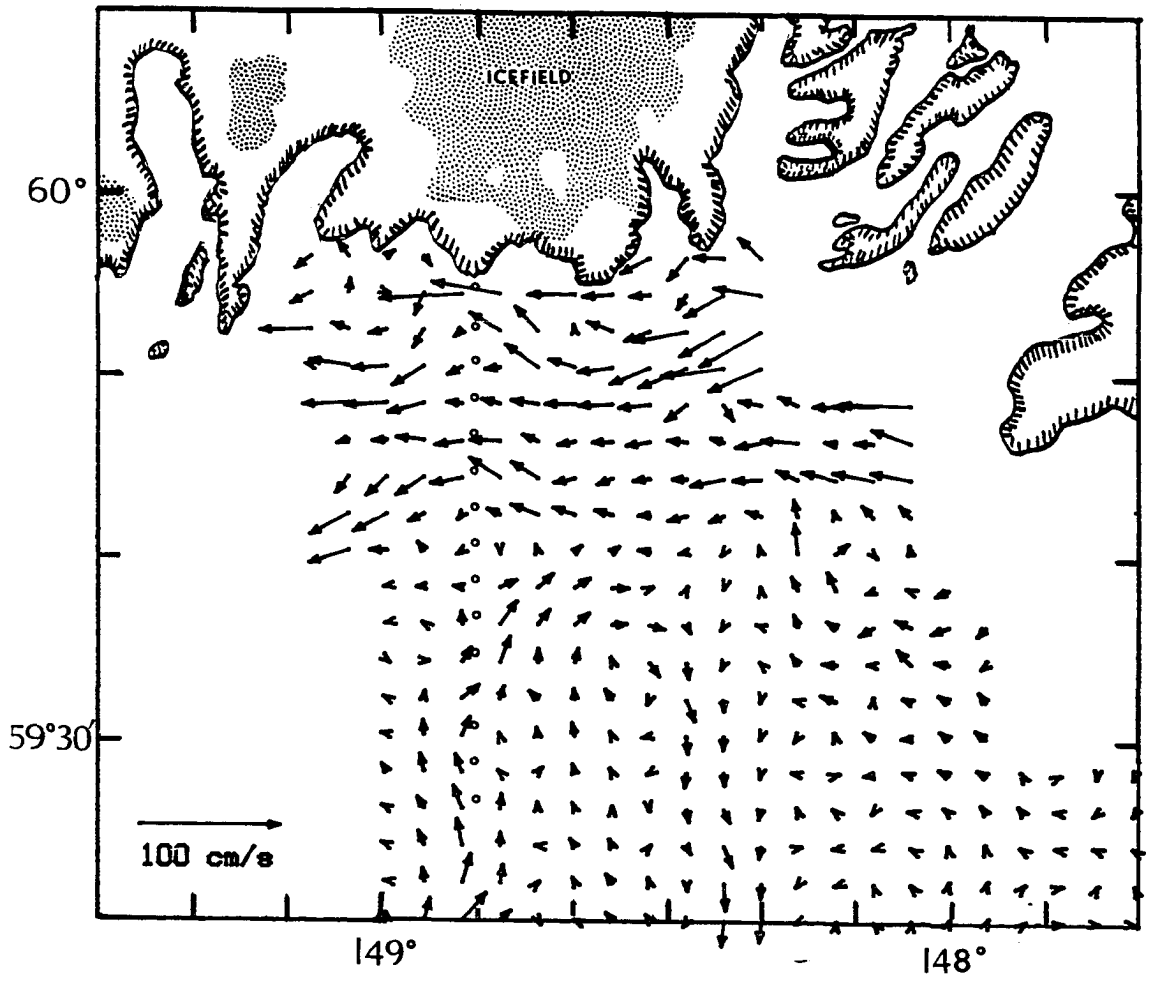

Fig. 5.7. Vectors of mean velocity, computed by vertically averaging the horizontal velocity profiles. Small circles represent PCM stations (locations where Ψ is considered known).

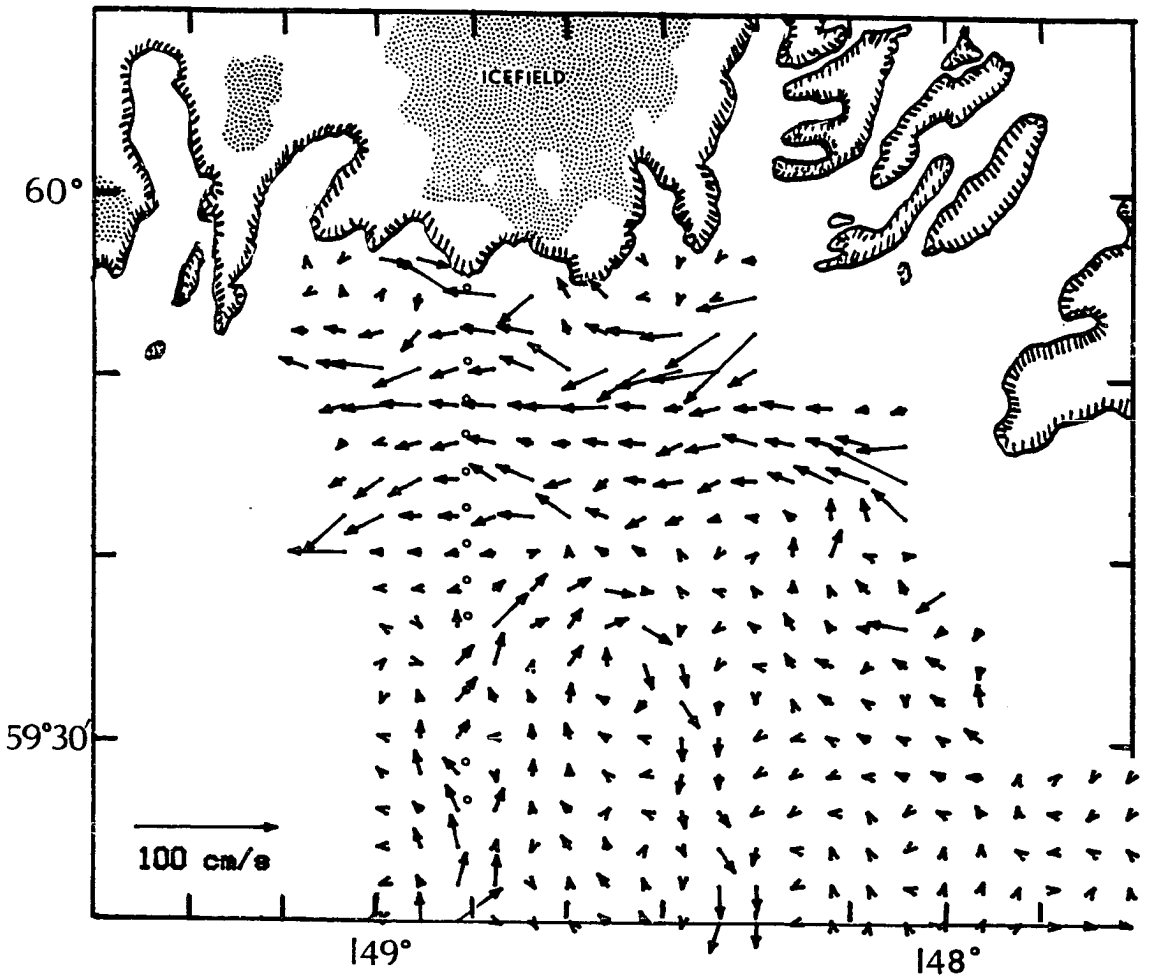

Fig. 5.8. Vectors of mean velocity, computed from the definition of streamfunction. Small circles represent PCM stations (locations where Ψ is considered known).

computed from the definition of the streamfunction. In most cases, $\bar{u}$ is nearly identical, but $\bar{v}$ in several cases varies not only in size but in sign. Discrepancies between the PCM and model profiles can be attributed generally to uncertainty in the east-west sealevel slope. While the uncertainty is the same in either direction, the relative error is much larger for the east-west slope, which is an order of magnitude smaller than the north-south slope.

Another reason for the difference between the measured and modelled across-shelf mean velocity is apparent in Figs. 5.7 and 5.8. The PCM transect is shown by small circles. The PCM transect is located along a meridion where the across-shelf component of velocity changes sign between the upstream and downstream sides. This sign change is probably due to the shape of the coastline at Cape Fairfield, which forces the mean flow to switch from an onshore to an offshore direction.

An interesting prediction of the tracing technique was an unexpected increase in the streamfunction gradient at the farthest offshore points. A re-examination of the single density section which extended south of the model domain to the shelf break confirmed the existence of an outer shelf current (using the geostrophic method, 150 db reference level). The outer shelf in this region is thought to have highly variable currents with considerable eddy activity (Niebauer *et al.*, 1981).

The velocity profiles computed by the model are compared with the PCM for two locations, one within the core of the current and one well outside the core, in Fig. 5.10. The alongshore (u) component within the core, at CF 3, shows good agreement, with a maximum at the surface, decreasing due to the opposing baroclinic pressure gradient to zero near 100 m (75 m in the case of the PCM). Between 100 m and the bottom, the flow reverses. The v component is onshore at the surface and offshore below 10 m, except near the bottom, where the flow is onshore. Outside the core, at CF11, the surface flow is zero, but a small baroclinic flow appears below the surface due to isopycnal slopes in the shallow pycnocline.

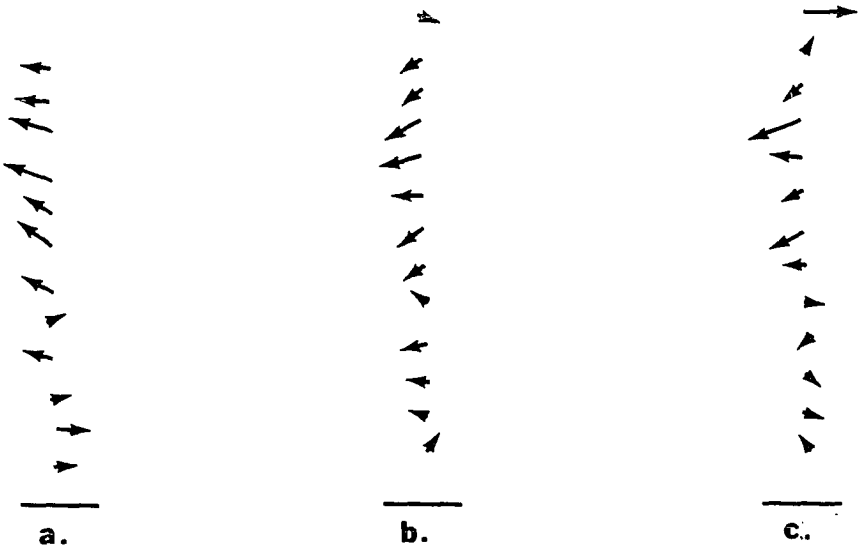

Fig. 5.9. Vectors of mean velocity along CF section, computed by three different sources. The sources are a) as measured by the PCM, b) by vertically averaging the horizontal velocity profiles, and c) from the definition of streamfunction.

In plan view (Fig. 5.11a), the surface velocity maximum is clearly characteristic for the ACC. The decrease in velocity below the surface is detectable at 15 m (Fig. 5.11b), and at this scale, the ACC has disappeared at 70 m. The convergence of the PWS water into the ACC is also visible in the surface currents. The flow at the surface and at 15 m at the location of the current meter is offshore, in agreement with the monthly averages of the 2 m and 50 m currents meters (Fig. 4.5b). The clockwise eddy or meander around the shoaling area offshore of the core, which appears to draw water onshore across the shelf, is discernible at all depths.

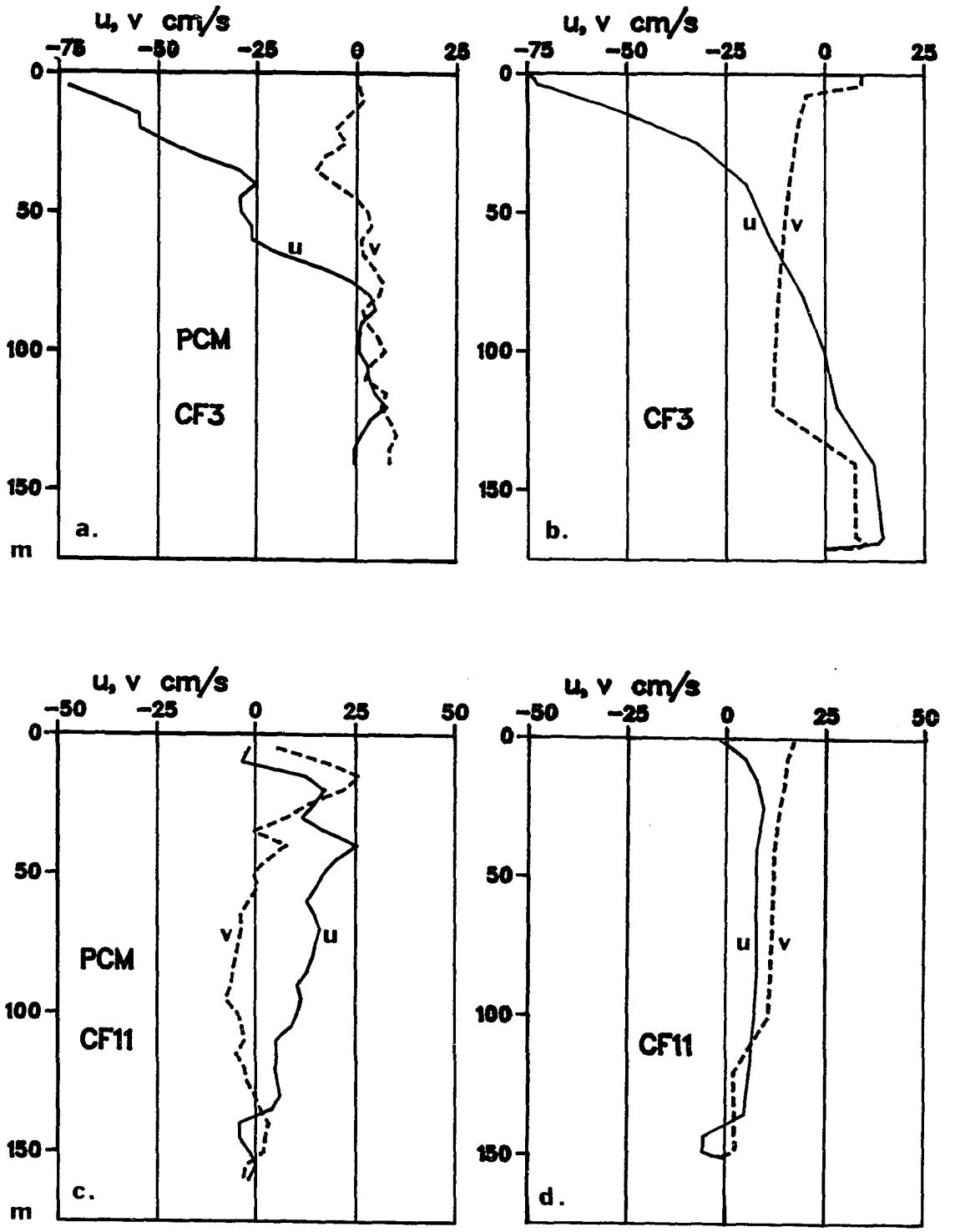

Fig. 5.10. PCM (a and c) and model (b and d) velocity profiles at CF3 (8 km offshore) and CF11 (38 km offshore).

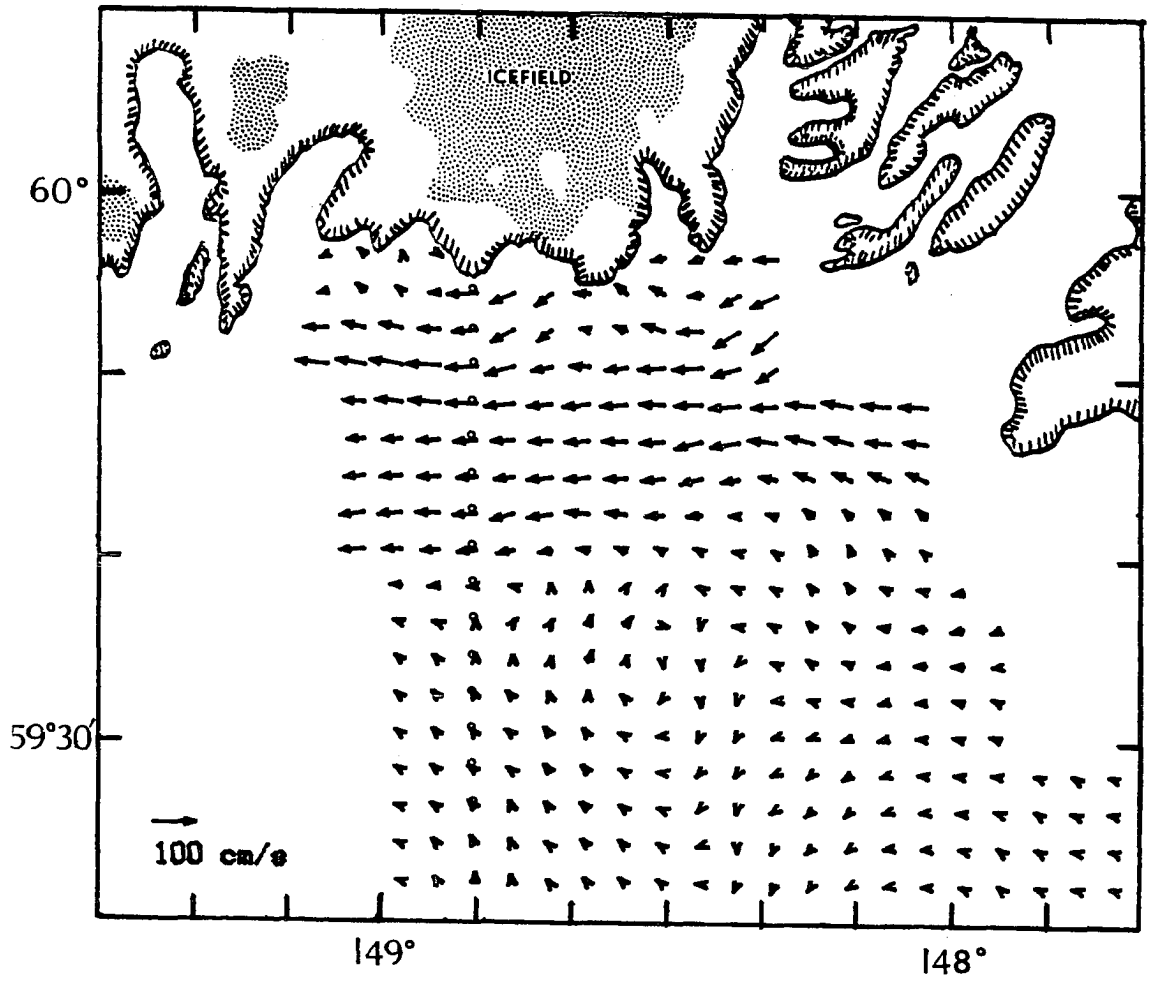

Fig. 5.11a. Velocity at surface.

Fig. 5.11. Velocity vectors at representative depths.

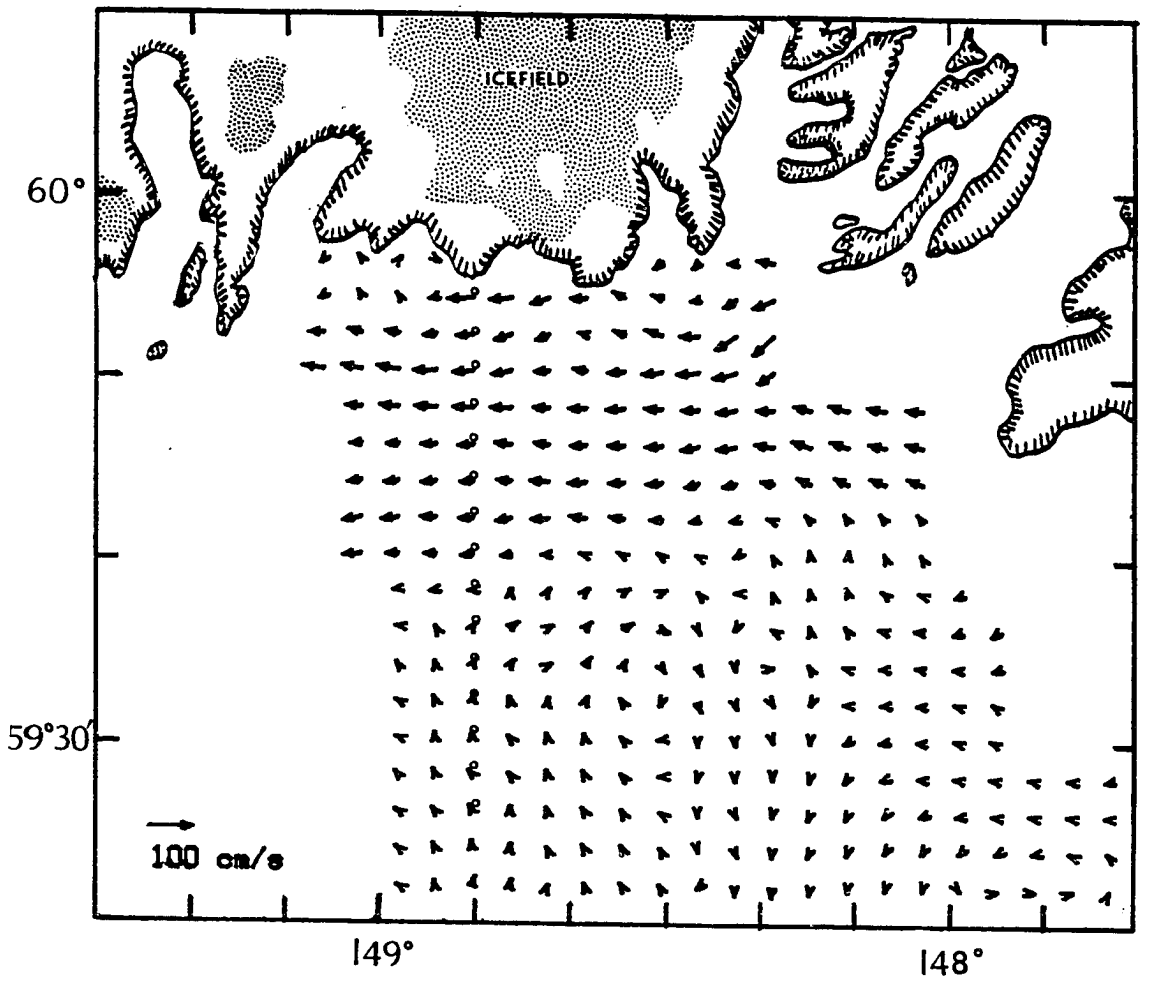

Fig. 5.11b. Velocity 15 m below surface.

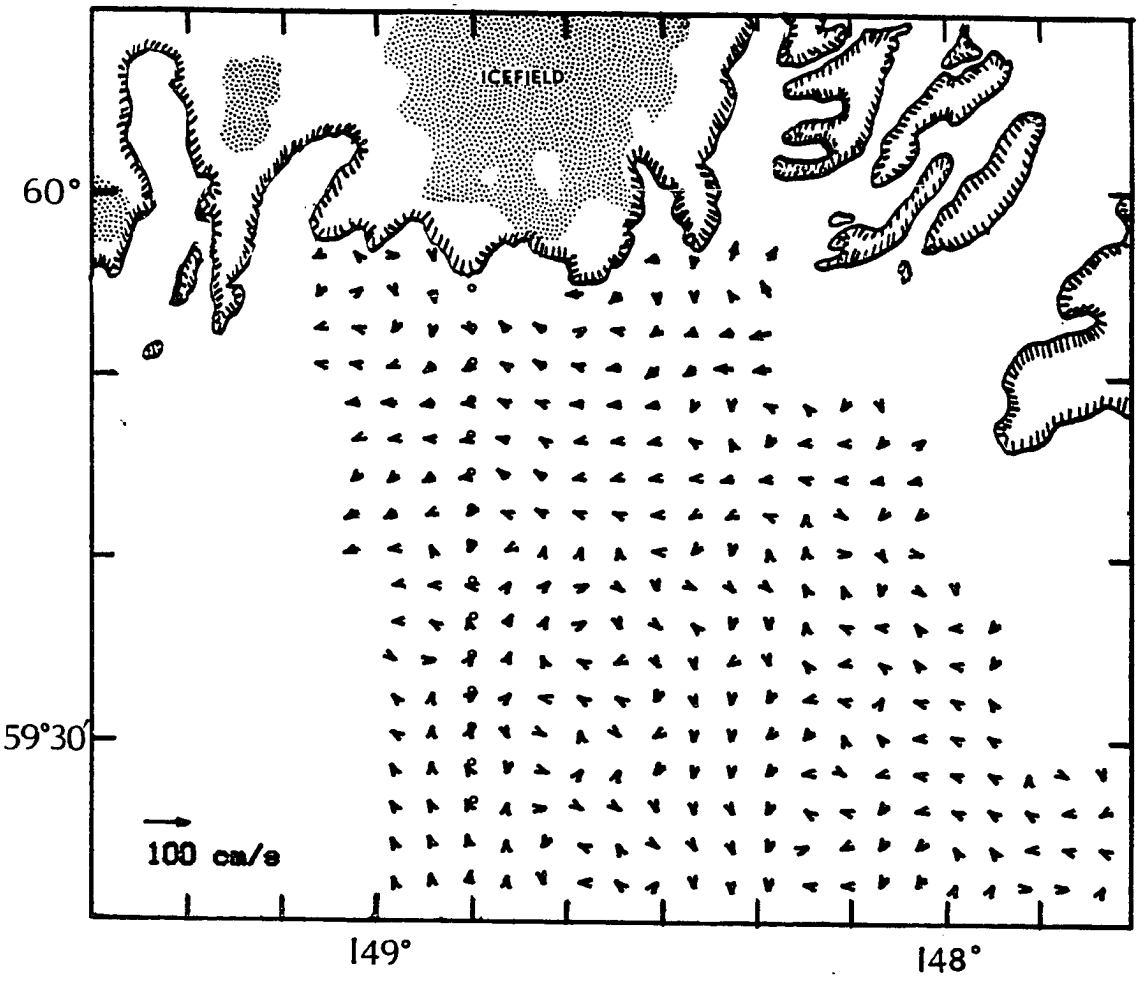

Fig. 5.11c. Velocity 70 m below surface.

Chapter 6. SUMMARY AND CONCLUSIONS

The Alaska Coastal Current has been studied from a variety of standpoints: water mass characteristics, short period oscillations, seasonal variability, the roles of temperature and salinity, and the momentum balance. From these approaches, together with previous studies both of the ACC and related coastal currents, an improved understanding is emerging which can be applied to buoyancy-driven coastal currents in widely separated parts of the globe.

The outflow from Prince William Sound onto the coast has been identified by this investigation as being of central importance to the flow in the study area. PWS acts as a large dilution basin, with a coastline of roughly 600 km, and a restricted exchange of oceanic water through Hinchinbrook Entrance (Schmidt, 1977). The cross-shelf contrast provided by the lighter PWS band effectively reinforces the ACC. Its convergence with the ACC in Blying Sound allows the PWS outflow to remain as a distinct nearshore band, as revealed by consecutive downstream cross-sections of "τ", a density flux function. The PWS outflow could be traced due to the fact that the its range of "τ" was distinct from that of the outer shelf water. This method for separating the outflow of a point source from a confluent shelf circulation may prove useful in other regions where the cross-shelf contrast in temperature, salinity, and density alone are not definitive.

A shoaling region, with depths decreasing to 75 m, surrounded by a shelf which otherwise ranges between 175 m and 225 m, appears to affect significantly the course of flow in Blying Sound. According to the model, the ACC bifurcates around the shoal. The portion which flows north of the shoal coalesces with the outflow from PWS to form a single core, or remains separate to form a double core. The southern portion deflects northward after passing the shoal, forming a semi-permanent meander on the "downstream" side. This meander, visible in the dynamic topography, advects water onshore across the shelf. Kantha *et al.* (1982) applied a diagnostic model without bottom

friction to the Mid-Atlantic Bight region north of the Straits of Florida, and predicted a similar stationary cyclonic eddy over the shoal known as the "Charleston Bump", and Pettigrew and Murray (1986) mention a meander in the Nicaraguan Coastal Current, directed nearly perpendicular to the coast. These may all be caused by the same vorticity constraints on the depth-averaged flow discussed in the preceding chapter.

The input of fresh, buoyant water at the coast results in a rise in sealevel of about 25 cm over 70 km. This sealevel gradient is associated with a surface jet which reaches speeds greater than 100 cm/s. At the same time, the isohaline surfaces, which slope upward offshore, compensate for the sealevel gradient by setting up an opposing baroclinic pressure gradient, so that the net horizontal pressure gradient vanishes at a depth of approximately 100 m. The conceptual model of a "floating jet", as applied to the ACC, is somewhat misleading, however. Although baroclinic compensation confines the ACC to the upper half of the water column, so that the velocity core is decoupled from the bottom topography, there are obvious topographic influences. One of these is the shoaling region in mid-Blying Sound. Another example is the southward-trending bottom contour at the location of the current meter mooring, that is partly responsible for the offshore monthly-averaged flow near the surface (despite downwelling-favorable winds). This is consistent with the results of diagnostic studies elsewhere. Hsueh and Peng (1978) concluded that the bottom boundary layer was an important factor in the direction of the residual mean flow over the Oregon continental shelf.

The momentum balance equations proposed in Chapter 5 correctly reproduced the meandering current associated with the shoaling region. It should be noted that another mechanism exists which can account for this type of behavior. Lagerloef (1983) found evidence that the inertial (the "nonlinear", or "advective") terms in the momentum equations (which were neglected here) could account for topographic control in a barotropic flow over a submarine canyon, and Eide (1979)

detected a topographically trapped *anti*cyclonic vortex in a stratified flow over a bank which he reproduced in a model similar to that of Lagerloef's. Using scaling arguments, the inertial terms were found to be of secondary importance in the September, 1983 data set from Blying Sound. The largest of these terms is $v \frac{\partial u}{\partial y}$. An upper limit on this term is for v = .1 m/s, and u = 1.2 m/s, confined to a core region (a Δy) of $.5 \cdot 10^4$m. The inertial term then is $\simeq 2.5 \cdot 10^{-5} m^2/s$. For the same conditions, the Coriolis term is $1.7 \cdot 10^{-4} m^2/s$, nearly an order of magnitude larger.

Another term may contribute to the momentum balance in certain applications. The shoreline curvature also constrains coastal currents, and if the velocity is sufficient, and the radius of curvature small enough, the centrifugal term in the momentum equation can not be ignored (Neumann, 1968, p. 155). Kozo (1982) found this to be important to the dynamics of sea breezes along the Alaskan Beaufort Sea coast. The centrifugal acceleration is c^2/r, where c is the speed, and r the radius of curvature of the flow. Choosing values for upper limits of the term, c=1.2 m/s, and $r=100 \cdot 10^3$ m, then $c^2/r \simeq 1.4 \cdot 10^{-5}$. Compared to the coriolis acceleration, $fc \simeq 1.2 \cdot 10^{-4} m^2/s$, the centrifugal term can safely be ignored. While this is probably always true for the ACC, it in not necessarily true for all coastal currents.

There is no single accepted method of incorporating bottom friction in models of shelf circulation. For deep bathymetry, bottom friction is often ignored (Kantha *et al.*, 1982), and for bathymetry with depths of less than 50 m and higher velocities, a quadratic dependence on velocity is often used (Lentz, 1984). An advantage of the shear stress formulation used in this study is that the equations are consistent with the integrated Ekman equations of Eq. 5.7 without requiring any additional assumptions. The model results were not very sensitive to the choice of the eddy viscosity coefficient at the bottom or to the implementation of the stress condition in the solution for $\vec{u}(z)$ in Section 5.3. This formulation was successful and is likely to work in a wide variety of depths and conditions.

The mean cross-shelf sealevel gradient was attributed to

freshwater discharge rather than wind stress, which was weak during and preceding the model study period. In other words, the model provides a physical confirmation of earlier statistical correlation studies of Royer (1981). By extension, it also supports the conclusions of Murray and Young (1985), who used a semi-analytic model to study the Nicaraguan Coastal Current. They calculated a similar sealevel gradient and also associated it with the freshwater input along the coast. The gradient predicted by the diagnostic model of the ACC, .3 cm/km, is large enough to be directly measureable by bottom pressure sensors. An array of sensors between the 75 and 200 m isobaths would provide a check on the model results. The sensors could be "calibrated" by assuming the sealevel gradient was zero following a low wind period in April or May, when freshwater discharge is at a minimum, and by assuming the gradient was zero at the offshore boundary at all times.

While our understanding of coastal circulation has improved dramatically over the past two decades, it is still incomplete. Certain processes, such as wind-driven upwelling, have received particular attention (Wooster, 1981), with a commensurate broadening and accuracy of the model physics. However, models of coastal circulation are still at a point where constrictive assumptions must be made. The steady-state, diagnostic model can explain a limited, carefully chosen set of phenomena, but even those presumptions must be reconsidered before the model can be universally applied. Experience has shown this to be true, since the buoyancy-driven coastal circulation models (in particular, Murray and Young (1985) and Heaps (1980)), were attempted to be adapted to this region prior to the success of this diagnostic model. On the other hand, many of the insights gained by a regional model can be applied generally in the study of the circulation in widely separated coastal areas. Finally, the success of the diagnostic approach in application to an area as topographically and dynamically complex as Blying Sound indicates that with a relatively small number of fixed current meters or pressure sensors, and routine hydrographic data, the mean velocity field can be

solved for in three dimensions over a wide area.

The model concurs with direct measurements in indicating that the flow reverses below some depth (approximately 100 m at the core, rising to 0 m outside the ACC) and has onshore components at certain depths depending on location. Fish larvae may take advantage of the reversed flow in order to remain within a particular portion of coastline, and the onshore flow may help ensure the fish larvae are not swept off the shelf. For example, in Blying Sound, a larval fish could remain over the shoal region without expending undue energy against the mean flow.

REFERENCES

Ahlnaes, K., T.C. Royer, and T.H. George, Multipole dipole eddies in the Alaska Coastal Current detected with Landsat Thematic Mapper data, *J. Geophys. Res., 92*, 13041-13047, 1987.

Atkinson, L.P., J.O. Blanton, and E.B. Haines, Shelf flushing rates based on the distribution of salinity and freshwater in the Georgia Bight, *Estuarine Coastal Mar. Sci., 1*, 462-472, 1978.

Csanady, G.T., Mean circulation in shallow seas, *J. Geophys. Res., 81*, 5389-5399, 1976.

Csanady, G.T., The Coastal Boundary Layer, in *Geophysics and the Environment*, pp. 57-70, ed. by C. Officer, National Academy of Sciences, U.S.A., Wash. D.C., 1977.

Csanady, G.T., *Circulation in the Coastal Ocean*, 279 pp., D. Reidel, Dordrecht, Holland, 1982.

Eide, L.I., Evidence of a topographically trapped vortex on the Norwegian continental shelf, *Deep Sea Res., 26/6A*, 601-621, 1979.

Fischer, H.B., Mixing processes on the Atlantic continental shelf, Cape Cod to Cape Hatteras, *Limnol. Oceanogr.,25*, 114-125, 1980.

Fomin, L.M., *The Dynamic Method in Oceanography*, 212 pp., Elsevier, Amsterdam, 1964.

Galt, J.A., A finite element solution procedure for the interpolation of current data in complex regions, *J. Phys. Oceanog., 10*, 1984-1987, 1980.

Galt, J.A., and G. Watabayashi, The linear decomposition of a diagnostic shelf circulation model and discussion of alternate boundary condition formulations, *OCSEAP Final Reports of Principal Investigators*, 26, pp. 453-694, U.S. Dept. Commerce, 1984.

Greisman, P., Western Gulf of Alaska Tides and Circulation (Final Report), 112 pp., Dobrocky-Seatech Ltd., Sidney, B.C., 1985.

Griffiths, R.W., and P.F. Linden, The stability of buoyancy driven coastal currents, *Dyn. of Atmos. and Oceans, 5*, 281-386, 1981.

Hayes, S.P. and J.D. Schumacher, Description of wind, current, and bottom pressure variations on the continental shelf in the

northeast Gulf of Alaska from February to May 1975, *J. Geophys. Res.*, 81, 6411-6419, 1976.

Heaps, N.S., Density currents in a two-layered coastal system, with application to the Norwegian Coastal Current, *Geophys. J. R. Astron. Soc.*, *63*, pp. 289-310, 1980.

Heaps, N.S., *Three-Dimensional Coastal Ocean Models*, 208 pp., Amer. Geophys. Union, Wash., D.C., 1987.

Hendershott, M.C., Long waves and ocean tides, in *Evolution of Physical Oceanography*, ed. by Warren, B.A. and C. Wunsch, The MIT Press, Cambridge, Mass., 1981.

Hsueh, Y. and C.Y. Peng, A Diagnostic model of shelf circulation, *J. Geophys. Res.*, 83, 3033-3041, 1978.

Jackett, D.R. and T.J. McDougall, An oceanographic variable for the characterization of water masses, *Deep-Sea Res.*, 32, 1195-1207, 1985.

Jenkins, G.M., and D.G. Watts, *Spectral Analysis and its Applications*, 525 pp., Holden-Day, Oakland, California, 1968.

Johnson, W.R. and T.C. Royer, A comparison of two current meters on a surface mooring, *Deep-Sea Res.*, 33, 1127-1138, 1986.

Johnson, W.R., T.C. Royer, and J.L. Luick, On the seasonal variability of the Alaska Coastal Current, in press, *J. Geophys. Res.*, 1988.

Kantha, L., A.F. Blumberg, and G.L. Mellor, A diagnostic technique for deducing the climatological circulation as applied to the South Atlantic Bight, Dynalysis of Princeton Report No. 69, 124 pp., 1981.

Kantha, L., G. Mellor, and A. Blumberg, A Diagnostic calculation of the general circulation of the South Atlantic Bight, *J. Phys. Oceanog.*, 12, 805-819, 1982.

Kantha, L., H.J. Herring, and G.L. Mellor, South Atlantic OCS circulation model - Phase III, Dynalysis of Princeton, Report No. 91, 153 pp., 1986.

Kao, T.W., The dynamics of ocean fronts. Part II: Shelf water structure due to freshwater discharge, *J. Phys. Oceanog.*, 11,

1215-1223, 1981.

Kozo, T.L., An observational study of sea breezes along the Alaskan Beaufort Sea coast: part I, *J. Applied Meteorology*, 12, 891-905, 1982.

Kundu, P. K., Ekman veering observed near the ocean bottom, *J. Phys. Oceanog.*, *6*, 238-242, 1976.

Lagerloef, G., Topographically controlled flow around a deep trough transecting the shelf off Kodiak, Alaska, *J. Phys. Oceanog.*, *13*, 139-146, 1983.

LeBlond, P.H., B.M. Hickey, and R.E. Thomson, Runoff Driven Coastal Flow off British Columbia, in *NATO ASI Series, G7*, 309-317, ed. by S. Skreslet, Springer-Verlag, Berlin, 1986a.

LeBlond, P.H., W.J. Emery, and T. Nicol, A Climatic Model of Runoff-driven Coastal Circulation, *Est., Coastal, and Shelf Sci.*, 23, 59-79, 1986b.

Lentz, S.J., Subinertial motions on the Southern California continental shelf, PhD. Thesis, 145 pp., University of California, San Diego, 1984.

Livingstone, D.M., and T.C. Royer, Observed surface winds at Middleton Island, Gulf of Alaska and their influence on the ocean circulation, *J. Phys. Oceanog.*, 10, 753-764, 1980.

Luick, J.L., W.R. Johnson, and T.C. Royer, Variations in the Alaska Coastal Current, Transactions, Amer. Geophys. Union, 67, p. 1042, 1986.

Luick, J.L., T.C. Royer, and W.R. Johnson, Coastal atmospheric forcing in the northern Gulf of Alaska, J. Geophys. Res., 92, 3841-3848, 1987a.

Luick, J.L., T.C. Royer, and W.R. Johnson, Some aspects of Modeling the Alaska Coastal Current, Int'l. Union of Geodesy and Geophysics, Vancouver, B.C., 1987b.

Mork, M., Experiments with theoretical models of the Norwegian Coastal Current, in *The Norwegian Coastal Current, II*, ed. by R. Saetre and M. Mork, 518-530, Univ. of Bergen, 1980.

Muench, R.D. and J.D. Schumacher, On the Bering Sea ice edge front, *J.*

Geophys. Res., *90*, 3185-3198, 1985.

Munk, W., Internal waves and small-scale processes, in *Evolution of Physical Oceanography*, ed. by Warren, B.A., and C. Wunsch, The MIT Press, Cambridge, Mass, 1981.

Murray, S.P., S.A. Hsu, H.H. Roberts, E.H. Owens, and R.L. Crout, Physical processes and sedimentation on a broad shallow bank, *Estuarine Coastal Shelf Sci*, *14*, 135-157, 1982.

Murray, S.P. and M. Young, The nearshore current along a high-rainfall, trade-wind coast - Nicaragua, *Estuarine Coastal Shelf Sci.*, *21*, 687-699, 1985.

Niebauer, H.J., J. Roberts, and T.C. Royer, Shelf break circulation in the northern Gulf of Alaska, *J. Geophys. Res.*, *86*, 4231-4242, 1981.

Neumann, G., *Ocean Currents*, 351 pp., Elsevier, Amsterdam, 1968.

Neumann, G., and W.J. Pierson, Jr., *Principles of Physical Oceanography*, Prentice-Hall, Englewood Cliffs, N.J., 1966.

Officer, C.B., *Physical Oceanography of Estuaries (and Associated Coastal Waters)*, 465 pp., John Wiley and Sons, New York, 1976.

Pettigrew, N.R., and S.P. Murray, The coastal boundary layer and inner shelf, in *Baroclinic Processes on Continental Shelves*, pp. 95-108, American Geophysical Union, Washington, D.C., 1986.

Ramming, H.-G., and Z. Kowalik, *Numerical Modelling of Marine Hydrodynamics*, 368 pp., Elsevier, New York, 1980.

Reed, R.K, J.D. Schumacher, and L.S. Incze, Water properties and circulation in Shelikov Strait, Alaska during 1985, NOAA Tech. Memo. ERL PMEL-68, 35 pp., 1986.

Royer, T.C., On the effect of precipitation and runoff on coastal circulation in the Gulf of Alaska, *J. Phys. Oceanog.*, 9, 555-563, 1979.

Royer, T.C., Baroclinic transport in the Gulf of Alaska, II, A fresh water driven coastal current, *J. Mar. Res.*, *39*, 251-266, 1981.

Royer, T.C., Coastal Fresh Water Discharge in the Northeast Pacific, *J. Geophys. Res.*, *87*, 2017-2021, 1982.

Royer, T.C., Observations of the Alaska Coastal Current, in *Coastal Oceanography*, ed. H. Gade, pp. 9-30, Plenum, New York, 1983.

Sarkisyan, A.S., The diagnostic calculations of a large-scale oceanic circulation, in *The Sea, vol. 6*, pp. 363-458, John Wiley and Sons, New York, 1977.

Schmidt, G.M., The exchange of water between Prince William Sound and the Gulf of Alaska, M.S. Thesis, 116 pp., Univ. of Alaska, Fairbanks, May, 1977.

Schumacher, J.D. and R. Reed, Coastal Flow in the northwest Gulf of Alaska: the Kenai Current, *J. Geophys. Res., 85*, 6680-6687, 1980.

Stommel, H., and A. Leetma, Circulation on the continental shelf, *Proc. Nat'l Acad. Sci., 69*, 3380-3384, 1972.

Thomson, R.E., A comparison between computed and measured oceanic winds near the British Columbia coast, *J. Geophys. Res.*, 88, 2675-2683, 1983.

Tomczak, M., Coordinate systems for zero and first derivative properties of seawater, *Ocean Modelling*, 72, 6-10, 1986.

Unesco, The Practical Salinity Scale 1978 and the International Equation of State of Seawater 1980, Tenth Report of the Joint Panel on Oceanographic Tables and Standards, 25 pp., *Unesco Tech. Pap. Mar. Sci., 36*, Unesco, Paris, 1981.

Wooster, W.S., An upwelling mythology, in *Coastal Upwelling*, pp. 1-3, Amer. Geophys. Union, Washington, D.C., 1981.